First Principles Study of Surface Stability and Interfacial Optical Response of InP(001) in Aqueous Environments

Dissertation

der Mathematisch-Naturwissenschaftlichen Fakultät

der Eberhard Karls Universität Tübingen

zur Erlangung des Grades eines

Doktors der Naturwissenschaften

(Dr. rer. nat.)

vorgelegt von

MSc. Vibhav Yadav
aus Delhi, India

Tübingen
2026

Gedruckt mit Genehmigung der Mathematisch-Naturwissenschaftlichen
Fakultät der Eberhard Karls Universität Tübingen.

Tag der mündlichen Qualifikation:	18.05.2026
Dekan:	Prof. Dr. Thilo Stehle
1. Berichterstatter:	Dr. Matthias May
2. Berichterstatter:	Prof. Dr. Reinhold Fink

Acknowledgments

I would like to express my gratitude from the bottom of my heart to Dr. Matthias May for providing me with the opportunity to work under his supervision within the Emmy Noether group *SPECSY*. It has been a great effort to explore the atomistic character of electrochemical interfaces of III-V semiconductors along the way of my PhD.

I would like to thank Prof. Dr. Reinhold Fink for being my second thesis supervisor. Special thanks to Prof. Dr. Udo Weimar and Prof. Dr. Monika Fleischer for being a part of the examination committee for my PhD defense.

For the begining of my PhD in Ulm I would like to thank Margot for her help in comprehending the experimental aspects of this research, and Jongmin Kim for his assistance in the theoretical aspects.

Working alongside Dr. Holger Euchner has been a privilege–I am hugely grateful for the stimulating debates and discussions that added to my experience of grappling with research issues collaboratively–it not only helped me gain a better understanding of the subject, but also forced me to challenge my way of thinking and experiment with new solutions.

I would further like to thank my colleagues for the lighthearted conversations.

Finally, I am highly indebted to my parents, Vandit, Subhadra, David, and most importantly, Charlotte, for being my guiding light and inspiration during difficult times. Without your unrelenting support, I would never have been able to pursue my research aspirations.

List of Publications

A. Research Papers

A1.

Yadav, V., Euchner, H., & May, M. M. (2025). The phase stability of InP(001) surfaces upon oxygen exposure from first principles. RSC Adv., 2025,15, 8464-8470

Scientific ideas: **VY (20%)**, HE & MM.

Data generation: **(VY 100%)**.

Analysis/Technical work: **VY (40%)**, HE & MM.

Paper writing: **(VY 33%)**, HE, & MM.

Supervision: HE & MM.

A2.

Yadav, V., Euchner, H., & May, M. M. (2025). Surface Dynamics of Clean and Oxygenated InP(001) Surfaces in Contact with Water – Insights from Computational Spectroscopy. ChemCatChem, 2026,18, e01347

Scientific ideas: **VY (20%)**, HE, and MM.

Data generation: **VY (100%)**.

Analysis/Technical work: **VY (50%)**, HE & MM.

Paper writing: **VY (33%)**, HE & MM.

Supervision: HE & MM.

A3.

Euchner, H., **Yadav, V.**, & May, M. M. (2025). The InP(100) Surface Phase diagram: from the gas phase to the electrochemical environment. ACS Appl. Mater. Interfaces 2025, 17, 5, 8601–8609

Scientific ideas: HE, **VY (10%)**, & MM.

Data generation: HE.

Analysis/Technical work: HE, **VY (5%)**, & MM.

Paper writing: HE, **VY (10%)**, & MM.

Supervision: MM.

Abstract

Shifting our reliance from activities related to greenhouse gas emissions is important to suppress global surface temperature rise. Renewable energy is key to decarbonising industrial sectors; specifically, photoelectrochemical water splitting using III-V tandem cells provides a viable route. However, atomistic-scale insight into interfacial changes–such as phase transitions and surface passivation–is rather limited under electrochemical conditions. Understanding the structural and temporal changes at the semiconductor–electrolyte interface is therefore important. III-V semiconductors, such as indium phosphide and its associated multinary alloys, show high performance in direct solar water splitting. In this work, we use first-principles calculations to investigate the thermodynamic stability of InP(001) surface reconstructions. We further analyse structural changes induced by oxygen exposure to mimic electrochemical conditions, providing a theoretical framework aligned with previous experimental results. Finally, for stable surface reconstructions, ab initio molecular dynamics and reflection anisotropy spectroscopy are used to analyse the evolution of optical anisotropy. These results could provide a correlation with real-time experimental observations at solid–vacuum and solid–liquid interfaces, where the latter is modelled as water in contact with the semiconductor surfaces. This study elucidates the thermodynamic landscape, demonstrating that P–dimer surfaces, specifically the $\beta 2(2\times4)$. P-rich (2×2) configurations, dominate upon oxygen exposure. Furthermore, our time-resolved optical anisotropy analysis reveals that the semiconductor–water interface induces significant temporal variations in optical signatures, driven by H_2O dissociation and subsequent ion migration. The computational insights gained from these InP(001) surfaces provide a foundational reference for investigating more complex III-V ternary alloys such as AlInP or GaInP. Future work could leverage computational hydrogen electrode model to analyse H/OH (co-)adsorption. Additionally transitioning from the IP-RPA toward GW or BSE methods will improve the accuracy of simulated time–resolved optical transitions, thereby capturing the higher-order electronic effects present.

Zusammenfassung

Die Verringerung unserer Abhängigkeit von Aktivitäten, die mit Treibhausgasemissionen verbunden sind, ist wichtig, um den globalen Anstieg der Oberflächentemperatur

zu unterdrücken. Erneuerbare Energien sind der Schlüssel zur Dekarbonisierung industrieller Sektoren; insbesondere die photoelektrochemische Wasserspaltung mittels III-V-Tandemzellen bietet einen gangbaren Weg. Jedoch ist der Einblick auf atomistischer Skala in Grenzflächenveränderungen – wie Phasenübergänge und Oberflächenpassivierung – unter elektrochemischen Bedingungen eher begrenzt. Das Verständnis der strukturellen und zeitlichen Veränderungen an der Halbleiter-Elektrolyt-Grenzfläche ist daher wichtig. III-V-Halbleiter wie Indiumphosphid und ihre zugehörigen multinären Legierungen zeigen eine hohe Leistung bei der direkten solaren Wasserspaltung. In dieser Arbeit nutzen wir First-Principles-Berechnungen, um die thermodynamische Stabilität von InP(001)-Oberflächenrekonstruktionen zu untersuchen. Wir analysieren ferner strukturelle Veränderungen, die durch Sauerstoffexposition induziert werden, um elektrochemische Bedingungen nachzuahmen, und liefern damit einen theoretischen Rahmen, der mit früheren experimentellen Ergebnissen übereinstimmt. Schließlich werden für stabile Oberflächenrekonstruktionen Ab-initio-Molekulardynamik und Reflexionsanisotropiespektroskopie eingesetzt, um die Entwicklung der optischen Anisotropie zu analysieren. Diese Ergebnisse könnten eine Korrelation mit Echtzeit-Experimenten an Festkörper-Vakuum- und Festkörper-Flüssigkeit-Grenzflächen liefern, wobei letztere als Wasser in Kontakt mit den Halbleiteroberflächen modelliert wird. Diese Studie verdeutlicht die thermodynamische Landschaft und zeigt, dass P-Dimer-Oberflächen, insbesondere die $\beta 2(2\times 4)$- und die P-reichen (2×2)-Konfigurationen, bei Sauerstoffexposition dominieren. Darüber hinaus zeigt unsere zeitaufgelöste optische Anisotropieanalyse, dass die Halbleiter-Wasser-Grenzfläche signifikante zeitliche Variationen in den optischen Signaturen induziert, angetrieben durch die Dissoziation von H_2O und die anschließende Ionenmigration. Die aus diesen InP(001)-Oberflächen gewonnenen rechnerischen Erkenntnisse bieten eine grundlegende Referenz für die Untersuchung komplexerer ternärer III-V-Legierungen wie AlInP oder GaInP. Zukünftige Arbeiten könnten das Modell der computergestützten Wasserstoffelektrode nutzen, um die (Co-)Adsorption von H/OH zu analysieren. Zusätzlich wird der Übergang vom IP-RPA hin zu GW- oder BSE-Methoden die Genauigkeit simulierter zeitaufgelöster optischer Übergänge verbessern und dadurch die vorhandenen elektronischen Effekte höherer Ordnung erfassen.

Contents

1 Motivation

Life on Earth is now confronting an escalating climate emergency because of greenhouse gas (GHG) emissions from fossil-fuel use, industrial activities, and land-use. These activities lead to a considerable increase in the concentrations of CO_2, CH_4, and N_2O in the troposphere. Consequently, global mean surface temperature rise of approximately 1.1° C relative to 1850–1900 baseline can be attributed to the strengthening of radiative forcing [1]. Since the mid-20^{th} century, observed changes in global warming are unparalleled over centuries, reflecting the combined, lasting effect of human-induced climate drivers.

The consequences of this warming are already visible across both natural and human systems. Physical manifestations include more intense and frequent heat extremes, altered precipitation patterns, and a widespread decline of the cryosphere (e.g. sea-ice, glaciers etc.). These changes are accompanied by accelerating sea–level rise, along-with warming and acidification of the ocean [2].

Presently, international mitigation and adaptation policies are lagging severely behind the stringent requirements necessary to reach the globally agreed climate target, underscoring a critical **"implementation gap"** where some political promises do not turn into effective action on the ground. (Fig. 1). Existing policies, are considered rather unlikely to limit the warming to 1.5° C and also adds a hurdle to the goal of remaining below 2° C. Therefore, systematic transitions across energy systems, industry, land management, and consumption patterns are necessary to achieve low emission pathways [1]. In this context, systematic understanding of climate change and the improvement of mitigation techniques are crucial. Current renewable sources–including solar, wind, bioenergy, geothermal, hydro-power, and ocean energy– are key to this transition. Although these sources are expected to dominate the future energy sector, alternative solutions are still required due to current limitations, such as intermittency, land-use conflicts, geographical dependence, and high early-stage technology costs [3]. Enabling large-scale renewable deployment requires energy storage and conversion technologies. To shift focus away from fossil fuels and toward sustainable alternatives, the use of lithium-ion batteries has become well established, particularly in the automotive industry [4]. However, the battery industry currently faces significant concerns regarding resource scarcity, safety, and long-term sustainability [5, 6, 7, 8].

Hydrogen is a versatile alternative: it is carbon-free at the point of use, has high

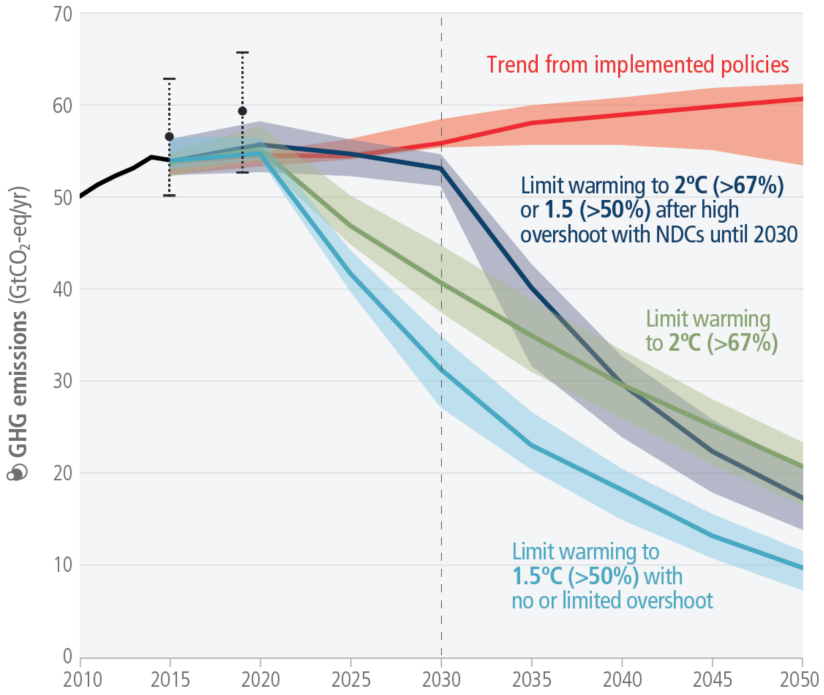

Figure 1: IPCC AR6 SYR figure2.5,showcasing that the policies implemented will result in higher GHG emissions by 2030 in comparison to those implied by nationally determined conributions (NDCs), taken from ref. [1].

gravimetric energy density, and can be produced through direct solar-water-splitting via photoelectrochemical (PEC) processes [9, 10]. The urgent need for these technologies stems from the requirement for *renewable fuels of non-biological origins*. These fuels are essential for decarbonising hard-to-abate sectors such as heavy industry, aviation, and shipping. Currently, several common routes for hydrogen production offer distinct trade-offs:

1. Steam Methane Reforming (SMR) remains the lowest cost option, assessed at $\sim$ 1.39\$ per kg H_2 in a 2016 analysis [11]; however, its heavy carbon footprint must be offset by costly carbon capture [12].

2. Photovoltaic-Electrolysis (PV-E) represents a technologically advanced route; however, hydrogen from PV-E remains expensive due to the high cost of electrolysers and Balance-of-System (BoS) components [13]. A 2020 techno-economic analysis suggested that due to falling PV panel prices, the Levelised Cost of Hydrogen (LCOH) for an off-grid PV-E is \$6.22 $kg_{H_2}^{-1}$ at 10.9% efficiency [14].

3. Photoelectrochemical (PEC) offers a simpler approach by integrating light absorption, charge separation, and catalysis into a single monolithic unit. Initially a lower LCOH value was reported for a base-case PEC ($\sim$\$11.4 $kg_{H_2}^{-1}$) compared to an off-grid PV-E ($\sim$\$12.1 $kg_{H_2}^{-1}$) [11]. Recent reports factoring in updated PV prices estimate the PEC LCOH at \$8.43 $kg_{H_2}^{-1}$ at 10% efficiency [14].

Thus, while PV-E leads in maturity and SMR in cost, the techno-economic benefits of PEC systems remain uncertain and limited [14]. Hence, for long-term sustainability and cost-effective decarbonisation, significant advances are required for PEC devices to compete with already existing energy sources. A primary hurdle for renewable energy is converting variable solar power into storable chemical fuel. A tandem PEC cell addresses this by combining light harvesting and water splitting into one unit, potentially reducing BoS costs by eliminating separate PV-arrays and an external electrolyser. However, PEC systems currently face a higher LCOH value than PV-E due to contingency costs and technical uncertainties [14]. These economic challenges originate from material science limitations: specifically, poor operational lifetimes and low efficiencies caused by corrosion and defect-mediated recombination at the semiconductor–electrolyte interface [15, 16]. Overcoming these limitations is essential towards achieving high efficiency (photo-)electrodes necessary for commercialisation.

2 Introduction

A primary objective in photoelectrochemical energy conversion is achieving sustainable performance; however, a critical limiting factor remains the poor stability of high-performance semiconductor (photo-)electrodes in aqueous electrolytes. Materials such as indium phoshpide and its ternary alloys demonstrate excellent light absorption characteristics for solar water splitting [17, 18], yet their surfaces are highly susceptible to degradation [16]. The electrochemical environment induces alterations in surface structure and stoichiometry, which subsequently modify the electronic structure, resulting in the formation of charge-carrier recombination centers and acting as points for material dissolution [19]. Consequently, a comprehensive understanding of these interfacial phenomena at the atomistic and electronic scales is essential to mitigate these corrosive pathways that otherwise degrade device performance [20, 21].

Correlating experimental and theoretical data at electrochemical interfaces presents significant challenges. To bridge this gap and reconcile discrepancies between models and observations, inherent system limitations must be explicitly accounted for. Investigating finite-temperature surface dynamics at the semiconductor–water interface via ab initio molecular dynamics (AIMD) simulations on a picosecond timescale yields crucial atomistic insights (Sec. 9.1). Specifically, these simulations facilitate a direct comparison between the semiconductor in contact with H_2O and solid–vacuum interface. While the vacuum interface establishes a baseline, the dynamic interactions with the aqueous environment introduce effects that can profoundly alter the surface electronic structure. Furthermore, these models track the temporal evolution of optical anisotropy for each respective interface [22].

The remainder of this work is structured as follows: Sec. 2.1.1 outlines the fundamental principles governing PEC water splitting; Sec 2.1.2 introduces key concepts and challenges associated with electrochemical interfaces; and Sec. 2.1.3 provides a brief overview of reflection anisotropy spectroscopy (RAS). Following these introductory subsections, the theoretical framework based on density functional theory (DFT) is detailed in Sec. 4. Subsequently, our findings are presented and discussed: Sec. 5.1 evaluates the thermodynamic phase stability of the InP(001) in vacuum and post oxygen exposure, while Sec. 5.2 showcases the surface dynamics of these stable phases as resolved via RAS.

2.1 Photoelectrochemical Water Splitting

PEC water splitting can be conceptualised as a process utilising a semiconducting (photo-)electrode that directly converts solar energy into a (photo-)voltage and the resulting (photo-)current, which is essential to drive the water splitting reaction, resulting in H_2 & O_2 evolution. The overall reaction is expressed as:

$$2H_2O(l) \rightarrow 2H_2(g) + O_2(g) \tag{2.1}$$

The standard Nernst potential required for the reaction is 1.23 V. In practice, the operating (photo-)voltage must be higher than this theoretical threshold due to energy losses, such as the overpotential required to overcome kinetic barriers and ohmic losses in the setup. While 1.23 eV sets the thermodynamic limit under standard conditions, additional kinetic barriers introduce an overpotential of $\sim$ 0.4–0.6 V, meaning (photo-)voltages of $\sim$ 1.6–1.8 V are typically required for the device operation [23]. III-V tandem (photo-)absorbers, particularly combinations such as GaInP/GaAs, are attractive for PEC devices [18]. Their tunable bandgaps allow optimised absorption of solar spectrum.

2.1.1 Working Principles

Under operating conditions, for PEC device, charge-carrier generation and migration can be regarded as a process that is driven by the gradient of the electrochemical potential (Fermi level), rather than by the built-in electric field [24, 25]. Consequently, surface reactions are controlled by the quasi-fermi level splitting at the interface, so sufficient carrier accumulation or inversion can enable hydrogen evolution even when the redox potential lies outside the band gap under flat–band conditions [26]. Upon contact between the semiconductor and the electrolyte, equilibration of the fermi level (E_F) and the electrolyte redox level ($E_{R,O}$) leads to an interfacial potential difference ($e\Delta\Phi$). In the absence of surface states (Fig. 2a), this potential drop occurs entirely within the semiconductor and results in band bending (V_{bb1}), such that $e\Delta\Phi=V_{bb1}$. The associated electric field extends over the space-charge region of width d_{SC}. In contrast when a high density of surface states is present (Fig. 2b), fermi-level pinning occurs and the band bending is fixed at V_{bb2}. The total interfacial potential difference is then partitioned between the semiconductor and the electrolyte as; $e\Delta\Phi=eV_{bb2}+e\Delta\Psi_H$, where $\Delta\Psi_H$ corresponds to potential drop in the Helmholtz region with the width d_H, effectively shifting the electric

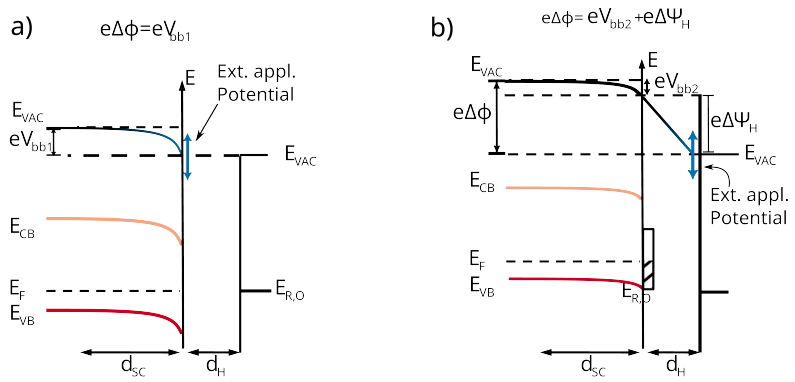

Figure 2: Band diagram of a p-type semiconductor in contact with an electrolyte. (a) showcases the semiconductor–electrolyte surface without surface states, (b) is the same situation as (a) but with high density of electronic states (vertical box, striped for occupied). The energy levels depicted are for the vacuum level E_{VAC}, the conduction and valence band edges as E_{CB} and E_{VB} resp., the semiconductor fermi level E_F, and the redox level of the electrolyte as $E_{R,O}$. This figure is taken from ref. [27].

field from the semiconductor space-charge region to the Helmholtz layer.

2.1.2 Electrochemical Interface

The main issue that hinders the increase of technological readiness level (TRL) is the lack of a fundamental understanding of the complexities governing the semiconductor–electrolyte interface. Here, the applied potential and the chemical environment often induce structural changes such as (phase transitions, corrosion, and degradation) of the (photo-)absorber. These modifications, in turn, alter the electronic structure by incorporating inhomogenieties in the surface electron density, which facilitates the formation of charge-carrier recombination centres or leads to material dissolution [28, 29]. Hence, it is important to analyse the structure, stability, and reactivity of the interface for improving the sustenance of the PEC water splitting device [30].

InP, a binary semiconductor, is a good model system for photoelectrochemical processes due to its direct 1.34 eV bandgap and high electron mobility. Its multinary alloys, such as $GaInP_2$ absorbers or AlInP window layers, are critical for high efficiency photovoltaic or photoelectrochemical solar cells [17, 31, 18].

The microscopic structure of the surface reconstructions has been explored for the InP(001) surfaces along In- and P-rich regions [32, 33]. Most computational studies of InP(001) focus on the (2×4) mixed-dimer reconstruction, which is synthesised through

epitaxial growth or ion bombardment and annealing [34]. The interfacial characteristics are as follows:

1. Surface Passivation: Prior studies related to oxygen/hydroxyl adsorption on In-rich surface reconstructions, reported the formation of surface limited M-O-M and M-O-P bridges, where M-O-M bridge acts as a hole trap that facilitates charge-carrier recombination and subsequent corrosion [35]. These distinct bonding motifs are found to form preferentially under oxygen exposure, and to a lesser extent under water exposure [19], where the surface instead tends to form P_xO_y polyphosphate motifs that can passivate and stabilise under operating conditions [36].

2. Interfacial dynamics: Reactivity towards the electrolyte is highly sensitive to the surface structure. While a pristine surface exhibits a high energy H_2O dissociation barrier, the presence of a thin native oxide layer renders H_2O adsorption and dissociation exothermic and barrier-less [37]. AIMD simulations reveal that the strong H-bond network at this hydroxylated interface aids in proton hopping via the Grotthus mechanism [38], directly linking the interplay of the surface–water dynamics to the overall kinetics of the hydrogen evolution reaction.

While these studies established an initial understanding of the electrochemical interface, the broader problem remains divided into two aspects: first, determining the thermodynamically stable phases under operating conditions; and second, correlating interfacial dynamics through measurement. Using a model system allows for a deeper understanding of how surface chemistry evolves under these conditions. RAS can be helpful as it can provide insight into structural changes in real-time, but it has some problems, such as correlating the optical response to a definitive surface structure without the use of computational models. Quite recent work showed that highly ordered InP(001) surfaces can be stabilised directly in aqueous electrolytes under a suitable potential [39], and the study also showcases the possibility of correlating results obtained from experiments and DFT models.

Missing links from theoretical insights are what this work is trying to provide by assessing the **thermodynamic stability** and then developing an understanding of the **time-resolved optical response** of the stable structures in contact with H_2O.

2.1.3 Optical Probing of Surfaces & Interfaces

There is a broad class of surface–probing optical methods, collectively known as **epioptics** (from Greek *epi* meaning "upon" the surface). For example, experiments which measures the change in absolute reflectivity (ΔR) are referred to as Differential-Reflectance Spectroscopy (DRS) or Surface Differential reflectivity (SDR), but they suffers from the drawback that they require two different measurements i.e. an additional externally-defined reference state (e.g., a known clean surface or a separate reference sample) to normalise the signal ($\frac{\Delta R}{R} = \frac{R_{clean} - R_{ref}}{R_{ref}}$) [40, 41]. In contrast RAS measures the present optical anisotropy by comparing the reflectivity between two perpendicular principal axes. RAS, a highly surface sensitive optical-probe, can operate in a wide range of environments [42], from ultra-high vacuum to liquid electrolytes [43]. It can be regarded to some extent as a further development of spectroscopic ellipsometry (SE) [44]. This technique is particularly valuable for its ability to perform *in-situ* studies, allowing for a real-time investigation of dynamic interfacial changes as they occur [19] due to the break in symmetry from bulk towards the surface. Recent studies related to the monitoring of surface morphology and reconstruction changes, with oscillations in the RAS signal during epitaxial growth linked to the periodic modulation of surface strain, are also reported [45]. RAS measures the difference in optical reflectivity between two principal axes of a crystal surface, i.e. RAS:=$\frac{\Delta r}{r} = 2\frac{r_{[\bar{1}10]} - r_{[110]}}{r_{[\bar{1}10]} + r_{[110]}}$. It was usually thought that the bulk signal is suppressed due to the absence of anisotropy, a recent study suggests that many "*bulk-related*" features are *bulk-enhanced surface anisotropies*. This is due to the localisation of states at the surface that are strongly modulated by the bulk dielectric function [46]. For a long time, the full exploitation of experimental RAS was limited because it being an "*inverse problem*": it doesn't directly provide information regarding the cause of the effect (optical response). One can experimentally link RAS to a specific atomic arrangement, resulting in the use of high-resolution techniques like STM, SEM, or LEED [48, 49, 50].

This gap is addressed by computational methods such as RPA (see Sec. 4.1.9) and GW (full RPA), approaching the accuracy required for the predictive modelling of surface optical responses [51]. There has been a transition from identifying structural fingerprints towards many-body electronic effects and the analysis of changes under dynamic environments. RAS calculations are performed on top of a ground state calculation of the electronic structure. Initial studies comparing results obtained from the DFT-LDA and

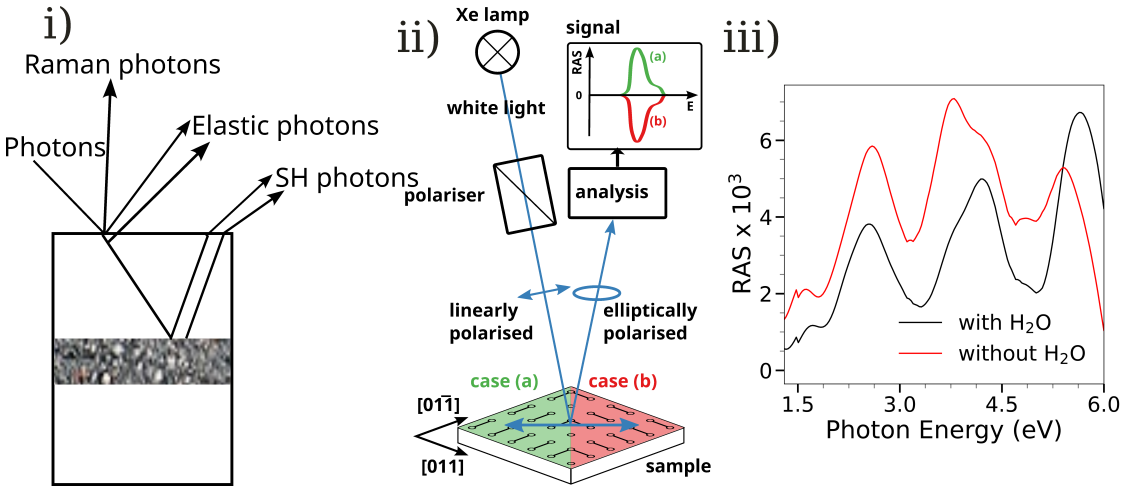

Figure 3: Overview of Epioptics, (i) principle showing the interaction of incident polarised light, and reflected light (including elastic, Raman, or second-harmonic photons), adapted from ref. [47], demonstrating the ability to probe buried interface due to the penetration depth of optical radiation (ii) RAS principles: White, polarised light reflects off the sample, and if optical anisotropy exists, the reflected light becomes elliptically polarised, with its behaviour analysed as a function of energy. Case (a) shows a dimerised surface with dimers oriented along the [0$\bar{1}$1] direction (green). Case (b) shows the same surface with dimers oriented along the [011] direction (red), resulting in a reversed RAS signal, (iii) theoretical RAS of $\beta 2(2\times4)$ InP(001) with and without H_2O. Sub-figure (ii) is taken from ref. [19].

GW framework, on GaP(001) surfaces were able to link the spectral features related to transitions between Ga-Ga bonding states and empty Ga bonds [32]. The accuracy can be further refined by including many-body corrections that account for excitonic effects by using GW and Bethe-Salpeter equations (BSE) [52]. Currently, it is possible to identify the structural fingerprints of AlInP(001), a ternary semiconductor [53]. Recently, time-dependent fluctuations in the optical anisotropy of metallic systems observed during AIMD simulations have also been reported [54], highlighting that thermal fluctuations and surface reordering–especially in liquid environments–are crucial for a realistic theoretical analysis.

3 Objectives

The focus of this study is to provide an atomistic-scale understanding of the InP(001) surface chemistry via density functional theory. The specifics of the study are as follows:

1. Phase stability analysis: To establish the thermodynamic stability of clean InP(001) reconstructions and evaluate the impact of oxygen adsorption on In- and P-rich stable surfaces. This involves characterising the formation of experimentally reported P_xO_y motifs that alter the surface energy relative to the degree of passivation, ultimately enabling the determination of stability from the overall phase diagram, as illustrated in publication *A1*.

2. Semiconductor–water interface: To analyse the structural dynamics of solid–vacuum and solid–liquid interfaces by introducing H_2O layers onto the respective stable surfaces. Herein, we aim to analyse how structural changes during AIMD simulations influence the resulting RA-spectrum, illustrated in publication *A2*.

3. Dynamic response: To compute the time-resolved optical response of stable interfaces. RA-spectra of snapshots from equilibrated AIMD trajectories aim to correlate structural changes with the optical signals, as illustrated in publication *A2*.

4. Potential dependent phase transformations: To investigate the impact of the applied electrochemical potential on surfaces. Using the computational hydrogen electrode model, the study aims to characterise the transitions between In-rich and Cl-rich reconstructions under H/Cl (co-)adsorption, highlighted in publication *A3*.

4 Methods

DFT provides a practical and powerful framework for electronic structure calculations. Its success lies in reformulating the many-body Schrödinger equation into a problem which is expressed in terms of the electron density $\rho(\mathbf{r})$, a function of three spatial coordinates, rather than the $3N$-dimensional many-electron wave-function $\Psi(\mathbf{r}_1, \ldots, \mathbf{r}_N)$. This simplification makes DFT computationally feasible for realistic materials and molecules, while still capturing essential quantum-mechanical effects.

4.1 Density Functional Theory

Within the Born-Oppenheimer approximation, the non-relativistic electronic Hamiltonian operator (H_{elec}) of a system containing N_{e} electrons and N_{nuc} nuclei can be expressed as a sum of specific energy operators:

$$H_{\text{elec}} = T_{\text{e}} + V_{\text{e-nuc}} + V_{\text{e-e}} = -\frac{1}{2}\sum_{i=1}^{N_{\text{e}}} \nabla_i^2 - \sum_{i=1}^{N_{\text{e}}}\sum_{\alpha=1}^{N_{\text{nuc}}} \frac{Z_\alpha}{|\mathbf{r}_i - \mathbf{R}_\alpha|} + \frac{1}{2}\sum_{i\neq j}^{N_{\text{e}}} \frac{1}{|\mathbf{r}_i - \mathbf{r}_j|}\,. \tag{4.1}$$

Here, the first term represents the electronic kinetic energy operator (T_{e}), describing the motion of the electrons. The second term is the electron–nucleus attractive potential energy operator ($V_{\text{e-nuc}}$), representing the electrostatic Coulomb attraction between the negatively charged electrons at positions $\mathbf{r}_i$ and the positively charged nuclei with atomic numbers Z_α fixed at positions $\mathbf{R}_\alpha$. The third term is the electron–electron repulsive potential energy operator ($V_{\text{e-e}}$), accounting for the mutual Coulomb repulsion between all pairs of interacting electrons.

The central quantity in DFT is the ground-state electron density, defined from the many-electron wavefunction Ψ as:

$$\rho(\mathbf{r}) = N_{\text{e}} \int |\Psi(\mathbf{r}, \mathbf{r}_2, \ldots, \mathbf{r}_{N_{\text{e}}})|^2 \, d\mathbf{r}_2 \ldots d\mathbf{r}_{N_{\text{e}}}\,. \tag{4.2}$$

This formulation represents the probability of finding any of the N_{e} electrons within a specific volume around the spatial coordinate $\mathbf{r}$, which properly integrates to the total number of electrons in the system:

$$\int \rho(\mathbf{r})\, d\mathbf{r} = N_{\text{e}}\,. \tag{4.3}$$

4.1.1 Hohenberg–Kohn Theorems

Hohenberg and Kohn (1964) established two fundamental theorems that lay the groundwork for DFT [55]:

1. The ground-state density $\rho(\mathbf{r})$ uniquely determines the external potential $v_{\text{ext}}(\mathbf{r})$ (up to an additive constant), and thus the full Hamiltonian and all ground-state observables.

2. A variational principle exists: for any trial electron density $\tilde{\rho}(\mathbf{r})$ consistent with the total number of electrons N, the total energy satisfies:

$$E[\tilde{\rho}] \geq E[\rho_0], \tag{4.4}$$

   where ρ_0 is the exact ground-state density, obtained by minimising the energy functional $E[\rho]$ with respect to $\rho(\mathbf{r})$.

4.1.2 Kohn–Sham Equations

Kohn and Sham (1965) introduced the idea of an auxiliary system of non-interacting electrons that reproduces the exact ground-state density [56]. The total energy functional can then be partitioned as:

$$E[\rho] = T_{\text{s}}[\rho] + \int v_{\text{ext}}(\mathbf{r})\rho(\mathbf{r})\, d\mathbf{r} + \frac{1}{2}\int \frac{\rho(\mathbf{r})\rho(\mathbf{r}')}{|\mathbf{r}-\mathbf{r}'|}\, d\mathbf{r}d\mathbf{r}' + E_{\text{xc}}[\rho]\,. \tag{4.5}$$

Variation of this functional with respect to $\rho(\mathbf{r})$ yields the Kohn-Sham (KS) equations:

$$\left[-\frac{1}{2}\nabla^2 + v_{\text{ext}}(\mathbf{r}) + v_{\text{H}}(\mathbf{r}) + v_{\text{xc}}(\mathbf{r})\right]\psi_i(\mathbf{r}) = \varepsilon_i\psi_i(\mathbf{r})\,, \tag{4.6}$$

where $v_{\text{ext}}(\mathbf{r})$ is the external potential representing the electrostatic interaction between the electrons and the nuclei, $v_{\text{H}}(\mathbf{r})$ is the Hartree potential defined as the classical, aforementioned electron-electron repulsive potential:

$$v_{\text{H}}(\mathbf{r}) = \int \frac{\rho(\mathbf{r}')}{|\mathbf{r}-\mathbf{r}'|}\, d\mathbf{r}'\,, \tag{4.7}$$

and the exchange-correlation potential $v_{\text{xc}}(\mathbf{r})$ accounts for all remaining many-body

quantum effects, represented as the functional derivative of the exchange-correlation energy that maps quantum exchange, electron correlation, and self-interaction corrections into a local potential:

$$v_{\mathrm{xc}}(\mathbf{r}) = \frac{\delta E_{\mathrm{xc}}[\rho]}{\delta \rho(\mathbf{r})}\,. \tag{4.8}$$

Herein, the electron density is constructed from the occupied KS orbitals, and can be expressed as:

$$\rho(\mathbf{r}) = \sum_{i}^{\mathrm{occ}} |\psi_i(\mathbf{r})|^2\,. \tag{4.9}$$

4.1.3 Self Consistent Field Method

The Self-Consistent Field (SCF) method is an iterative approach used to obtain a stable electronic charge density that satisfies the KS equations in DFT. The method involves repeatedly updating the electron density until self-consistency between the input and output densities is achieved, which illustrates the schematic workflow of the SCF procedure (Fig. 4).

The process begins with an initial guess for the electron density, $\rho(\mathbf{r})$, which can be generated from atomic superpositions or a previous calculation. Based on this density, the effective KS potential is calculated as:

$$v_{\mathrm{KS}}[\rho(\mathbf{r})] = v_{\mathrm{ext}}(\mathbf{r}) + v_{\mathrm{H}}[\rho(\mathbf{r})] + v_{\mathrm{xc}}[\rho(\mathbf{r})]\,. \tag{4.10}$$

Using this potential, the KS equations are solved:

$$\left[-\frac{1}{2}\nabla^2 + v_{\mathrm{KS}}[\rho(\mathbf{r})]\right]\psi_i(\mathbf{r}) = \varepsilon_i \psi_i(\mathbf{r})\,, \tag{4.11}$$

yielding a new set of KS orbitals $\psi_i(\mathbf{r})$ and corresponding eigenvalues ε_i. From these orbitals, an updated electron density is constructed as:

$$\rho_{\mathrm{out}}(\mathbf{r}) = \sum_{i}^{\mathrm{occ}} |\psi_i(\mathbf{r})|^2\,. \tag{4.12}$$

The newly obtained density is compared to the previous iteration's density. If the difference is within a predefined convergence threshold, the calculation is considered self-consistent, and relevant quantities such as the total energy, charge density, and band

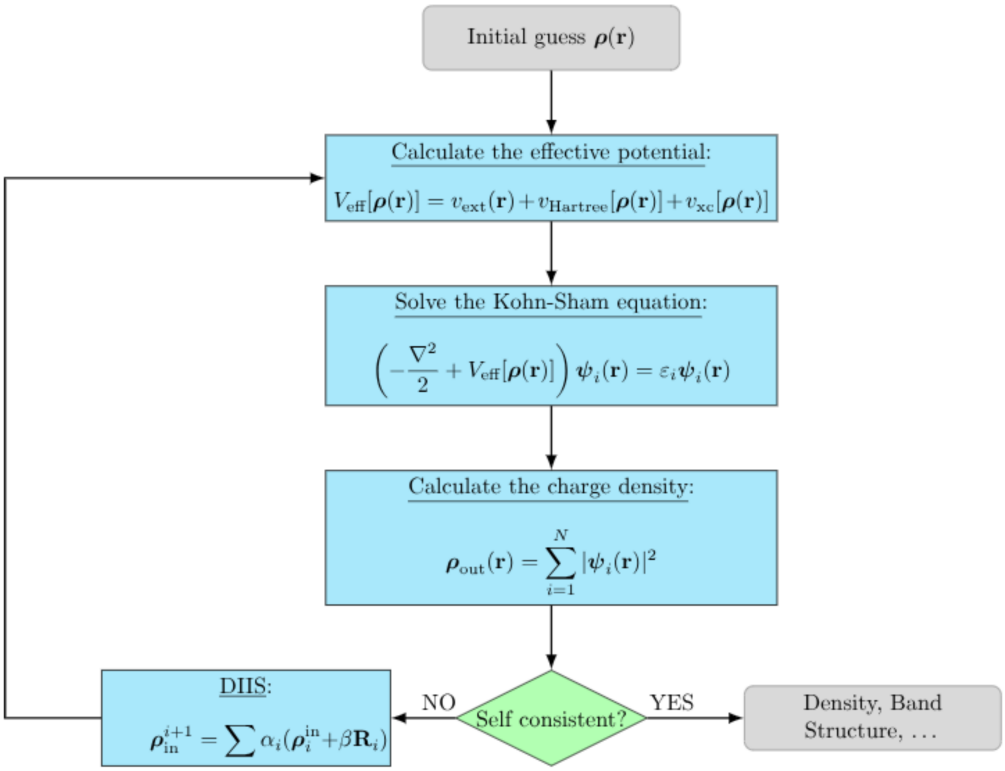

Figure 4: The Self-Consistent Field (SCF) method with density mixing. This figure is adapted from ref. [57].

structure are extracted. If self-consistency has not yet been achieved, the densities are mixed to generate a new input density for the next iteration. Various mixing schemes are employed to accelerate convergence, one common approach being the Direct Inversion in the Iterative Subspace (DIIS) method, expressed as:

$$\rho_{\text{in}}^{n+1} = \sum_j \alpha_j(\rho_{\text{in}}^j + \beta R_j)\,, \tag{4.13}$$

where R_j denotes the residual error vector between the input and output densities, and α_j, β are mixing parameters.

This iterative loop continues until the input and output densities become indistinguishable within the desired tolerance, marking the system as self-consistent.

4.1.4 Pseudopotentials

The explicit treatment of all electrons in a system is computationally inefficient due to core states being tightly bound and oscillatory near the nucleus. In practice, most chemical and structural properties related to interfacial phenomena are determined by the valence electrons, while the core remains chemically inert. Hence, via pseudopotentials, the strong nuclear potential is replaced by a smoother effective potential that acts only on the valence electrons [58].

In the KS framework with pseudopotentials, the effective H for the valence electrons can be expressed as:

$$H_{\mathrm{KS}}^{\mathrm{PP}} = T_{\mathrm{s}} + v_{\mathrm{loc}}^{\mathrm{PP}}(\mathbf{r}) + v_{\mathrm{nl}}^{\mathrm{PP}} + v_{\mathrm{H}}[\rho] + v_{\mathrm{xc}}[\rho]\,, \tag{4.14}$$

where $v_{\mathrm{loc}}^{\mathrm{PP}}$ is a smooth local potential that models the long-range electrostatic interaction outside a chosen core radius, $v_{\mathrm{nl}}^{\mathrm{PP}}$ introduces angular momentum dependence through non-local projectors to capture the short-range scattering effects of different core shells, and v_{H}, v_{xc} are the Hartree and exchange–correlation contributions [59].

There are several widely used pseudopotentials:

1. **Norm-conserving pseudopotentials**, which preserve the norm of the valence wavefunctions inside a chosen core radius [60].

2. **Ultrasoft pseudopotentials**, which relax the norm-conservation condition to allow smoother pseudo-wavefunctions and smaller basis sets [61].

3. **Projector augmented-wave (PAW) method**, which reconstructs all-electron wavefunctions from smooth auxiliary orbitals via linear transformations [62].

The choice of the pseudopotential depends on the basis set and the code. For example, the Gaussian and plane-wave (GPW) approach often employs Goedecker-Teter-Hutter (GTH) pseudopotentials, while plane-wave codes commonly support norm-conserving, ultrasoft, and PAW formulations of the pseudopotentials.

4.1.5 Basis Sets

In KS DFT, the single-particle orbitals, $\psi_i(\mathbf{r})$, are structured as a linear combination of basis functions $\{\chi_\mu(\mathbf{r})\}$:

$$\psi_i(\mathbf{r}) = \sum_\mu C_{\mu i}\, \chi_\mu(\mathbf{r}), \tag{4.15}$$

where $C_{\mu i}$ are the expansion coefficients determined from the self-consistent field method, forming the density matrix that maps the continuous electronic problem onto a discrete matrix eigenvalue problem.

Two main types of basis sets are commonly used. In periodic systems, plane waves provide a natural and unbiased basis, where each orbital is expanded:

$$\psi_i(\mathbf{r}) = \sum_{|\mathbf{G}|^2/2 \leq E_{\text{cut}}} c_i(\mathbf{G})\, e^{i\mathbf{G}\cdot\mathbf{r}}, \tag{4.16}$$

where $\mathbf{G}$ are the reciprocal lattice vectors that span the Fourier space of the periodic cell, and E_{cut} is the kinetic energy cutoff, a critical convergence parameter that truncates the infinite Fourier series to a finite, computationally manageable set. Due to plane waves being delocalised, they are known to efficiently represent smoothed-out valence wavefunctions, although requiring pseudopotentials to eliminate the need to describe the oscillatory core states.

The orbital representation can also be presented if one uses the localised basis functions centred at atomic sites, such as Gaussian-type orbitals (GTOs):

$$\chi_\mu(\mathbf{r}) = \sum_p d_{\mu p}\, e^{-\alpha_p |\mathbf{r}-\mathbf{R}_A|^2}, \tag{4.17}$$

where α_p is the Gaussian exponent exponent governing the radial decay and spatial width of the orbital shell, $d_{\mu p}$ is the contraction coefficient used to combine primitive Gaussians into fixed atomic-like functions, and $\mathbf{R}_A$ denotes the position of nucleus A. These basis sets are compact and efficient for describing molecular environments and localised states.

Also, on the other hand, a few electronic structure methods combine the advantages of both approaches. For instance, the Gaussian and Plane Wave (GPW) scheme uses atom-centred Gaussian orbitals for the Kohn-Sham states, while the electron density is

represented in an auxiliary plane-wave basis:

$$\rho(\mathbf{r}) = \sum_{i}^{\text{occ}} |\psi_i(\mathbf{r})|^2 \quad \Rightarrow \quad \rho(\mathbf{r}) = \sum_{|\mathbf{G}| \leq G_{\max}} \tilde{\rho}(\mathbf{G})\, e^{i\mathbf{G}\cdot\mathbf{r}}, \tag{4.18}$$

where $\tilde{\rho}(\mathbf{G})$ represents the complex Fourier coefficients of the electron density, and $G_{\max}$ is the density cutoff in reciprocal space. This allows efficient computation of the Hartree potential in reciprocal space via the fast Fourier transform (FFT) while retaining the locality and efficiency of Gaussian orbitals [63].

The choice of basis depends on the system and computational code: plane-wave approaches (e.g., QUANTUM ESPRESSO) emphasise systematic convergence [64], whereas localised or mixed schemes (e.g., GPW methods in CP2K) provide efficiency for large heterogeneous systems [65]. In all cases, the basis set defines the balance between computational cost and accuracy.

4.1.6 Exchange-Correlation Approximations

The challenge of DFT is the construction of accurate approximations to $E_{\text{xc}}[\rho]$. Perdew famously described these as rungs on a "Jacob's ladder" of density functional approximations, climbing from the simplest local forms toward the "heaven" of chemical accuracy. The explicit sum of the exchange–correlation functional can be expressed as the exchange and correlation terms:

$$E_{\text{xc}}[\rho] = E_{\text{x}}[\rho] + E_{\text{c}}[\rho]\,. \tag{4.19}$$

Local Density Approximation (LDA) has been one of the earliest formulations of the exchange–correlation functional in the framework of DFT. Herein, the assumption made for calculating the exchange-correlation energy is that $E_{\text{xc}}^{\text{LDA}}[\rho]$ at each point in space depends solely on the local electron density, as if each infinitesimal region of the system were part of a homogeneous electron gas (HEG) with the same density. Accordingly, the E_{xc} functional can be expressed as:

$$E_{\text{xc}}^{\text{LDA}}[\rho] = \int \rho(\mathbf{r})\, \varepsilon_{\text{xc}}^{\text{HEG}}(\rho(\mathbf{r}))\, d\mathbf{r}, \tag{4.20}$$

where $\varepsilon_{\mathrm{xc}}^{\mathrm{HEG}}(\rho)$ denotes the exchange–correlation energy per particle of a uniform electron gas with density ρ. The exchange component, derived from the HEG model, can be expressed as:

$$\varepsilon_{\mathrm{x}}^{\mathrm{LDA}}(\rho) = -\frac{3}{4}\left(\frac{3}{\pi}\right)^{1/3}\rho^{1/3}. \tag{4.21}$$

On the other hand, correlation effects cannot be solved analytically and are dealt with using Quantum Monte Carlo (QMC) data for the homogeneous electron gas [66]. An analytic expression for ε_{c} of the HEG is available in the high-density limit [67], corresponding to:

$$\varepsilon_{\mathrm{c}} = A\ln r_{\mathrm{s}} + B + r_{\mathrm{s}}(C\ln r_{\mathrm{s}} + D), \tag{4.22}$$

and in the case of the low-density limit, it corresponds to:

$$\varepsilon_{\mathrm{c}} = \frac{1}{2}\left(\frac{g_0}{r_{\mathrm{s}}} + \frac{g_1}{r_{\mathrm{s}}^{3/2}} + \dots\right), \tag{4.23}$$

where A, B, C, D and g_0, g_1 are parameterization coefficients fitted to numerical QMC data, and r_{s} is the dimensionless Wigner–Seitz parameter [68], defined as the radius of a sphere which encompasses exactly one electron. Being on the first rung of the ladder, regarding the simplicity of the LDA, it performs well for metallic, densely packed systems. Although, for systems with strong inhomogeneity in the charge distribution like molecules or surfaces, the accuracy is strongly diminished, thus necessitating gradient-based approaches.

Generalised Gradient Approximation (GGA) is on the second rung; the PBE functional is a widely used GGA that depends on the magnitude of the local electron density gradient. Hence, the electron density-dependent functional can be formulated as:

$$E_{\mathrm{x}}^{\mathrm{GGA}}[\rho] = \int \rho(\mathbf{r})\,\varepsilon_{\mathrm{x}}^{\mathrm{unif}}(\rho(\mathbf{r}))\,F_{\mathrm{x}}(s(\mathbf{r}))\,d\mathbf{r}, \tag{4.24}$$

with the dimensionless reduced density gradient defined as:

$$s(\mathbf{r}) = \frac{|\nabla\rho(\mathbf{r})|}{2k_{\mathrm{F}}(\mathbf{r})\rho(\mathbf{r})}, \qquad k_{\mathrm{F}}(\mathbf{r}) = \left(3\pi^2\rho(\mathbf{r})\right)^{1/3}, \tag{4.25}$$

where $k_{\mathrm{F}}(\mathbf{r})$ is the local Fermi wave vector acting as a scaling factor for the spatial variations of the density. The enhancement factor, $F_{\mathrm{x}}(s)$, is used to describe deviations

from a homogeneous electron gas. For PBE, it is written as [69]:

$$F_{\mathrm{x}}(s) = 1 + \kappa - \frac{\kappa}{1 + \mu s^2/\kappa}, \tag{4.26}$$

with the non-empirical fundamental constants defined as $\kappa = 0.804$, which satisfies the Lieb–Oxford bound constraint, and $\mu \approx 0.21951$, the effective gradient coefficient for exchange. PBE systematically improves binding energies and chemical energetics. Closely related, the meta-GGA functionals on the third rung of the ladder add the local kinetic energy density (τ), or the Laplacian of the density ($\nabla^2\rho$), to the electron density and its gradient ($\nabla\rho$) for electronic structure calculations.

Hybrid functionals fall on the fourth rung of the ladder. They can be classified as unscreened and range-separated (i.e., screened). The electron density-dependent exchange–correlation energy can be formulated for the case of PBE0, HSE, etc., as:

$$E_{\mathrm{xc}}^{\mathrm{hybrid}} = \alpha E_{\mathrm{x}}^{\mathrm{HF}} + (1-\alpha) E_{\mathrm{x}}^{\mathrm{PBE}} + E_{\mathrm{c}}^{\mathrm{PBE}}. \tag{4.27}$$

Hybrid functionals include a fraction of exact Hartree–Fock (HF) exchange (the standard value of the α parameter is 0.25) and improve the band-gap value which is closer to the experimental results in comparison to the functionals from the lower rungs like LDA and GGA. Although, it requires a higher computational cost. The total HF exchange energy is expressed as:

$$E_{\mathrm{x}}^{\mathrm{HF}} = -\frac{1}{2}\sum_{i,j}^{\mathrm{occ}} \iint \frac{\psi_i^*(\mathbf{r}_1)\psi_j(\mathbf{r}_1)\psi_j^*(\mathbf{r}_2)\psi_i(\mathbf{r}_2)}{|\mathbf{r}_1 - \mathbf{r}_2|} d\mathbf{r}_1\, d\mathbf{r}_2, \tag{4.28}$$

where the non-local integration calculates the exact exchange interaction between pairs of occupied spatial orbitals, effectively eliminating the spurious self-interaction error present in pure semi-local functionals.

4.1.7 Dispersion Corrections

Standard LDA, GGA, and hybrid functionals fail to fully capture long-range dispersion (van der Waals) interactions, which arise from correlated fluctuations of the electron density. These interactions are crucial for weakly bound molecular complexes, layered materials, and adsorption phenomena. A widely used correction to account for these in-

teractions is the semi-empirical Grimme-D3 scheme [70], which adds a damped pairwise dispersion term to the DFT energy:

$$E_{\text{DFT-D3}} = E_{\text{DFT}} + E_{\text{disp}}^{\text{D3}}, \tag{4.29}$$

with $E_{\text{disp}}^{\text{D3}}$ calculated as:

$$E_{\text{disp}}^{\text{D3}} = -\sum_{i<j} \sum_{n=6,8} \frac{C_{ij}^{(n)}}{R_{ij}^{n}} f_{\text{damp}}^{(n)}(R_{ij}), \tag{4.30}$$

where i and j run over all atomic pairs in the system, $n = 6$ and $n = 8$ denote the higher-order asymptotic multipole expansion terms, $C_{ij}^{(n)}$ are the geometry-dependent dispersion coefficients, R_{ij} is the interatomic distance, and $f_{\text{damp}}^{(n)}$ is a damping function ensuring the correction vanishes at short range to prevent double-counting of correlation effects already captured by the semi-local functional. The D3 correction is computationally inexpensive and has been widely adopted in molecular and solid-state simulations.

DFT provides an efficient and versatile framework for electronic structure theory. The Hohenberg-Kohn theorems guarantee that all ground-state properties are encoded in the density, while the KS formalism enables practical orbital-based implementations. The accuracy of any DFT calculation depends critically on the approximation chosen for $E_{\text{xc}}[\rho]$.

1. LDA is robust for structural properties but could lead to inaccuracy due to correlation energy calculation in inhomogeneous systems.

2. GGA (e.g., PBE) and meta-GGA balance accuracy and cost, and remain a default choice.

3. Hybrid functionals (e.g., PBE0) include non-local exchange and improve chemical energetics and band gaps, at higher cost.

4. Adaptive (e.g., D3) and non-local dispersion corrections are essential for incorporating long-range correlation effects [71].

4.1.8 Ab initio Molecular Dynamics

Under operating conditions, temperature induced structural dynamics can bring changes at the solid–liquid interface resulting in electronic fluctuations, altering the stability and functionality. Hence, analysing time-dependent phenomena requires a theoretical framework that can give insight into both atomic motion and the associated changes in electronic structure. *Ab Initio Molecular Dynamics* provides such an approach by directly coupling molecular motion with quantum-mechanical force evaluation.

In AIMD, the inter-atomic forces are computed at each simulation step from first-principles. The nuclear motion over time is resolved according to Newton's equations of motion, hence providing a time-resolved description of structural evolution, as used in classical molecular dynamics.

The motion of the nuclei is governed by the Lagrangian [72]:

$$L(\{\mathbf{R}_I\},\{\dot{\mathbf{R}}_I\}) = T(\{\dot{\mathbf{R}}_I\}) - V(\{\mathbf{R}_I\}) = \sum_I \frac{1}{2} M_I \dot{\mathbf{R}}_I^2 - E_{\mathrm{el}}(\{\mathbf{R}_I\}), \tag{4.31}$$

where M_I and $\mathbf{R}_I$ denote the mass and position of the nucleus I, and E_{el} is the electronic energy of the system obtained from DFT for the instantaneous atomic configuration. The resulting equations of motion,

$$M_I \ddot{\mathbf{R}}_I = -\nabla_I E_{\mathrm{el}}(\{\mathbf{R}_J\}), \tag{4.32}$$

are integrated numerically using schemes such as the velocity–Verlet or leapfrog algorithms [73], ensuring good energy conservation and stable trajectories over extended simulation times.

To mimic realistic thermodynamic conditions, thermostats are often introduced to control the temperature and enable sampling, corresponding to a canonical (NVT) ensemble. Common approaches include the Nosé–Hoover and Langevin thermostats, which regulate the kinetic energy of the nuclei by introducing friction and stochastic forces. In particular, the *adaptive Langevin thermostat* provides robust temperature control with minimal disturbance to the system's intrinsic dynamics [74]. It combines stochastic noise with a dynamically adjusted friction coefficient $\gamma(t)$ that is tuned based on the instantaneous kinetic energy of the system. The friction coefficient is automatically increased when the kinetic energy exceeds the target value and decreased when it falls

below, thus maintaining the set temperature without overdamping the natural motion of the atoms. AIMD is a powerful tool for exploring the finite-temperature behaviour of materials from first principles. It bridges the gap between static electronic structure calculations and experimental observations under dynamic, realistic conditions, thereby providing atomistic insight into the mechanisms governing surface stability, reactivity or energy conversion processes [75, 76].

4.1.9 Computational RAS

Reflection Anisotropy Spectroscopy is a non-destructive, linear optical probe highly sensitive to surface-induced anisotropies. It measures the normalized difference in the complex reflectivity r of light at normal incidence between two orthogonal in-plane crystal directions. For cubic(001) surfaces, these directions are typically $[\bar{1}10]$ and $[110]$. The RA signal is defined as:

$$\mathrm{RAS} := \frac{\Delta r}{r} = 2\frac{r_{[\bar{1}10]} - r_{[110]}}{r_{[\bar{1}10]} + r_{[110]}}, \quad r \in \mathbb{C}, \tag{4.33}$$

where $r_{[\bar{1}10]}$ and $r_{[110]}$ represent the complex reflection coefficients for light polarized along these specific orthogonal axes. This rendering makes RAS highly surface-sensitive, particularly to anisotropies arising from surface reconstructions or adsorbate ordering. From a theoretical perspective, RAS is connected to the anisotropy of the dielectric response function of the semi-infinite system.

According to the three-phase model devised by McIntyre and Aspnes [77], this response can be described by combining the individual dielectric functions of the bulk substrate, the surrounding vacuum, and a distinct surface layer characterized by an effective isotropic thickness d. For the case where $\Delta r \ll r$, the real part of the signal can be related to the reflectance R via $\mathrm{Re}(\frac{\Delta r}{r}) \approx \frac{1}{2}\frac{\Delta R}{R}$ and can then be expressed with respect to the anisotropy of the surface dielectric function $\Delta\varepsilon_\mathrm{s}$ as [78]:

$$\frac{\Delta R}{R} = \frac{4\pi d}{\lambda}\mathrm{Im}\left[\frac{\Delta\varepsilon_\mathrm{s}}{\varepsilon_\mathrm{b} - 1}\right], \tag{4.34}$$

where λ is the wavelength of the incident light, and ε_b is the bulk dielectric function. Expanding this to separate the real and imaginary components of the anisotropic surface

dielectric tensor ($\Delta\varepsilon_s'$ and $\Delta\varepsilon_s''$, respectively) yields:

$$\frac{\Delta R}{R} = \frac{4\pi d}{\lambda}\left(A\,\Delta\varepsilon_s'' - B\,\Delta\varepsilon_s'\right), \tag{4.35}$$

where the weighting parameters A and B are defined by the real (ε_b') and imaginary (ε_b'') components of the bulk dielectric function:

$$A = \frac{\varepsilon_b' - 1}{(1-\varepsilon_b')^2 + (\varepsilon_b'')^2}, \quad B = \frac{\varepsilon_b''}{(1-\varepsilon_b')^2 + (\varepsilon_b'')^2}. \tag{4.36}$$

At the microscopic level, the surface anisotropy is obtained from Independent-Particle Random Phase Approximation (IP-RPA) calculations that neglect local field effects. For an idealized, symmetric slab, the imaginary part of the half-slab polarisability along the x-axis (corresponding to $[\bar{1}10]$) is written as:

$$\mathrm{Im}[4\pi\alpha_{xx}^{\mathrm{hs}}(\omega)] = \frac{4\pi^2 e^2}{m^2\omega^2\mathcal{A}}\sum_{\mathbf{k}}\sum_{v,c}\left|P^x_{v\mathbf{k},c\mathbf{k}}\right|^2 \times \delta(E_{c\mathbf{k}} - E_{v\mathbf{k}} - \hbar\omega), \tag{4.37}$$

where e and m are the fundamental electron charge and mass, $\mathcal{A}$ is the surface area, ω is the photon frequency, and δ represents the Dirac delta function. The term $P^x_{v\mathbf{k},c\mathbf{k}}$ represents the transition matrix element of the momentum operator between the occupied valence (v) and unoccupied conduction (c) Kohn-Sham (KS) single-particle states at wave vector $\mathbf{k}$.

Evaluating this polarisability requires explicit input of the KS eigenvalues and wavefunctions from ground-state DFT. However, if the simulated slab profile is non-symmetric, a real-space cutoff approach using a step-like window function $\theta(z)$ is required to cleanly isolate the surface response. The modified, non-local matrix elements are constructed as follows [79]:

$$\tilde{P}^x_{v\mathbf{k},c\mathbf{k}} = -i\int d\mathbf{r}\,\psi^*_{v\mathbf{k}}(\mathbf{r})\,\theta(z)\,\frac{\partial}{\partial x}\,\psi_{c\mathbf{k}}(\mathbf{r}), \tag{4.38}$$

and the corresponding half-slab polarisability transforms into:

$$\mathrm{Im}[4\pi\alpha_{xx}^{\mathrm{hs}}(\omega)] = \frac{8\pi^2 e^2}{m^2\omega^2\mathbf{A}}\sum_{\mathbf{k}}\sum_{v,c}\mathrm{Re}\left[\left(P^x_{v\mathbf{k},c\mathbf{k}}\right)^*\tilde{P}^x_{v\mathbf{k},c\mathbf{k}}\right] \times \delta(E_{c\mathbf{k}} - E_{v\mathbf{k}} - \hbar\omega). \tag{4.39}$$

In practice, this IP-RPA post-processing framework (e.g., via the YAMBO code [80]) systematically underestimates optical excitation energies. This deficiency stems funda-

mentally from the unphysical self-interaction error and the missing derivative discontinuity in standard semi-local exchange-correlation functionals, resulting in an incorrect semiconductor band gap. To correct this limitation for semiconductors and insulators, a empirical scissors shift operator is rigidly applied to the KS eigenvalues to shift the conduction bands upward, enabling accurate comparison with experimental RAS measurements.

4.2 Ab initio Thermodynamics

In this work, the Gibbs free surface energy ($\gamma = \Delta G/A$) is used to assess the thermodynamic stability of different reported surface reconstructions of InP(001). A lower γ value results in the stability of a surface reconstruction. The general formula for γ is given by:

$$\gamma(T,p) = \frac{1}{A}\left(G(T,p,N_i) - \sum_i N_i\mu_i(T,p)\right), \tag{4.40}$$

where T and p denote temperature and pressure, N_i represents the number of atoms of a particular surface constituent species i, and μ_i is its corresponding chemical potential. Here, G is the Gibbs free energy of the slab, and A is the total surface area of the cell. While G in principle depends on temperature and pressure, it is often simply approximated in ab initio-based approaches by the calculated total electronic energy of the corresponding slab (E_{slab}), thus neglecting vibrational entropy and volume changes. Moreover, the chemical potential is frequently normalised with respect to the bulk energies of the respective elements ($\Delta\mu_i(T,p) = \mu_i(T,p) - E_{i,\text{bulk}}$). This equation then can be represented as:

$$\gamma(T,p) = \frac{1}{A}\left(E_{\text{surf}} - \sum_i N_i\Delta\mu_i(T,p)\right), \tag{4.41}$$

where E_{surf} is the normalized surface energy contribution derived from subtracting the reference bulk energy from the slab's total electronic energy. Under equilibrium, the surface constituents' chemical potentials, i.e., μ_{In} and μ_{P}, are connected via the bulk formation energy of InP, which can be exploited:

$$\mu_{\text{In}} + \mu_{\text{P}} = \mu_{\text{InP,bulk}} = \mu_{\text{In,bulk}} + \mu_{\text{P,bulk}} + \Delta H_{\text{f}}^{\text{InP}}. \tag{4.42}$$

Hence, the surface free energy can be expressed as a function of a single variable, $\Delta\mu_{\mathrm{In}}$. The range for $\Delta\mu_{\mathrm{In}}$ is constrained by the experimentally determined InP formation energy, which is -0.81 eV, yielding $\Delta H_{\mathrm{f}}^{\mathrm{InP}} \leq \Delta\mu_{\mathrm{In}} \leq 0$, where the lower bound corresponds to P-rich conditions and the upper bound signifies In-rich conditions. After determining the phase stability of clean surface reconstructions as a function of $\Delta\mu_{\mathrm{In}}$, the overall phase stability upon oxygen exposure can be represented as a function of $\Delta\mu_{\mathrm{In}}$ and $\Delta\mu_{\mathrm{O}}$, where the oxygen chemical potential can usually be determined as a function of partial pressure p and temperature T:

$$\Delta\mu_{\mathrm{O}}(p,T) = \frac{k_{\mathrm{B}}T}{2}\left[\ln\left(\frac{p\lambda^3}{k_{\mathrm{B}}T}\right) - \ln Z_{\mathrm{rot}} - \ln Z_{\mathrm{vib}}\right] - \frac{1}{2}E_{\mathrm{O}_2}\,. \tag{4.43}$$

Herein, k_{B} is the Boltzmann constant, λ is the de Broglie thermal wavelength of the O_2 molecule, while Z_{rot} and Z_{vib} are the rotational and vibrational partition functions of the gas-phase O_2 molecule, respectively. E_{O_2} represents the total energy of the oxygen molecule in its computational spin-triplet ground state. For determining the overall phase stability, the surface energy ($\gamma(\Delta\mu_{\mathrm{In}},\Delta\mu_{\mathrm{O}})$) has to be mapped onto the x–y plane ($\Delta\mu_{\mathrm{In}}$,$\Delta\mu_{\mathrm{O}}$).

4.3 Computational Details

Investigation into the structural stability and time–resolved reflection anisotropy of InP(001) interfaces are carried out via first principles calculations. The system buildup and computational configuration are established as follows:

1. Code: Phase stability and AIMD analysis are performed using CP2K [65]. Subsequent RA-spectra of equilibrated trajectories are calculated via the Yambo code [80, 81]. Yambo requires ground-state wave functions from a plane wave DFT code, which are provided via QUANTUM ESPRESSO [64].

2. System setup: Calculations initiated from the experimentally reported zinc-blende InP bulk structure, where systematic convergence tests regarding slab thickness, vacuum size, and k-point grids are conducted using a $\sqrt{2}\times\sqrt{2}$ cell layout. Based on these convergence tests, the (2×4) and (2×2) based surface reconstructions were modelled using asymmetric slab geometries.

3. Slab Structure: The asymmetric InP(001) slabs comprise 12 atomic layers alternating as 6 In and 6 P layers. To prevent nonphysical interactions between periodic image replicas along the surface normal, a vacuum region of $\sim$ 36 and 20 Å was included for the analysis of phase stability (paper *A1*) and surface dynamics (paper *A2*) resp. During geometry optimisation, the bottom 3 In and 2 P layers were fixed, with the bottom-most In-layer passivated using pseudo-hydrogen atoms (Z=1.25) to prevent the formation of an internal electric field arising from charge imbalance, thereby avoiding the artificial creation of spurious surface states.

4. XC-functional: The PBE functional is used to describe the exchange-correlation effects during the phase stability and AIMD simulations (paper *A1,A2*). For the subsequent optical response calculations, electronic band structure benchmarks are obtained via hybrid PBE0 XC-functional for a representative mid-trajectory snapshot in the equilibrated phase. The resulting scissors-shift parameters are then applied uniformly across the PBE-derived electronic ground-state structures for all trajectory snapshots to compute the time-resolved RA-spectra within the Independent-Particle Random Phase Approximation (IP-RPA) without local field effects (paper *A2*).

5. Dispersion Correction: Semi-empirical Grimme-D3 corrections are applied across phase stability and AIMD simulations to account for long-range Van der Waals interactions (paper *A1,A2*).

6. Pseudopotentials: Non-local, norm conserving GTH-PBE pseudopotentials are eomployed to describe the electron–core interactions during the phase stability and AIMD calculations (paper *A1,A2*), for the ground-state electronic structure and subsequent RA-spectra calculations, Optimised Norm-Conserving Vanderbilt (ONCV) pseudopotentials are utilised (paper *A2*).

7. Basis Sets: For the CP2K-based mixed Gaussian plane-wave (GPW) calculations, the DZVP basis set is used for the phase stability analysis (paper *A1*), while the more extended TZV2P basis set is used for the AIMD simulations (paper *A2*). These configurations utilise a plane-wave kinetic energy cutoff of 400 Ry and a relative cutoff of 60 Ry, Conversely, for the subsequent post-processing optical response calculations an explicit expansion of the wave-functions, a pure plane-wave

basis formulation is employed with a kinetic energy cutoff of 60 Ry is employed to obtain the electronic band structure.

8. solid–liquid interface modelling: To incorporate the impact of an aqueous environment, stable surfaces at specific $\Delta\mu_{\mathrm{In}}$ chemical potentials are solvated using seven layers of water, This corresponds to the inclusion of 58 H_2O molecules for the (2×2) surface cells and 116 H_2O molecules for the larger (2×4) surface reconstructions, respectively.

9. AIMD simulations: Prior to AIMD simulations, both the solid–liquid and solid–vacuum interfaces are geometrically optimised to achieve a stable starting configuration. Thereon, AIMD trajectories are simulated within the canonical ensemble (NVT) at a temperature of 300 K, regulated by an Adaptive Langevin thermostat with a integration time step of 0.5 fs. Each simulation are ran for $\sim$ 20 ps, which includes system-dependent equilibration windows (paper *A2*).

10. Band gap corrections: Calculation of the optical response requires a precisely defined electronic structure. To mitigate the band gap underestimation inherent to the semi-local PBE XC-functional, an empirical scissors operator correction (Eqs. (9.1) and (9.2)) is applied and is applied to align the PBE-derived valence and conduction bands with the bands obtained from the hybrid PBE0 functional. This approach is justified since, once the system attains structural equilibrium, minor fluctuations in the principal thermodynamic variable (e.g. T) exert a negligible impact on the ground-state surface electronic properties.

11. Optical anisotropy: For the RAS calculations, IP-RPA framework (Sec. 4.1.9) is employed to evaluate the half-slab dielectric polarisability contributions.. A real-space cutoff is applied such that only the topmost four atomic layers of the InP(001) slab contribute to the optical spectrum. To capture the impact of thermal and structural fluctuations on the electronic structure, AIMD snapshots are extracted every 500 fs for the subsequent determination of the time–resolved optical anisotropy.

5 Results

This section represents the results published in publication *A1*. Herein, the structural and thermodynamic stability of InP(001) surface reconstructions–both for clean surfaces and under oxygen exposure–is investigated using first-principles calculations. Determining their stability in aqueous and oxidising environments remains an ongoing challenge due to the complexities of surface oxidation and defect formation.

The clean surface phase diagram of InP(001) is analysed, identifying five stable reconstructions. These are predominantly P-terminated structures under P-rich conditions, such as (2×2)-2D, and c(4×4) reconstructions. The $\alpha 2(2\times 4)$ and $\beta 2(2\times 4)$ reconstructions are found to be stable under intermediate $\Delta\mu_{\mathrm{In}}$ chemical potential, whereas the mixed-dimer (2×4) surface is stable under In-rich conditions. Subsequently, the additive adsorption of oxygen atoms onto these stable surface reconstructions is evaluated to map the overall phase stability with respect to the chemical potentials of the surface constituents. Structural analysis indicates that oxygen binding preferentially occurs on P-rich surfaces, driving the formation of experimentally reported polyphosphate P_xO_y motifs [82]–specifically the In(P_2O_7) species, which is theoretically established in this study [83]. Conversely, the commonly cited In-rich mixed-dimer surfaces become thermodynamically unstable across a broad range of chemical potentials. These findings imply that the surface passivation and oxidation pathways of InP are governed by polyphosphate formation rather than indium-oxide-like bonding [36].

5.1 Phase Stability of InP(001) surfaces

Theoretical analysis of the surface chemistry and phase stability of P- and In-rich InP(001) reconstructions—including the (2×2)-1D, (2×2)-2D, c(4×4), $\alpha 2(2\times 4)$, $\beta 2(2\times 4)$, and mixed-dimer (2×4) structures–has been previously reported [33]. Early models relied on the *Electron-Counting Rule* alongside surface dimer formation as guiding principles to explain several of these observed phases [84, 85]. For InP(001), combined experimental and first-principles studies have identified a characteristic set of surface structures: under In-rich conditions, the surface forms a mixed-dimer (2×4) configuration, whereas intermediate conditions favor the stepped $\alpha 2(2\times 4)$ and $\beta 2(2\times 4)$ reconstructions, and more P-rich preparation conditions yield (2×2)-based and c(4×4) structures.

Taking these previous investigations into consideration, our resulting phase diagram

confirms the existence of five stable reconstructions (Fig. 5b). These reconstructions can be classified into two distinct categories based on whether dimer formation occurs on an underlying In-terminated or P-terminated sublayer, as theoretically established in a recent study [83]. When compared directly to Schmidt's LDA-based phase diagram (Fig. 5a) [33], our results shift the stability window of the P-rich (2×2)-1D reconstruction, which appears slightly unstable in the present PBE-based phase diagram (Fig. 5b). This deviation can likely be attributed to differences in the exchange-correlation treatment, as well as the explicit inclusion of the semi-empirical Grimme-D3 dispersion correction to the PBE functional in the present study.

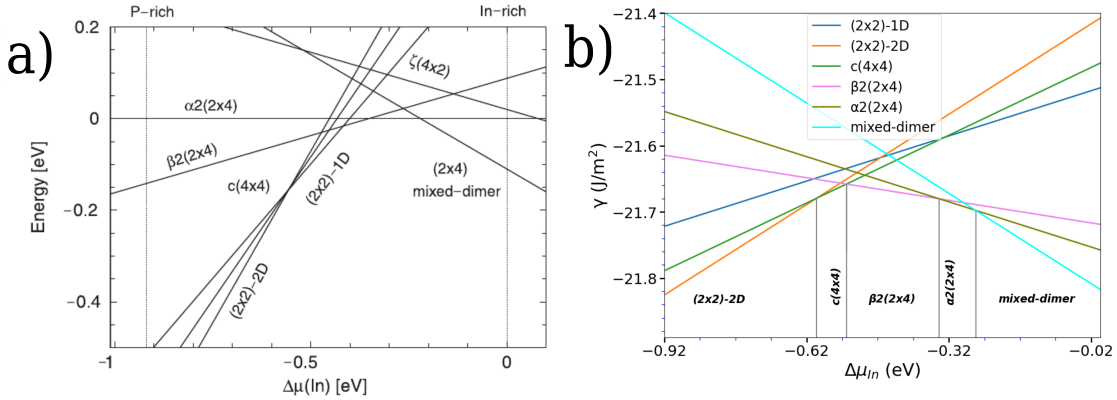

Figure 5: Phase stability diagram of InP(001) surface reconstructions, Sub-figures a, b corresponds to LDA- and PBE-D3 derived phase diagrams. Sub-figure (a) is taken from ref. [33], while sub-figures b is take from the paper *A1*.

In the P-rich region, the stable configurations fall into the P-terminated sublayer category and include the (2×2)-2D and c(4×4) structures. Both are characterized by the formation of P–P dimers on the surface: the (2×2)-2D reconstruction exhibits two P–P dimers per unit cell, while the c(4×4) reconstruction consists of three P–P dimers arranged within a $\sqrt{2} \times \sqrt{2}$ surface unit cell that is rotated by 45° with respect to the conventional one (Fig. 6a). At intermediate chemical potentials, stepped reconstructions situated on an In-terminated sublayer are stable. Namely, the $\beta 2(2 \times 4)$ surface comprises three P–P dimers, with two dimers occupying the upper plateau and one dimer located on the lower terrace. Similarly, the $\alpha 2(2 \times 4)$ surface exhibits a distinct step-edge configuration containing only one dimer on the upper plateau and one dimer on the lower terrace (Fig. 6b). Toward In-rich conditions, the stable structure transitions to a mixed In–P dimer reconstruction, which is also structurally supported by the underlying

In-terminated sublayer.

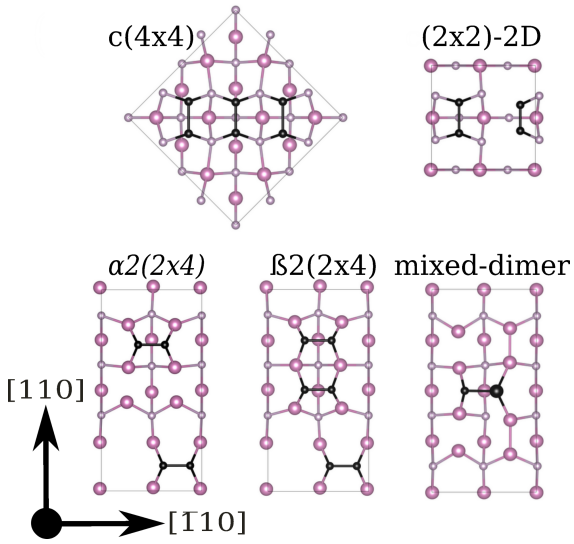

Figure 6: Stable InP(001) surface reconstructions, viewed along the (001) plane. Surface dimers, i.e. P–dimers and dimers are indicated in dark-grey. In and P are indicated by pink, and grey spheres. This figure is taken from paper *A1*.

5.1.1 Oxygen Passivation

It is essential to understand the distinct behaviour of oxygen addatom adsorption on InP(001) surfaces after ascertaining the thermodynamic stability of the (Sec. 5.1). For this purpose an analysis identifying the favourable sites for oxygen insertion and adsorption is important. This is achieved by a constrained relaxation of a single oxygen atom placed across a grid of surface sites while keeping all atoms in the slab fixed, thereby producing a potential energy surface mapped as a heat of formation(ΔH_f) colour map. As shown in Fig. 7, oxygen atoms preferentially adsorb onto P atoms, specifically targeting surface dimers and sites in the vicinity of step edges. This preference for P-atom adsorption remains consistent even on the In-rich mixed-dimer surface. According to the phase stability analysis, increasing the total oxygen content on the mixed-dimer reconstruction favours the formation of In-O-In bonds with the neighbouring atoms, alongside oxygen insertion into the underlying P-layer situated below the In-termination (Sec. 5.1.3). Conversely, P-rich surfaces such as $\beta 2(2\times 4)$ and c(4×4) phases exhibit highly negative ΔH_f values directly on the P-P dimer sites. Similar to the In-rich surface, the addatom adsorption process on these P-rich surfaces involves favourable O-atom insertion into

the In–P back bonds, driving the formation of bridging In-O-P networks. Crucially, this mechanism of oxygen insertion into the back bonds is consistent with experimental and theoretical observations in the literature [86, 38].

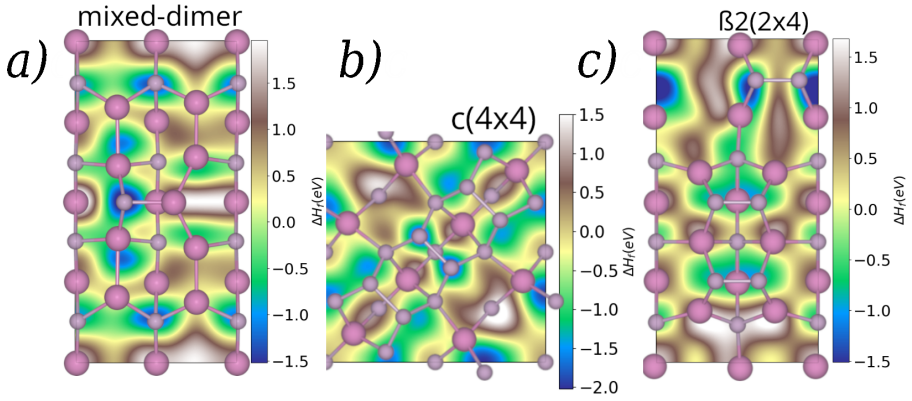

Figure 7: Potential energy surfaces for oxygen adsorption on different InP(001) surface reconstructions (heat of formation colour map). Sub-figures a,b, and c corresponds to mixed-dimer, c(4×4), and $\beta 2(2 \times 4)$ reconstruction. In and P atoms are constrained, whereas O is allowed to relax along the surface normal. This figure is taken from paper *A1*.

From these initial constrained simulations, it becomes evident that, across both P-rich and In-rich reconstructions, oxygen preferentially binds to P–P dimer sites or the underlying P-terminating layer as the total oxygen content increases.

5.1.2 Oxygenation Approach

To investigate the findings regarding the structure-sensitive oxidation of InP(001) upon exposure to oxygen or water [19, 34, 86, 87], two complementary strategies are employed: a step-wise screening method and an motif-transfer method.

The first approach is the step-wise screening method, in which individual O atoms are sequentially placed above the surface and relaxed at specific positions informed by the prior potential energy surface heatmap analysis. In this approach, the oxygen and substrate surface atoms are left unconstrained during geometry optimization. The most favorable position for each additional O addatom is chosen on the basis of the lowest calculated ΔH_f. Stable surfaces are thus iteratively occupied until the surface becomes fully passivated, avoiding the formation of surface-bound O_2 molecules or the emergence of significant structural distortions. This step-wise approach provides direct insight into the

sequential formation of indium polyphosphate motifs (P_xO_y) via the following mechanism:

1. Adsorption onto P–P dimers leading to the formation of P–P–O networks.

2. Adsorption onto an available vacant site, forming O–P–P–O configurations. Additionally, at higher coverage, O-atom deposition onto an existing P_xO_y motif leads to the formation of a 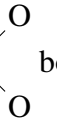 bonding state.

3. Charge depletion and a concurrent increase in the P–P bond length, leading to oxygen insertion and the formation of a bridging P–O–P bond.

4. Consequent adsorption driving oxygen insertion into the underlying In–P back bonds.

As the surface addatom coverage increases during step-wise screening, the surface layer tends to distort, characterized by significant in-plane displacement of the underlying P- or In-layers or an upward shifting of the P_xO_y motif along surface normal. This distortion ultimately suppresses further oxygen insertion into the P-back bonds, an effect observed predominantly for P–P dimers situated on the underlying P-termination (Fig. 8a).

The second approach is the extrapolation method, which utilises a motif-transfer scheme to bypass the structural distortions encountered during high-coverage sequential screening. A combination of these approaches is required for full surface passivation because the techniques used to achieve maximum coverage on the stepped $\beta 2(2\times 4)$ reconstruction cannot always be directly translated to other surfaces. For example, the $\alpha 2(2\times 4)$ surface—an equivalent stepped phase but with only two surface P–P dimers—possesses exposed In atoms in the underlying layer that tend to form competing In_xO_y species. Similarly, the P-terminated planar c(4×4) and (2×2)-2D surfaces contain three and two P–P dimers, respectively, requiring an alternate pattern. Finally, the mixed-dimer surface lacks surface P–P dimers altogether, necessitating a distinct scheme to achieve full passivation. To address these variations, the following extrapolation pathways are utilised to systematically construct and optimize passivated surface models:

1. Simultaneous motif transfer: The concurrent deposition of a specific polyphosphate motif onto all equivalent surface sites at once. For example, all three P–P

dimers of the $\beta 2(2 \times 4)$ reconstruction are covered with P_2O_7 motifs simultaneously, followed by full geometry optimization to verify if the surface remains stable and retains its characteristic surface chemistry.

2. Sequential motif transfer: The systematic transfer of a P_2O_5 motif (derived from the step-wise approach) onto a stable surface that already hosts the same or a different P_xO_y unit, resulting in extended configurations such as $(P_2O_5)_2$ (Fig. 9). Note that for the clean P-rich (2×2) surface, this motif-transfer scheme is carried out exclusively (Fig. 9b).

3. Systematic build-up: A hybrid implementation of step-wise deposition and motif-transfer, proceeding with the ideal deposition of structural motifs onto stable intermediate surfaces previously identified via the sequential step-wise approach (Fig. 9, top-left).

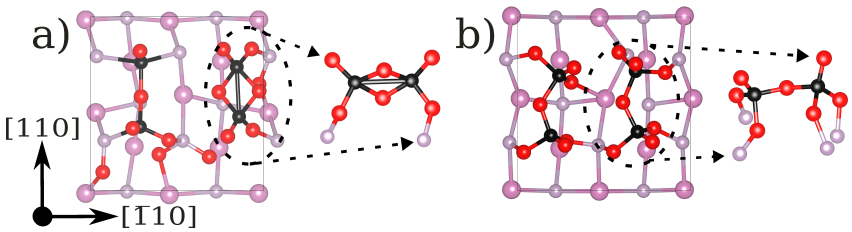

Figure 8: Representative surfaces obtained during oxygen adsorption for (2×2)-2D, along-with side-view cutouts of the right-hand P_xO_y motif. (a) Top view of the oxygenated phase obtained during sequential screening, illustrating distorted surfaces with emerging polyphosphate units. (b) Top view of the oxygenated phase generated by further extrapolation, showing the relaxed structure after deposition on favourable sites and the stabilisation of (P_xO_y) motifs.

These combined approaches are used to identify the most favorable stable surface geometry possessing the lowest ΔH_f at any given target oxygen coverage. Figure 9 provides a visual representation of a ten-oxygen-atom adsorption workflow on two classes of stable surface reconstructions: those with dimer formation on the P-rich (2×2) or the (2×2)-2D phases. This systematic framework reveals the various pathways available to evaluate thermodynamic stability at a specific oxygen coverage. For instance, in the case of the (2×2)-2D reconstruction, multiple distinct structural options are evaluated (Fig. 9a). Conversely, for the P-rich (2×2) reconstruction, a direct combination of motif transfer steps is used exclusively to achieve the target ten-oxygen-atom coverage (Fig. 9b). This

ten-oxygen-atom scenario serves as a representative benchmark highlighting how different pathways are leveraged to locate the global minimum of ΔH_f. It further illustrates the interaction of P-rich surfaces with oxygen and showcases how passivation pathways for higher oxygen contents are computationally determined.

Crucially, both the step-wise and motif-transfer methods converge on the conclusion that P_xO_y species–particularly the P_2O_7 motifs–represent the thermodynamically most stable oxygenated configurations from moderate to high oxygen coverage. These motifs incorporate oxygen through the formation of P–O, P–O–P, and specifically bridging In–O–P bonds for cases involving P–P dimers on an underlying In-termination, which fundamentally reflects the preferential affinity of oxygen adsorption toward surface P–P dimers.

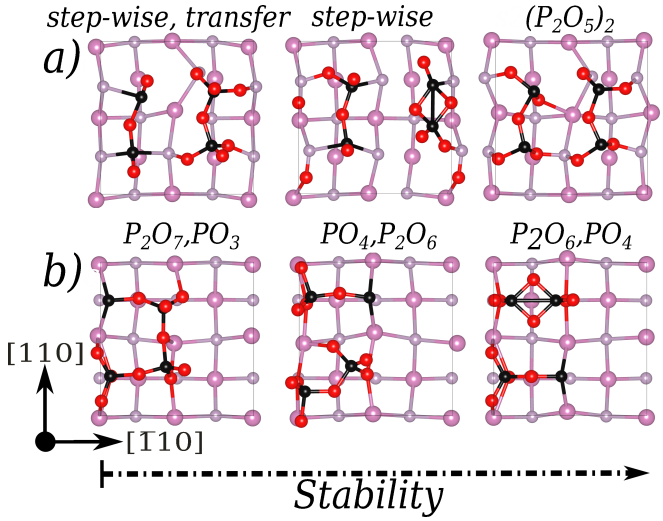

Figure 9: Representation of P_xO_y motif formation for the adsorption of ten oxygen atoms. The figure is organised into two rows: (a) shows adsorption on the (2×2)-2D reconstruction, and (b) shows adsorption on the P-rich (2×2) surface. The axis at the bottom denotes lower ΔH_f and hence higher stability, as one moves along the right for both (2×2) and (2×2)-2D phases.

It is worth noting that for the (2×2)-2D surface, it is difficult to directly transfer the P_2O_7 motifs onto the clean clean surface as isolated single units. This difficulty arises because the two surface dimers differ inherently in their initial bond lengths and spatial positions relative to the underlying P-layer, making uniform motif-transfer challenging. Therefore, following the initial formation of two local P_2O_5 motifs, additional oxygen is explicitly inserted into the P-back bonds to arrive at full coverage via two distinct

P_2O_7 motifs. This hybrid approach successfully allows the surface to retain its macroscopic symmetry despite significant local displacement of surface atoms–an effect observed uniquely for the (2×2)-2D surface–provided alternative approaches to passivate the surface are systematically implemented.

For the In-rich mixed-dimer surface, direct motif extrapolation is entirely impossible due to the total absence of surface P–P dimers. Following the sequential step-by-step oxygen coverage approach instead, the surface effectively retains its initial in-plane structural arrangement of surface atoms at low coverage. However, beyond a critical threshold of oxygen coverage, the underlying In- or P-atomic layers begin to exhibit substantial vertical and horizontal displacements. This distortion can be attributed to oxygen insertion toward the bulk, leading to the formation of bridging In–O–P bonds, which have also been reported experimentally [86].

5.1.3 Phase Stability of InP(001) upon oxygen exposure

Finally, the combination of the approaches discussed above provided an insight into the thermodynamic phase stability of each surface reconstruction with respect to $\Delta\mu_O$. The resulting stability trends are evaluated by calculating the surface energy (γ) as a function of $\Delta\mu_O$ and $\Delta\mu_{In}$ (Fig. 10). These results highlight that the oxygen-rich stable configurations—specifically those saturated by the P_xO_y motifs—are thermodynamically favorable.

Regarding the (2×2)-2D phase, the configuration featuring two P_2O_7 motifs (Fig. 12b) spans the phase diagram for $\Delta\mu_O > -2.5\,\text{eV}$ as one moves toward the P-rich limit ($\Delta\mu_{In} < -0.4\,\text{eV}$). Conversely, low oxygen coverage (3 and 4 O-atoms) fall outside the overall stability region, appearing only in a narrow region where $\Delta\mu_{In} < 1.05\,\text{eV}$ near the metallic phosphorus boundary, as illustrated in Fig. 12a. Interestingly, for oxygen contents up to 7 atoms, stable phases are achieved solely via the step-wise screening (Fig. 10a). This highlights that due to the distinct features of the two P–P dimers, a combination of both approaches had to be used to accurately map the stability. For the $c(4\times4)$ reconstruction, scanning the stable configurations for a specific O-content is done only via the P_xO_y motif-transfer approach, similar to the P-rich (2×2) surface. Regardless of the different structural motifs investigated, the results (Fig. 10b) indicate that none of the $c(4\times4)$ configurations occupy a region of stability in the overall phase diagram (Fig. 12). Upon comparing Figs. 10a,b, the adsorption energy γ^{ad} across a wide range of $\Delta\mu_O$ is higher

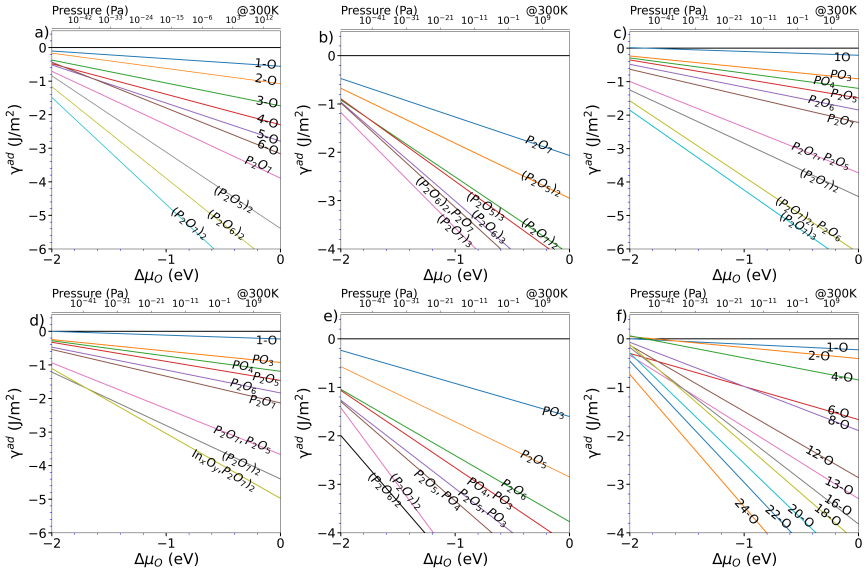

Figure 10: Surface energy with respect to oxygen chemical potential of the energetically favourable O adsorption sites for (a) (2×2)-2D, (b) c(4×4), (c) $\beta2(2\times4)$, (d) $\alpha2(2\times4)$, (e) P-rich (2×2), and (f) mixed-dimer surface reconstructions. Sub-figure(a,c,e–f) are taken from paper *A1*.

for the case of the fully passivated $c(4\times4)(P_2O_7)_3$ compared to the (2×2)–2D$(P_2O_7)_2$ phase.

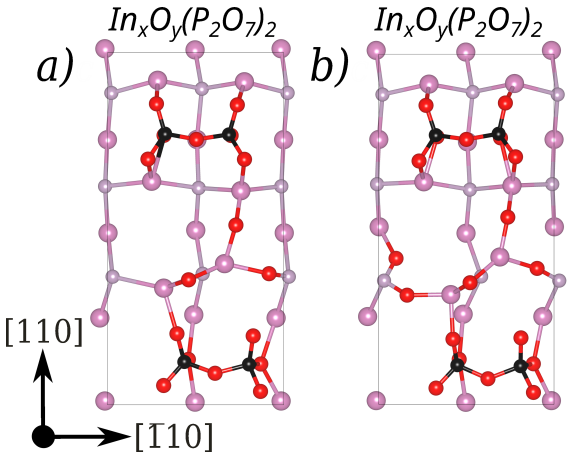

Figure 11: Surface structure of the $\alpha2(2\times4)$ reconstruction beyond the 14 O-atom coverage limit, illustrating the saturation of P–dimer and the subsequent formation of In_xO_y species.

As the most extensively studied surface in this work, the $\beta2(2\times4)$ reconstruction

accommodates multiple structural combinations via the motif-transfer approach due to the availability of three distinct surface P–P dimers. Through this systematic evaluation, it is found that the surface reaches its maximum passivation coverage at a content of 21 oxygen atoms, which corresponds to the complete saturation of all three P–P dimers with P_2O_7 motifs (Fig. 12b). This 21-O phase represents the most stable configuration across the entire experimentally accessible P-rich region ($\Delta\mu_{\mathrm{In}} < 0\,\mathrm{eV}$) within the overall phase diagram. Furthermore, while intermediate configurations hosting only one or two P_2O_7 motifs (equivalent to lower oxygen contents) are also found to be thermodynamically stable, they are restricted to narrow domains of the oxygen chemical potential (Fig. 12). Similarly, the $\alpha 2(2\times 4)$ surface—which has one less P–P dimer than the $\beta 2$ reconstruction—reaches maximum passivation when both of its dimers are covered with P_2O_7 motifs at a 14-O atom limit (Fig. 10d). Further adsorption beyond this stage occurs near the In-layer of the upper terrace, creating In_xO_y species such as In_2O_3 that slightly distort the underlying In-termination, with full structural saturation eventually achieved at 17 O-atoms (Fig. 11). However, despite accommodating these configurations, this specific reconstruction does not hold a stable region in the overall phase diagram because it remains energetically less stable than competing phases (Fig. 12a). This lack of a stable domain confirms that such indium oxide formations are thermodynamically unstable under equilibrium conditions compared to the dominant polyphosphate phases, a finding consistent with experimental observations indicating that indium oxides are easily removed or unstable on these treated surfaces [36]. For the P-rich (2×2) phase, stable configurations are found solely via the motif-transferring approach (Fig. 10e). The resulting phases feature $(P_2O_6)_2$ and $(P_2O_7)_2$ motifs (Fig. 12b), appearing as stable phases in the overall phase diagram for $\Delta\mu_{\mathrm{O}} > -2.5\,\mathrm{eV}$, and within the range $-1.9 < \Delta\mu_{\mathrm{In}} < 0.9\,\mathrm{eV}$. These two configurations occupy a vast region of the overall phase diagram (Fig. 12a). Furthermore, the surface exhibited minimal surface distortion, equivalent to the $\beta 2(2\times 4)$ surface, and is well suited for accommodating these polyphosphate motifs without significant strain on the underlying layers.

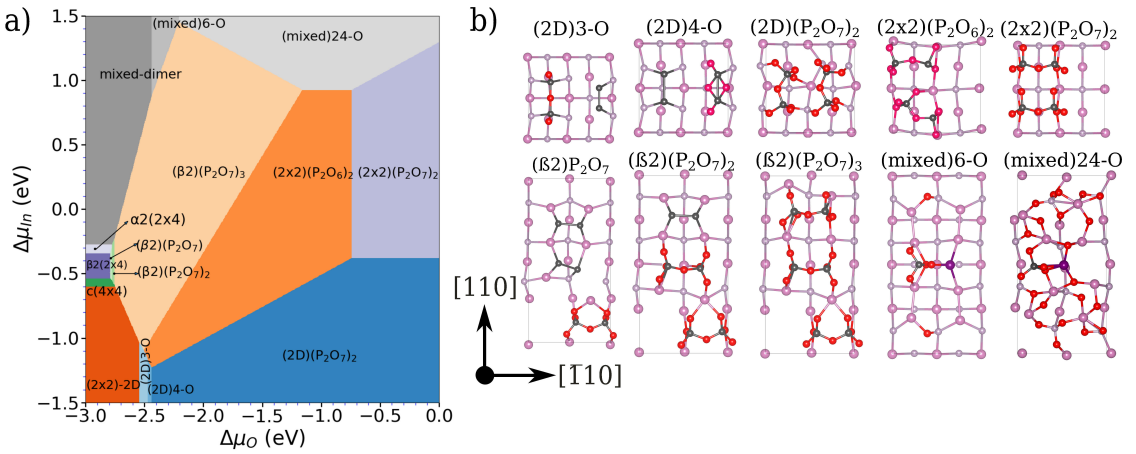

Figure 12: (a) Overall phase diagram of oxygenated InP(001) surfaces, as a function of indium and oxygen chemical potentials. P_xO_y-containing P-rich surfaces dominate the stability region, whereas In-rich mixed-dimer phases are restricted to the near-metallic limit, (b) Ball-and-stick representation for InP(001) oxygenated surface reconstructions, viewed along the (001) direction. To distinguish between the types of dimers, surface P–dimers are shown in dark grey, and dimers are represented with a magenta-grey pattern. In, P, and O atoms are shown in pink, grey, and red spheres respectively, this figure is take from the paper *A1*.

An additional calculation is done by transferring the motifs to achieve a $(P_2O_7)_3$ coverage on the P-rich (2×2) phase. This is performed by extending the surface along the [110] direction to form a P-rich (2×4) surface with four P–P dimers; however, the results indicated that this configuration remains unstable. The difficulty in identifying a stable configuration can be attributed to the topological constraints of the potential energy surface (PES). The optimization of the surface to find a local minimum is highly dependent on the *initial guess* of the oxygen atomic positions. The placement of oxygen atoms—whether on a clean surface or as coverage increases—largely determines the height of barriers on the PES. This indicates the extent of cumulative atomic displacement required for surface atoms to invoke changes in bond lengths and angles to reach the minimum. Consequently, if the initial guess for the positions of a single atom, a motif, or a combination of motifs is sub-optimal, the system may converge to an incorrect local minimum or a saddle point.

Lastly, the In-rich mixed-dimer structures become energetically stable for 6 and 24 O-atom coverage (Fig. 12b) when $\Delta\mu_{\mathrm{In}} > 0.88\,\mathrm{eV}$. However, this stability domain represents unrealistically In-rich and O-poor conditions, closely approaching the stability

limit of metallic indium. Thus, the emergence of P_xO_y motifs, and particularly P_2O_7, can be regarded as the central mechanism for stabilizing the InP(001) surface under oxygen exposure.

5.2 Time–Resolved Reflection Anisotropy Spectroscopy

This section presents the results published in Publication *A2*. Herein, we analyze the structural dynamics of pristine and oxygenated InP(001) surfaces in vacuum and in explicit contact with H_2O via AIMD simulations at 300 K. The impact of these structural modifications on the optical anisotropy is subsequently determined via computational RAS. This dual approach provides critical insights into atomic re-ordering and the structural impact of adsorption/desorption processes at the solid–water interface, which are highly relevant for stable (photo-)electrode design. The inherent phase transformations (Sec. 5.1) and surface passivation mechanisms under electrochemical environments—frequently involving the adsorption of P_xO_y motifs (Sec. 5.1.3)—can drastically alter the electronic structure of the surface, and, consequently, its optical response. Therefore, combining AIMD simulations with computational RAS allows for a detailed analysis of these underlying interface phenomena at atomistic lengths and femtosecond timescales. However, when evaluating these dynamic properties and their resulting optical spectrum, one must explicitly take into consideration the systematic limitations of semi-local functionals, finite supercell sizes, and AIMD timescales, as detailed extensively in Sec. 9.1.

Solid–liquid and solid–vacuum interfaces of the stable InP(001) reconstructions identified in Publication *A1* are investigated at specific indium chemical potentials. In particular, we examine the pristine $\beta 2(2\times4)$ phase alongside three characteristic oxygenated phases: $\beta 2(2\times4)(P_2O_7)$, $(2\times2)(P_2O_6)_2$, and $(2\times2)(P_2O_7)_2$ (Fig. 12b). To overcome the fundamental electronic limitations of semi-local DFT, appropriate scissors operator parameters (Δ_{scissor}, v_{slope}, and c_{slope}) are obtained for both the solid–liquid and solid–vacuum interfaces. This parameter fitting is performed by mapping the PBE-derived band structures onto a reference PBE0-derived band structure calculated from a representative mid-trajectory surface snapshot (Table 1). A positive or negative value for the correction accounts for the relative change in the PBE band gap compared to the PBE0 exchange-correlation functional; specifically, a positive shift compensates for the characteristic underestimation of the gap, while a negative adjustment compen-

Surface	Δ_{scissor} (eV)	c_{slope}	v_{slope}
$\beta 2(2\times4)$ without H_2O	0.403	1.098	1.138
$\beta 2(2\times4)$ with H_2O	0.35	1.117	1.164
$\beta 2(2\times4)(P_2O_7)_3$ without H_2O	0.246	1.085	1.178
$\beta 2(2\times4)(P_2O_7)_3$ with H_2O	0.7097	1.1	1.198
$(2\times2)(P_2O_6)_2$ without H_2O	0.487	1.086	1.147
$(2\times2)(P_2O_6)_2$ with H_2O	-0.143	1.207	1.206
$(2\times2)(P_2O_7)_2$ without H_2O	0.775	1.037	1.183
$(2\times2)(P_2O_7)_2$ with H_2O	-0.469	1.08	1.207

Table 1: Scissors-operator parameters obtained for different surface, used to determine the RA-spectrum. Δ_{scissor}, c_{slope}, and v_{slope} correspond to the shift in band gap and scaling of conduction and valence bands, respectively. The respective values are taken from paper ref. *A2*.

sates for any localized overestimation. From there, the resulting time-resolved RAS–representing the optical response for configurations belonging to the equilibrated region of the AIMD trajectories–is calculated to correlate the interface dynamics with the resulting anisotropy. To evaluate the spectral variations between individual snapshots, the RAS of each snapshot is compared against a geometry-optimized mid-trajectory reference state, yielding the reference and time-averaged RA-spectra, respectively. The RA-spectra of different snapshots are then combined to generate color plots for the respective interfaces, visually displaying the spectral evolution over time. This analysis aims to uncover how dynamic surface fluctuations and specific structural motifs fundamentally influence the optical anisotropy.

For the pristine $\beta 2(2\times4)$ surface, H_2O adsorption and subsequent kinetic dissociation occur, resulting in the adsorption of surface hydroxyl (OH) groups. An interesting phenomenon is observed for the $(2\times2)(P_2O_6)_2$ phase in contact with H_2O: the P_2O_6 moieties adsorb a hydrogen atom, while an additional oxygen atom is inserted into the underlying In-layer, leading to significant in-plane distortion. This insertion drastically impacts the optical anisotropy of the sample, prompting the appearance of a large negative feature that clearly distinguishes it from the water-free case. Conversely, the overlying H_2O layer acts to stabilize the surface (Sec. 5.2.3).

Notably, the fully passivated P-rich (2×2) surface exhibits the opposite trend compared to its partially passivated counterpart. The strong negative anisotropy present for the solid–liquid interface of the $(P_2O_6)_2$ phase is also observed for the solid–vacuum

interface of the $(P_2O_7)_2$ phase (Sec. 5.2.4). This correspondence highlights how theoretical insights can be effectively leveraged to isolate and identify changes in optical anisotropy across distinct chemical interfaces.

5.2.1 $\beta 2(2\times4)$

First, AIMD simulations are used to study the structural dynamics and thermal stability of the $\beta 2(2\times4)$ reconstruction–a stepped surface with 3 P–P dimers on an In-termination–in vacuum and in contact with H_2O molecules at 300 K using an NVT ensemble (see Sec. 4.3). The simulations are conducted for $\sim$ 21 ps and 15 ps for the solid -vacuum and solid–liquid interfaces, respectively, to ensure sufficient equilibration for both systems.

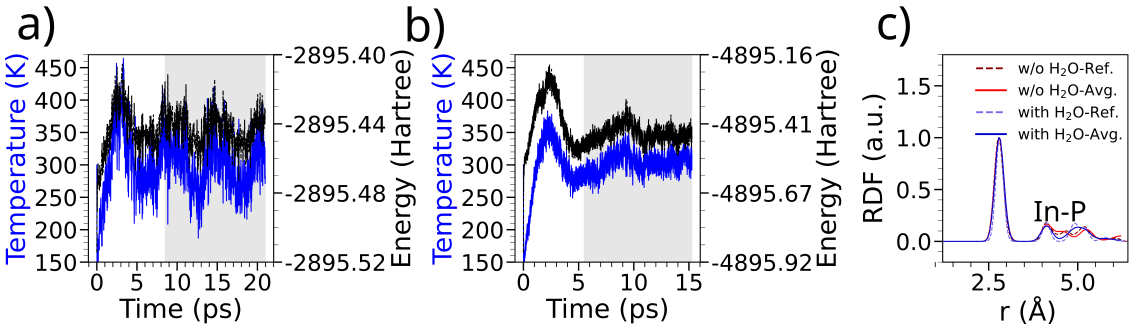

Figure 13: AIMD trajectories of the $\beta 2(2\times4)$ reconstruction: (a) temperature (blue) and energy (black) variation wrt. time for the solid–vacuum interface; (b) depicts variations for the clean interface in contact with H_2O. The grey shaded area in both (a) and (b) depicts the equilibrated region, (c) shows the RDF of the In–P pairs in the topmost layers, calculated for the equilibrated (grey) region with (blue lines) and without H_2O (red lines). Sub-figure (c) is adapted from the paper *A2*.

Fig. 13 shows the time-evolution of temperature (blue) and total energy (black). In the solid–vacuum case (Fig. 13a), a rapid jump in temperature is observed during the initial equilibration phase, reaching $\sim$ 450 K before stabilising around $\sim$ 300 K alongside some noticeable fluctuations. The total energy fluctuates around a mean value of -2895.47 Ha. Similarly, for the solid–liquid interface (Fig. 13b), reduced fluctuations around a mean value of -4895.45 Ha are observed. The grey-shaded areas (Fig. 13a, b) correspond to the equilibrated regions where the time-resolved spectroscopy is calculated.

To investigate the structural origins of the optical response, radial distribution function (RDFs) are are calculated for the In and P atoms in the topmost layers of the structure. The solid lines denote the average RDF obtained along the equilibrated region of the AIMD trajectory, whereas the dashed lines correspond to the reference structure, which has been convoluted with a Gaussian function to allow for better direct comparability. The data are scaled with respect to the respective maxima. For the solid–vacuum in-

terface, snapshot visualisations reveal that the atomic distance between the phosphorus atoms of the three P–P dimers barely change throughout the trajectory ($\Delta r(t)^{P-P} \sim 0$). The slight variations in the In–P RDF, characterised by a shoulder peak at ~ 4 Å, are primarily attributed to the thermal displacement of In atoms in the underlying In-layer (Fig. 13c).

Interestingly, the solid–liquid interface exhibits significant structural changes. H_2O undergoes both molecular and dissociative adsorption (Fig. 14), as observed during relaxation (pre-AIMD) and within the equilibrated region (grey (Fig. 13b). The surface is highly dynamic, frequently changing between configurations with two or three hydroxyl groups. This temporal variation, combined with the potential formation of H_3O^+ ion the bulk water layer, leads to variations in the P–P dimer bond lengths in in comparison to the solid–vacuum counterpart. In contrast, for the solid–liquid interface, the RDF peak for the third nearest neighbour (at ~ 5 Å, situated below the two P-dimers on the upper plateau) exhibits a broader distribution. The indium atoms for this peak corresponds to the In-layer below the P-dimer on the lower terrace.

Furthermore, adsorbed OH groups on the In terrace continuously switch positions via interaction with nearby H_2O molecule (Fig. 14), a mechanism reminiscent of Grotthus- and Zundel-type behaviour [38]. To investigate the structural dynamics, a total of 20 equidistant configurations–referred to as trajectory snapshots–sampled at intervals of 500 fs are extracted. To get an overview of the relative differences induced by these fluctuations, the calculated RA-spectra of the individual snapshots are analysed alongside the mid-trajectory reference state and the overall time-averaged spectrum.

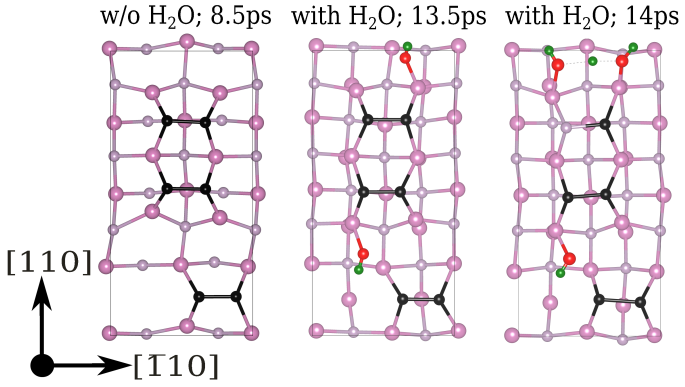

Figure 14: Top view of $\beta 2(2\times4)$ surface, used for RA-spectra calculations in the presence and absence of H_2O. Surface dimers, i.e. P–dimers are indicated in dark-grey. In, P, O, and H are indicated by pink, grey, red, and green spheres.

Second, as discussed in Sec. 4.3, scissors operator parameters are obtained for mid-trajectory surfaces by fitting the semi-local PBE-derived bands to hybrid PBE0 reference band structures for both cases with and without H_2O (Table 1). For the solid–vacuum interface, the time-averaged RA-spectra (Fig. 15c) displays major peaks centered at $\sim$ 3.1 eV, 3.9 eV, alongside a complex multiple peak feature spanning the range 4.1–5.5 eV ultraviolet range. Additionally, a minor low-energy spectral feature emerges at $\sim$ 1.9 eV within specific individual snapshots. The prominent feature at $\sim$ 3.9 eV, consistently identified snapshots (Fig. 16), dominates the colour plot over the entire 20 ps trajectory (Fig. 15a), likely due to the high structural rigidity of the surface P–P dimers.

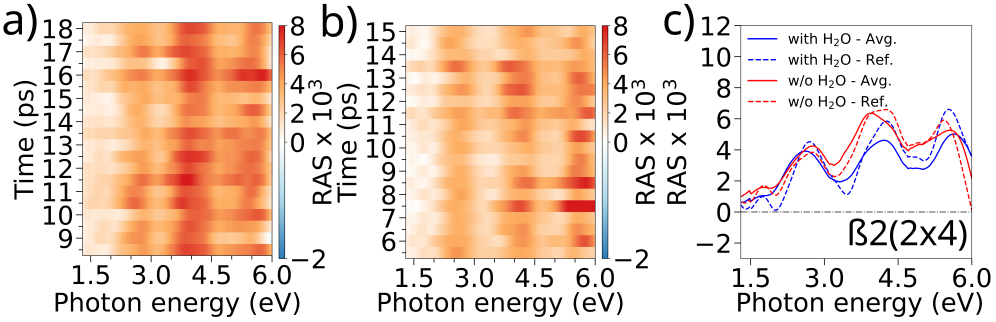

Figure 15: Evolution of RAS during the MD trajectory of the $\beta 2(2\times4)$ surface. (a) and (b) show the time-resolved RAS colour plots for the $\beta 2(2\times4)$ surface without and with H_2O, respectively. (c) presents the time-averaged and reference RA-spectra for both the with H_2O (blue lines) and without H_2O (red lines) cases. This figure is adapted from paper *A2*.

The feature at $\sim$ 3.1 eV is prone to more pronounced changes, exhibiting peak splitting and intensity reduction in specific snapshots (e.g. at 8.5 ps relative to 15 ps and 16.5 ps in Fig. 16). Similarly, the high intensity feature at 5.5ėV shows variations and splitting at specific timesteps (e.g., 16.5 ps). Regarding solid–liquid interface, the RA-spectra undergo small deviations over time characterised by systemic peak broadening and intensity reduction (Fig. 15b). Prominent peaks centered at $\sim$ 2.7 eV, 3.3 eV, 3.8 eV are resolved in the time-averaged RA-spectra. Interestingly, the minor low-energy spectral feature observed at $\sim$ 1.8 eV completely diminishes for the 14 ps snapshot (Fig. 17). It is worth noting that while the profiles obtained for different snapshots along the trajectory remain in good qualitative agreement with the overall time-averaged spectra, clear deviations from the reference structure are observed. Upon comparing the individual spectra, the peaks present at $\sim$ 3.3 eV and 3.8 eV fluctuate prominently along the trajectory, as

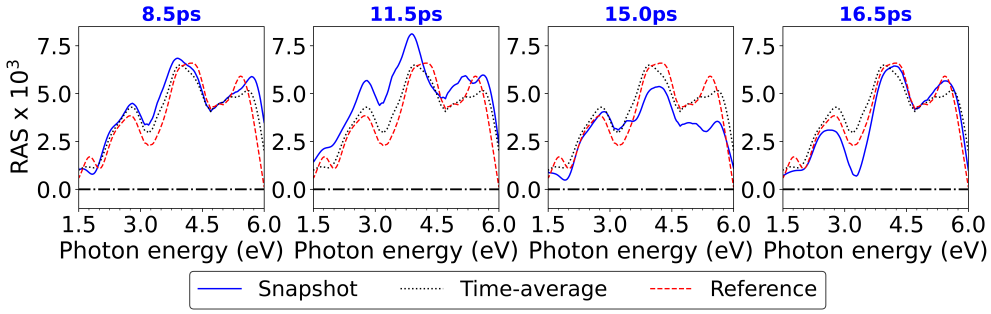

Figure 16: RA-spectra of the $\beta 2(2\times4)$ surface without H_2O along the AIMD trajectory. The blue line represents the RA-spectra at an individual time-step, while the time-averaged, and the reference structure RA-spectra are depicted as black and red dashed lines, resp. This figure is adapted from paper *A2*.

confirmed by the intensity fluctuations in the colour plots (Fig. 15b). Concurrently, the peak intensity for the spectral feature at ~ 2.7 eV is prone to broadening (e.g. @ 12 ps and 14 ps in Fig. 17), and a notable red-shift of the peak position is also observed for several snapshots (13.5 ps and 14.5 ps).

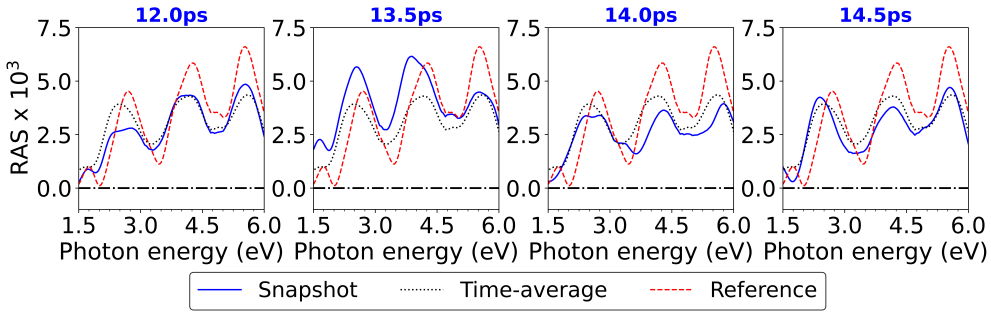

Figure 17: RA-spectra of the $\beta 2(2\times4)$ surface with H_2O along the AIMD trajectory. The blue line represents the RA-spectra at an individual time-step, while the time-averaged, and the reference structure RA-spectra are depicted as black and red dashed lines, resp. This figure is adapted from paper *A2*.

In summary, the RA-spectra for the case without H_2O changes only slightly over time (Fig. 15a). This is directly related to the highly constrained changes in the atomic positions of the P–P dimers and the upper indium layer; however, peak–splitting and deviations from the reference structure are observed in only a few isolated snapshots. In contrast, for the solid–liquid interface, cumulative atomic displacements of surface atoms reaching up to 5 Å toward the bulk are observed over the 20 ps AIMD trajectory.

As is evident from the broadening and shifts in the structural RDF, dynamic interfacial changes driven by the adsorption, desorption, and exchange of hydroxyl groups or coordinating H_2O molecules strongly perturb the electronic eigenvalues along the sampled *k*-path. These dynamic physio-chemical changes modulate the accessible optical transitions at specific photon energies, manifesting macroscopically as the broadening and splitting observed in the time-resolved RA-spectra (Fig. 15b). While, a full snapshot-by-snapshot evaluation via unique PBE-to-PBE0 hybrid band fittings would theoretically capture these variations with high precision, such a procedure remains computationally prohibitive.

5.2.2 $\beta 2(2\times4)(\mathbf{P_2O_7})_3$

Following the same approach as used for the clean surface, we performed time-resolved anisotropy analysis on configurations from AIMD simulations of the fully passivated $\beta 2(2\times4)(P_2O_7)_3$ surface. This analysis provides insight into the interplay between surface dynamics and the resulting optical response. The vacuum dimensions and the total number of H_2O molecules remain identical to the previous case.

AIMD simulations are conducted for $\sim$ 15 ps and 18 ps for the solid -vacuum and solid–liquid interfaces, respectively. While full passivation successfully reduced the equilibration time for the solid–vacuum interface, it conversely increased the time required for the solid–liquid interface. This suggests that while passivation enforces structural rigidity–leading to faster stabilisation in vacuum–it introduces interfacial dynamics or re-ordering at the interfacial boundary that invokes a longer equilibration period compared to the clean $\beta 2(2\times4)$ surface. In the solid–vacuum case, an initial temperature increase is followed by stabilisation of both temperature at around 300 K (Fig. 18a), with the total energy in the equilibrated region fluctuating around a mean value of -3232.96 Ha (Fig. 18a). For the solid–liquid interface, the temperature stabilises around 300 K after an initial peak of $\sim$ 450 K at 2 ps during equilibration, with energy fluctuating around -5233.00 Ha (Fig. 18b).

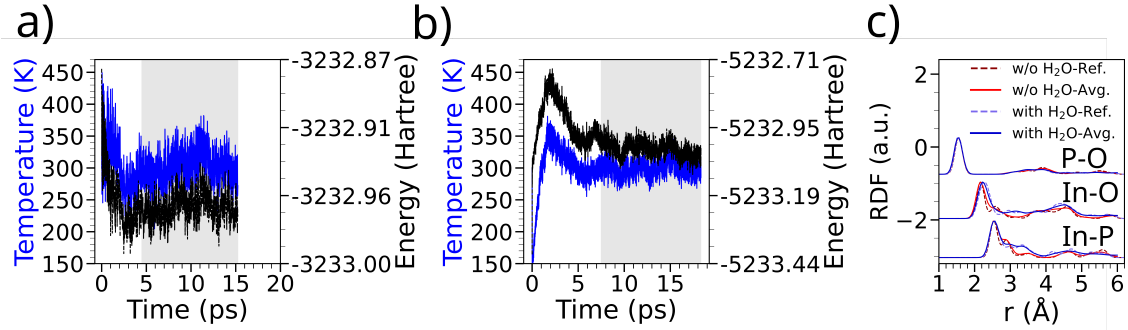

Figure 18: AIMD trajectories of the $\beta 2(2\times4)(P_2O_7)_3$ reconstruction: (a) temperature (blue) and energy (black) variation wrt. time for the solid–vacuum interface; (b) depicts variations for the clean interface in contact with H_2O. The grey shaded area in both (a) and (b) depicts the equilibrated region, (c) shows the RDF of the In–P, In–O, and P–O pairs in the topmost layers, calculated for the equilibrated (grey) region with (blue lines) and without H_2O (red lines). Sub-figure (c) is adapted from the paper *A2*.

To investigate the structural origins of the optical response, we examine the pair-wise

distributions in Fig. 18c. For the solid–vacuum interface, the P–O–P bridge within the three P-dimers is stable, with P–P distances ranging from 2.8 to 3.2 Å. However, the story differs for the In–O–P bridge back-bonds, particularly for the P_2O_7 unit on the lower terrace. This discrepancy results in a sharp shoulder in the In–P RDF: while the two P-dimers on the upper terrace maintain an In–P bond distance of $\sim$ 2.8 Å (the sharp RDF peak), the In–P distance for the lower terrace unit shifts from 3.4 to 3.7 Å.

A distinct behaviour emerges for the solid–liquid interface in comparison to the clean surface (Sec. 5.2.1). Here, H_2O molecules dissociate, allowing hydroxyl groups to bind directly to the underlying In-layer, forming In–OH–In or In–OH species (Fig. 20). Throughout the trajectory, we observe the coordination of two water molecules on an indium atom.

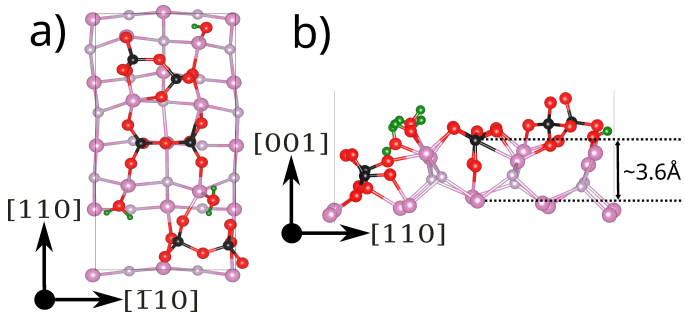

Figure 19: Top view and side view of $\beta 2(2\times4)(P_2O_7)_3$ 7.5 ps snapshot, used for RA-spectra in contact with H_2O. Surface dimers, i.e. P–dimers are indicated in dark-grey. In, P, O, and H are indicated by pink, grey, red, and green spheres.

An interesting structural event is captured in the 7.5 ps snapshot: the oxygen atom of a P–O bond bends toward the bulk to form an In–O–P bond involving the middle P-dimer and the second indium layer. This "*short lived*" geometry plays a role in the broadening of the peak corresponding to the second nearest neighbour in the In–P pair wise distribution (Fig. 19 and 18c). While the P–P distance within the P–O–P bridge remains $\sim$ 2.9 Å (similar to vacuum), the left phosphorus atom of the upper plateau dimer undergoes an upward shift along the [110] direction (Fig. 20). Combined with stronger fluctuations in the lower

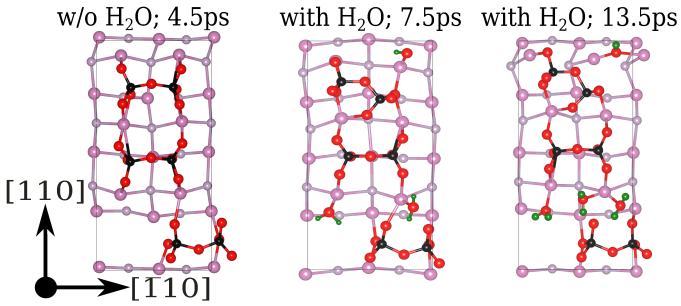

Figure 20: Top view of $\beta 2(2\times4)(P_2O_7)_3$ surface, used for RA-spectra calculations in the presence and absence of H_2O. Surface dimers, i.e. P–dimers are indicated in dark-grey. In, P, O, and H are indicated by pink, grey, red, and green spheres.

terrace In–P distance reaching up to 3.6 Å, these temporal changes result in a much broader second nearest neighbour peak within the In–P RDF distribution compared to the solid–vacuum interface. Second, as discussed in Sec. 4.3, scissors operator parameters for both cases are obtained by fitting PBE-derived to PBE0-derived band structures, using mid-trajectory configurations (Table 1).

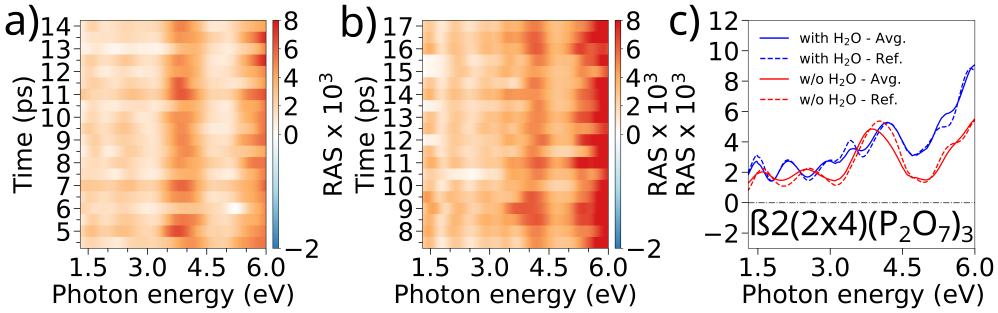

Figure 21: Evolution of RAS during the MD trajectory of the $\beta 2(2\times4)(P_2O_7)_3$ surface. (a) and (b) show the time-resolved RAS colour plots for the $\beta 2(2\times4)(P_2O_7)_3$ surface without and with H_2O, respectively. (c) presents the time-averaged and reference RA-spectra for both the with H_2O (blue lines) and without H_2O (red lines) cases. This figure is adapted from paper *A2*.

The optical analysis of the solid–vacuum interface reveals prominent features at 4.1 and 5.0 eV, alongside several peaks in the 1.6 to 3.0 eV range within the time-averaged RA-spectra (Fig. 22). Peaks in the range of 1.6 to 3.0ėV exhibit a uniform fluctuation in intensity relative to the time-averaged RAS (e.g., at 4.5 ps relative to 5.0 ps and 13.0 ps). The peak at 4.5 eV shows a minor change in intensity over time and the appearance of shoulders in the 5 ps and 6 ps snapshot.

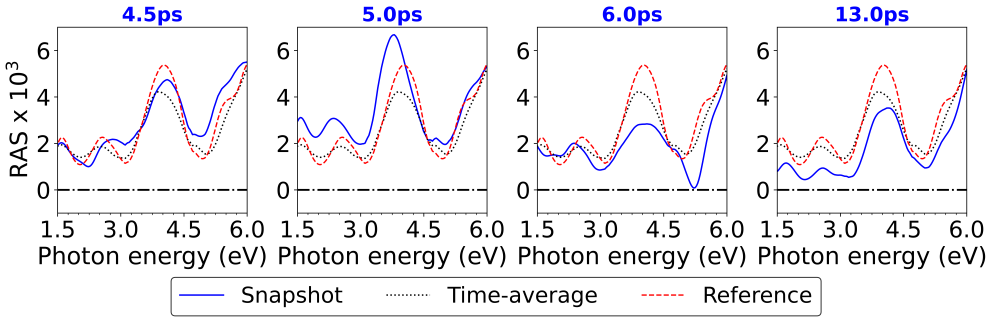

Figure 22: RA-spectra of the $\beta 2(2\times4)(P_2O_7)_3$ surface without H_2O along the AIMD trajectory. The blue line represents the RA-spectra at an individual time-step, while the time-averaged, and the reference structure RA-spectra are depicted as black and red dashed lines, resp. This figure is adapted from paper *A2*.

For the solid–liquid interface, the optical response is qualitatively similar to the vacuum phase, characterised by peaks in the 1.6 to 3.0 eV range, a prominent feature at $\sim$ 4.4 eV, and appearance of shoulders in the high intensity region (Fig. 23). Peak splitting is observed for the $\sim$ 4.4 eV feature in specific snapshots (e.g., at 7.5 ps relative to 10.5 and 13.5 ps). Notable change occur for the high-intensity peak at $\sim$ 5.0 eV during 7.5 to 13.5 ps interval. This feature showcases probable instability, characterised by fluctuating emergence and gradual reduction in intensity that eventually leads to its disappearance (Fig. 23). In summary, the distinct temporal resolved in the time-dependent

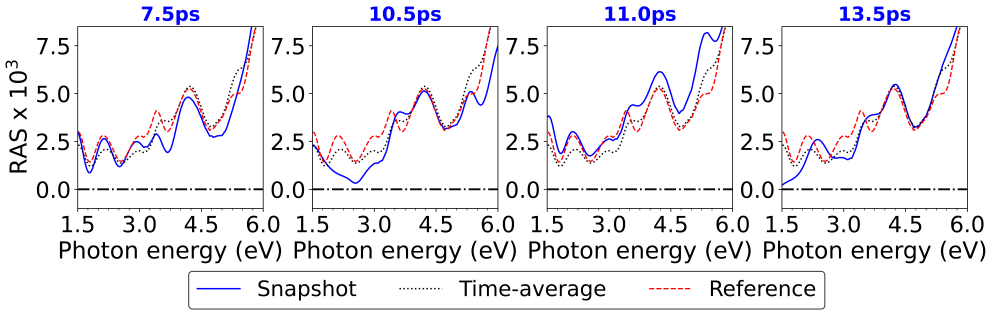

Figure 23: RA-spectra of the $\beta 2(2\times4)(P_2O_7)_3$ surface with H_2O along the AIMD trajectory. The blue line represents the RA-spectra at an individual time-step, while the time-averaged, and the reference structure RA-spectra are depicted as black and red dashed lines, resp. This figure is adapted from paper *A2*.

RA-spectra of the passivated $\beta 2(2\times4)(P_2O_7)_3$ surface serve as a direct optical fingerprint of the differing interfacial environments. For the solid–liquid interface, the spectra fluctuations observed along the AIMD trajectory map onto specific sub-picosecond

domains characterised by active structure re-ordering, namely the dissociation of H_2O into bridging In–OH–In species and structural oxygen insertion toward the bulk. These changes structurally manifest as a broadened In–P pairwise distribution. On an electronic scale, rather than destabilising the system, these modifications modulate the underlying bulk-like and near-surface eigenstates of the constituent atoms that compose the system's band structure. Because these atomic eigenstates are not subject to severe electronic changes, the presence of water layer effectively acts as a stabilising agent that bounds the overall optical variations. This stabilising behaviour is clearly visible in the time–resolved RAS colour plots and snapshot subplots, where the spectra track each other closely over time the minor temporal variations observed between individual snapshots do not indicate severe electronic structural degradation, but rather confirm that the subtle spectral shifts originate from minute, physio–chemical changes at the interface. Consequently, these structural changes simply introduce a localised inhomogeneity that smoothly shifts the accessible polarisation-dependent transition matrix elements. Similarly, the solid–vacuum interface also exhibits remarkable spectral rigidity over time; because the polyphosphates limits large thermal displacements of atoms, keeping their respective eigenstates intact and maintaining a stable temporal evolution of RAS.

5.2.3 $(2 \times 2)(\mathbf{P_2O_6})_2$

Next, we discuss the oxygenated P-rich (2×2) stable phases, identified via the overall phase diagram (Fig. 12). To evaluate the structural dynamics and thermal stability of the $(2\times2)(P_2O_6)_2$ configuration, we performed AIMD simulations for the solid–vacuum and solid–liquid interfaces for 25 ps and 20 ps respectively (Fig. 24a,b).

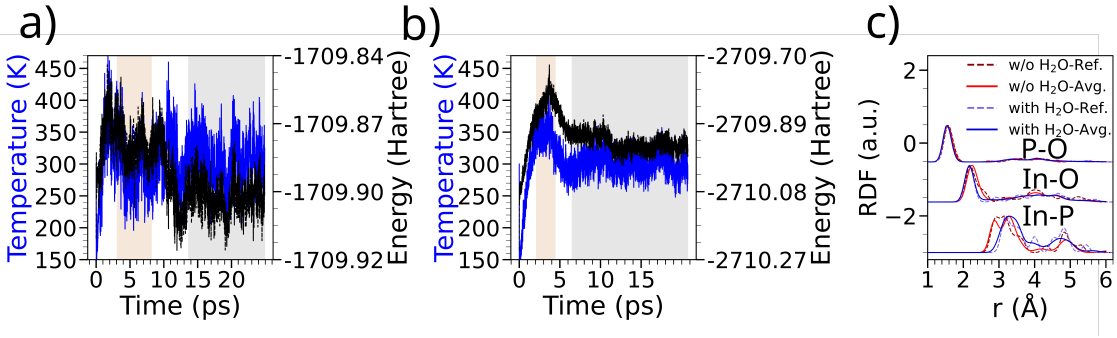

Figure 24: AIMD trajectories of the $(2\times2)(P_2O_6)_2$ reconstruction: (a) temperature (blue) and energy (black) variation wrt. time for the solid–vacuum interface; (b) depicts variations for the clean interface in contact with H_2O. The grey and brown shaded area in both (a) and (b) depicts the stable and meta-stable regions resp., (c) shows the RDF of the In–P, In–O, and P–O pairs in the topmost layers, calculated for the equilibrated (grey) region with (blue lines) and without H_2O (red lines). Sub-figure (c) is adapted from the paper *A2*.

The structure obtained via the overall phase stability analysis represents a partially passivated surface containing 12 oxygen atoms, structured as two P_2O_6 moieties on an underlying In-layer. For consistency, the vacuum size (20 Å) matches that used for the $\beta2(2\times4)$ reconstructions (Sec. 5.2.1 and 5.2.2), interfaces are modelled using an NVT ensemble at 300 K (Sec. 4.3), incorporating 58 H_2O molecules for the solid–liquid interface. AIMD simulations are conducted for ∼ 25 ps and 20 ps for the solid -vacuum and solid–liquid interfaces respectively (Fig. 24a,b). Interestingly, and in contrast to the more rigid (2×4) reconstructions, the P-rich (2×2) system explores multiple stable configurations in phase space, driven by uncompensated dangling bonds arising from the incomplete surface passivation. In these distinct structural regions, the temperature and total energy are not static but fluctuate around stable mean values.

As shown in the brown shaded area of Fig. 24a, the solid–vacuum surface initially resides in a localised meta-stable state for a short time domain (∼ 305 K and -1709.87 Ha) before jumping to a more energetically favourable minimum (grey shaded area). This

second phase remains predominantly stable throughout the remainder of the simulation ($\sim$ 300 K and -1709.9 Ha). Similarly for the solid–liquid interface, a clear transition from an initial equilibrated state ($\sim$ 345 K and -2709.87 Ha) toward a more stable thermodynamic equilibrium is observed, as indicated by the grey shaded area ($\sim$ 300 K and -2710.2 Ha). This latter equilibrated region, where the temperature and energy fluctuate around a global minimum, is used for the subsequent optical analysis. Significant changes in atomic ordering, driven by the dynamic interaction with the H_2O molecules, are observed here, which strongly impact the RA-spectra of specific trajectory snapshots.

The correlation of these observed changes in the optical response with underlying surface dynamics is highlighted by the pairwise distribution in Fig. 24c. In the solid–vacuum case, the covalent P–O–P bridge within the P_2O_6 unit is highly rigid, with bond distances ranging narrowly from 2.9 to 3.1 Å, translating to a sharp, well defined P–O peak in the RDF. However, the notable split observed in the In–P distribution split is directly related to the underlying In–layer dynamics: while the geometry optimised (overall phase stability Sec. 5.1.3) identifies four sets of linear In–O–In bonds, but the subsequent breaking of specific In–O bonds during the AIMD trajectory creates two distinct stable In–P bond lengths clustered around $\sim$ 3 Å.

In the solid–liquid interface, the dynamic interaction with H_2O over-layer significantly re-orders the structural framework via several distinct pathways:

1. Water dissociation and P_2O_7H formation: Water molecules undergo dissociation, where the resulting hydroxyl groups adsorb onto surface P atoms over the course of simulation. Concurrently, hydrogen adsorption or subsequent proton transfer directly from these adsorbed sites facilitates active hydrogen migration across the surface, converting the localised P_2O_6 units into protonated or hydroxylated, P_2O_6H and P_2O_7H-like groups and shifting the surface a 13-oxygen composition (Fig. 25).

2. Oxygen insertion and In_3O formation: Additional oxygen atom inserts toward the bulk. The initial structural connectivity of four $P-O\begin{smallmatrix}\diagup\,In\\ \diagdown\,In\end{smallmatrix}$ units is disrupted by hydrogen migration and resulting hydroxyl formation from the bulk water layer along-with oxygen insertion. This chemical rearrangement leads to the formation of persistent, highly coordinated In_3O cluster within the indium layer.

3. Separate In–O–P bond formation: On a left P-atom of top P–P dimer site, creation of new In–O–P bond happens for the 14 ps snapshot in the solid–liquid interface (Fig. 25).

4. Surface shifting and RDF broadening: These cumulative bonding changes force the phosphorus atom of the topmost surface dimer to shift outward along the [001] direction toward the vacuum. (Fig. 25). Although the P–O and In–O distributions remain relatively narrow, the to solid–vacuum interface (Fig. 24c). This reflects that the $r_{(\text{In-P})}(t)$ distance distributions for both the immediate surface and the near-surface atoms span a wide spatial range, confirming significantly larger positional fluctuations of the surface atoms than seen in the vacuum case.

5. Surface shifting and RDF broadening: These cumulative bonding transformations force the phosphorus atom of the topmost surface dimer to shift outward along the [001] direction toward the vacuum (Fig. 25). Although the core P–O and In–O distributions remain relatively narrow, these complex rearrangements invoke a severe broadening of the structural In–P peak compared to the vacuum baseline (Fig. 24c), showing that the $r_{\text{In-P}}(t)$ bond metrics track across a broad spatial range with enhanced positional fluctuations.

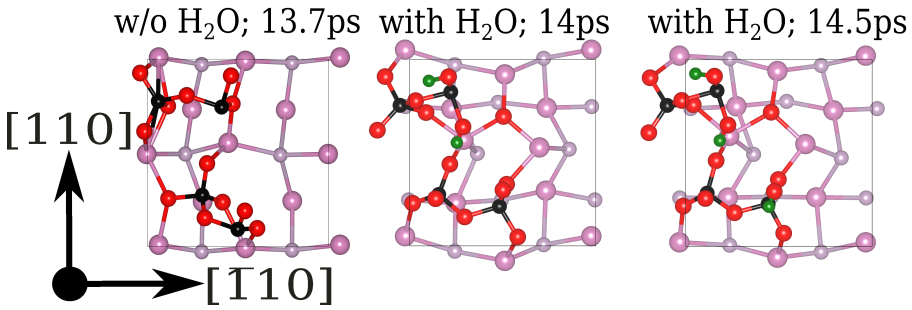

Figure 25: Top view of $(2 \times 2)(P_2O_6)_2$ surface, used for RA-spectra calculations in the presence and absence of H_2O. Surface dimers, i.e. P–dimers are indicated in dark-grey. In, P, O, and H are indicated by pink, grey, red, and green spheres.

The scissors operator parameters are determined using the exact same approach established the $\beta 2(2 \times 4)$ surfaces (Table 1). For the solid–vacuum interface, the time-averaged RA-spectra correlate strongly with the reference structure (Fig. 26c). Nonetheless, evaluating the the optical response of individual snapshots highlights some interesting changes, particularly within the mid-energy range ($\sim$ 2.8 to 4.0 eV) and near the

high-energy region at 5.1 eV. The provisional peak at ∼5.1 eV–which stands out as a sharp feature in the reference spectrum–is notably diminished in the time-averaged result.This attenuation is a direct consequence of the frequent structural configurations explored during the simulation. Furthermore, the snapshots taken at different time intervals reveal significant dynamic behaviour (Fig. 27). Between 20.7 ps and 22.7 ps, a merging of peaks and a subsequent down-shift in intensity occur within the 2.0 to 3.7 eV range. Concurrently, from 13.7 ps to 22.7 ps, the peak at ∼ 5.1 eV undergoes continuous broadening accompanied by intensity fluctuations.

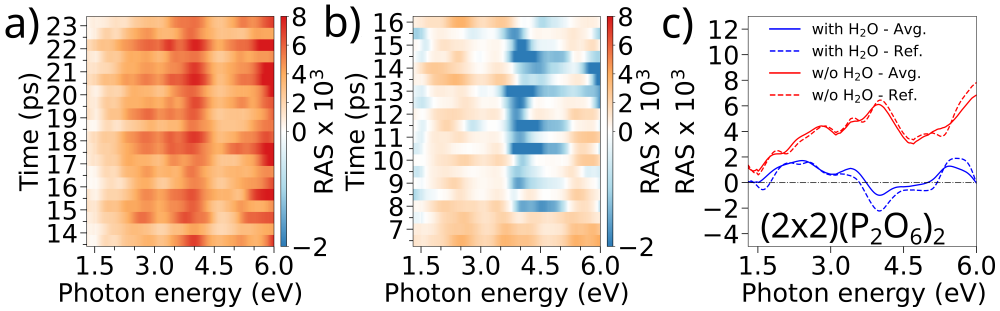

Figure 26: Evolution of RAS during the MD trajectory of the $(2\times2)(P_2O_6)_2$ surface. (a) and (b) show the time-resolved RAS colour plots for the $(2\times2)(P_2O_6)_2$ surface without and with H_2O, respectively. (c) presents the time-averaged and reference RA-spectra for both the with H_2O (blue lines) and without H_2O (red lines) cases. This figure is adapted from paper *A2*.

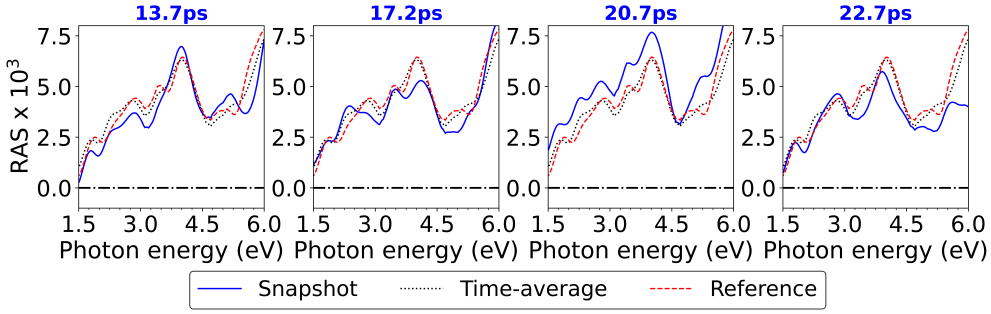

Figure 27: RA-spectra of the $(2\times2)(P_2O_6)_2$ surface without H_2O along the AIMD trajectory. The blue line represents the RA-spectra at an individual time-step, while the time-averaged, and the reference structure RA-spectra are depicted as black and red dashed lines, resp. This figure is adapted from paper *A2*.

An analysis of the optical response for the solid–liquid interface reveals highly pronounced temporal changes that are vastly more sever than those seen in the $\beta2(2\times4)$

phases. Throughout the trajectory, significant changes–such as occasional full inversions between positive and negative intensities–are clearly resolved (Fig. 28 and 26b). Focusing on the transition of the optical response at $\sim 4.0\,\text{eV}$ from 13.5 ps onwards, we observe a gradual collapse in positive anisotropy accompanied by a noticeable blue–shift and wide-spread peak broadening (Fig. 28). Specifically, the RA-spectra for the 14.5 ps snapshot showcase a profound reduction in peak intensity at $\sim 4.0\,\text{eV}$. Conversely, at higher photon energies ($\sim 5.0\,\text{eV}$), the optical response for individual snapshots appears to converge for simulation times exceeding 15 ps (Fig. 26b).

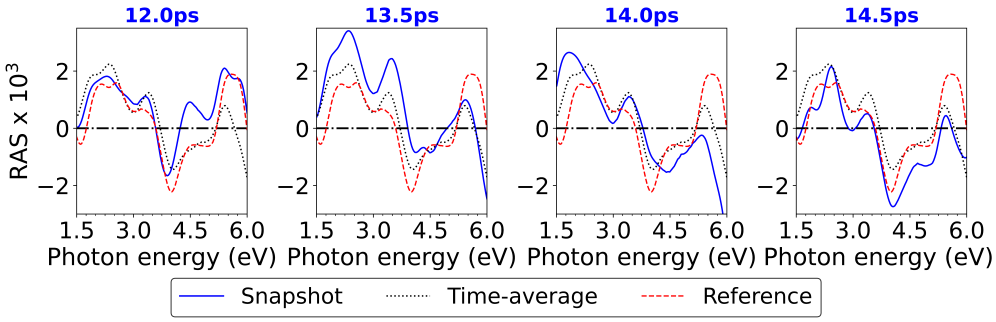

Figure 28: RA-spectra of the $(2 \times 2)(P_2O_6)_2$ surface with H_2O along the AIMD trajectory. The blue line represents the RA-spectra at an individual time-step, while the time-averaged, and the reference structure RA-spectra are depicted as black and red dashed lines, resp. This figure is adapted from paper *A2*.

In summary, $(2\times2)(P_2O_6)_2$ surface shows significant optical variations driven by its highly dynamic structural behaviour.While the vacuum interface remains mostly consistent with the reference RA-spectra–with only subtle temporal changes visible in the colour plot–the liquid interface undergoes substantial chemical and resulting electronic changes that strongly correlate with the macroscopic optical response. The striking emergence of negative anisotropy and extensive peak broadening can be linked to a structural change of the P_xO_y motif and the formations of In–O–P bond along-with the formation of In_3O unit.

We can hypothesise that these changes arise from several physical factors. The presence of dangling bonds on a partially passivated surface invokes a significant amount of atomic rearrangement, specifically for the solid–liquid interface. This directly modifies the surface electronic environment, enabling more plausible electronic transitions over the course of AIMD simulation. Ultimately, these intertwined structural and electronic changes do result in some unique features for certain snapshots, such as peak

inversions observed at 4.0 eV. These features are driven by highly localised changes in the coordination environment around individual atomic sites, which heavily configure the polarisation-dependent transition matrix elements over time. However, capturing the full scope of these coupled fluctuations introduces inherent computational trade-offs. A small surface size can artificially give rise to an unwanted or discrete vibrational density of states due to periodic image interactions. Consequently, a substantial simulation time domain alongside a large supercell is required to properly smooth out these finite-size vibrational artifacts and reach an equilibrated phase. Furthermore, an ideal choice of built-in parameters of an NVT thermostat, necessary to maintain a stable temperature profile at 300 K, is required (Sec. 9.1).

5.2.4 $(2 \times 2)(\mathbf{P_2O_7})_2$

Lastly, we investigate the fully passivated P-rich (2×2) surface, representing the next fully oxygenated phase in the overall phase diagram Fig. 12. Following the analysis used for the partially passivated $(P_2O_6)_2$ surface (Sec. 5.2.3), we performed AIMD simulations to calculate the time–resolved RA-spectra for the $(2\times2)(P_2O_7)_2$ surface. This approach enables a systematic investigation of the optical anisotropy over a temporal domain, establishing a direct correlation between the degree of surface passivation and the resulting RAS features.

The trajectories for hte solid–vacuum and soli–liquid interfaces are conducted for ∼ 25 ps and 14 ps respectively (Fig. 29a,b). As illustrated in Fig. 29a, the solid–vacuum interface initially occupies a meta-stable state (brown shaded region) characterised by a higher total energy plateau of ∼ -1741.85 Ha. Between 6 and 8 ps, the system undergoes a structural transition marked by a sharp, temperature spike peaking at ∼ 500 K near 7.5 ps. This thermal behaviour indicates that the system is overcoming a kinetic barrier to escape its meta-stable state and transition toward a more energetically favourable, stable minimum (grey shaded area, ∼ 300 K and -1742.0 Ha).

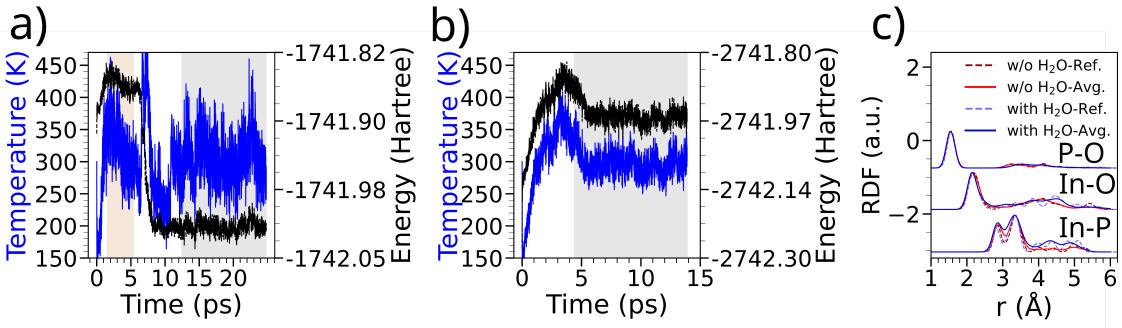

Figure 29: AIMD trajectories of the $(2\times2)(P_2O_7)_2$ reconstruction: (a) temperature (blue) and energy (black) variation wrt. time for the solid–vacuum interface, where the brown shaded area is a transient meta-stable state; (b) depicts variations for the clean interface in contact with H_2O. The grey shaded area in both (a) and (b) depicts the equilibrated region, (c) shows the RDF of the In–P, In–O, and P–O pairs in the topmost layers, calculated for the equilibrated (grey) region with (blue lines) and without H_2O (red lines). Sub-figure (c) is adapted from the paper *A2*.

In stark contrast to the partially passivated $(P_2O_6)_2$ surface the solid–liquid interface for this fully passivated structure exhibits a significantly smoother transition toward equilibrium (Fig. 29b), seamlessly reaching a steady sate without jumping between distinct

energetic plateaus.

In the vacuum phase, the P_2O_7 moieties themselves prove to be quite rigid. The P–P distance within the internal P–O–P bridges remain nearly constant at ~ 2.8 Å, which yields a sharp, well-defined P–O RDF peak in the RDF. However, a major sub-surface rearrangement takes place during the transition to the lower energy plateau:

1. P–P dimerisation: At ~ 4 Å below the polyphosphate motifs, existing In–P back bonds break. This facilitates the clear formation of a localised P–P dimer with a bond length of $\sim$ Å (Fig. 30, w/o H_2O at 20.9 ps).

2. Reduction of In–O–P bridges: The four active bonding linkages initially identified at 0 K during the overall phase stability analysis (Sec. 5.1.3) reduce to just two as the surface reorganises,

3. Interfacial ring formation: A persistent ring-like connectivity involving the coordinating In, P, and O atoms emerges at the interface (Fig. 30 w/o H_2O at 20.9 ps). This spatial rearrangement directly contributes to a splitting of the In–P peak RDF peak observed around 3.0 Å (Fig. 29c).

The interaction with bulk H_2O phase invokes n entirely different set of structural constraints. Here, the P–P distance within the P_xO_y units expands slightly to ~ 3.1 Å. Similarly, the initial four In–O–In surface links are reduced to a single link for the top polyphosphate motif. This localised bridge imposes certain constraints, significantly restricting the motion of the upper In–O–P pairs relative to the lower motif and giving rise to a distinct, well resolved In–P peak splitting in the RDF (Fig. 29c). The comparative RDF analysis reveals that while the P–O and In–O distributions remain relatively consistent across both environments, the active In–P bonds deviate sharply from the bulk crystal behaviour via two key trends:

1. Bond extension: Compared to the ideal bulk In–P distance (r^{bulk}_{In-P}) ~ 2.53 Å, surface relaxation and the broken symmetry extend these bonds to ~ 2.7 Å for clean, unperturbed surface obtained at 0 K.

2. Dynamic displacement split: During the AIMD trajectory of the solid–liquid interface, specific In–P bond distances split widely between 2.6 and 3.0 Å. This confirms that the bulk and surface bond lengths differ substantially ($r^{\text{bulk}}_{\text{In-P}} \neq r^{\text{surf}}_{\text{In-P}}$) due

to dynamic interactions over time, as observed in the snapshots of Fig. 25 (e.g. at 11.4 ps with H_2O).

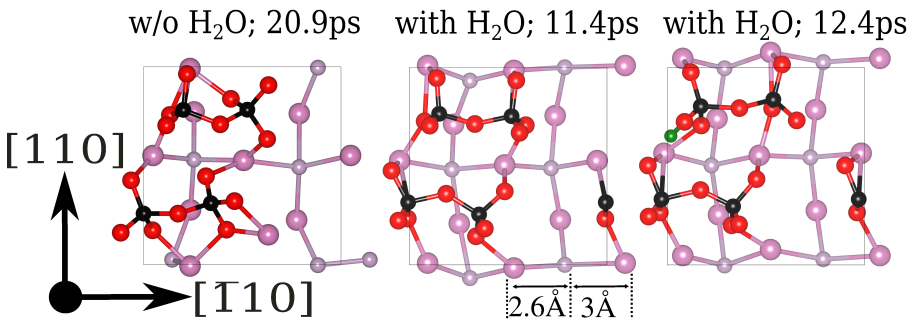

Figure 30: Top view of $(2 \times 2)(P_2O_7)_2$ surface, used for RA-spectra calculations in the presence and absence of H_2O. Surface dimers, i.e. P–dimers are indicated in dark-grey. In, P, O, and H are indicated by pink, grey, red, and green spheres.

Scissors operator parameters for both interfaces are determined using mid-trajectory surface snapshots (Table 1). For the solid–vacuum interface, the time-averaged RA-spectra exhibit a prominent, sharp optical feature located at ~ 5.3 eV (Fig. 32). Within the mid-energy range (3.2–4.8 eV), the spectra undergo significant evolution over the course of the simulation: specifically the peak centered at 4.2 eV undergoes broadening accompanied by a steady reduction in intensity over time (e.g., comparing the 13.4 ps snapshot to the 18.4 ps snapshot).

Notably, the spectral features within the 2.8 to 4.2 eV region remain persistent throughout the trajectory, showing consistent line shapes. However, they exhibit a clear shift in intensity over time, as seen by the deeper negative anisotropy in the 20.9 ps snapshot compared to the early 12.4 ps snapshot (Figs. 31a and 32). This distinct shift toward a more negative anisotropy correlates with the previously discussed structural changes–specifically the subsurface P–P dimerisation and the reduction of the coordinating In–O–In bridges–which breaks local symmetry and alters the surface electronic states. The corresponding colour plot (Fig. 26a) confirms these subsequent intensity changes throughout the trajectory, showing stable but dynamic fluctuations particularly at lower photon energies.

On the other hand, the solid–liquid interface showcases the exact opposite behaviour, demonstrating significantly lower variance in its calculated optical anisotropy over time. The individual, snapshot derived RA-spectrum display a remarkably high coherence with

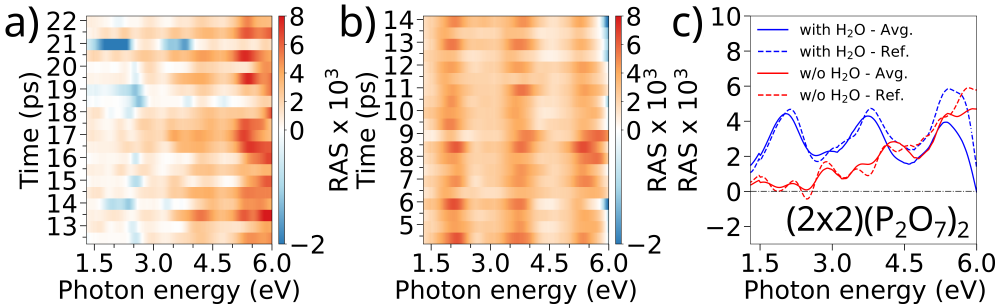

Figure 31: Evolution of RAS during the MD trajectory of the $(2\times2)(P_2O_7)_2$ surface. (a) and (b) show the time-resolved RAS colour plots for the $\beta2(2\times4)$ surface without and with H_2O, respectively. (c) presents the time-averaged and reference RA-spectra for both the with H_2O (blue lines) and without H_2O (red lines) cases. This figure is adapted from paper *A2*.

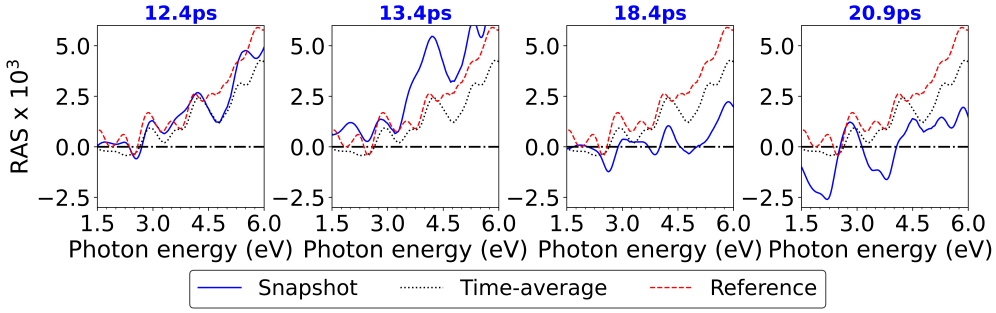

Figure 32: RA-spectra of the $(2\times2)(P_2O_7)_2$ surface without H_2O along the AIMD trajectory. The blue line represents the RA-spectra at an individual time-step, while the time-averaged, and the reference structure RA-spectra are depicted as black and red dashed lines, resp. This figure is adapted from paper *A2*.

both the time-averaged and reference spectra (Fig. 33). This interface is characterised by three distinct, stable peaks of comparable intensities located at 2.1, 3.7, and 5.5 eV. Temporal fluctuations here are minimal, consisting primarily of subtle peak-splitting effects or minor intensity reductions (as seen in the 11.4 ps and 12.4 ps snapshots). This optical consistency reflects the structural insights obtained from our radial distribution analysis: while the dynamic interaction with H_2O overlayer causes minor polyphoshpate bending, localised H_2O adsorption, and shifting In–O–In bridging that constrain atomic motion, the core $P_xO_y$moiety remains intact. Crucially, the system avoids the major subsurface structural rearrangements and bond-breaking events observed under vacuum conditions. A comparative analysis of the (2×2) reconstructions indicates that both the partially passivated $(P_2O_6)_2$ and fully passivated $(P_2O_7)_2$ surfaces undergo transitions

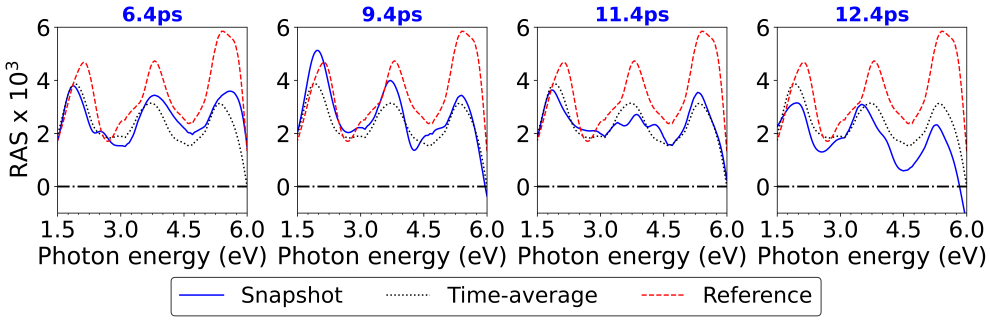

Figure 33: RA-spectra of the $(2 \times 2)(P_2O_7)_2$ surface with H_2O along the AIMD trajectory. The blue line represents the RA-spectra at an individual time-step, while the time-averaged, and the reference structure RA-spectra are depicted as black and red dashed lines, resp. This figure is adapted from paper *A2*.

from meta-stable configurations toward equilibrated minima. However, their structural and optical responses to the surrounding environment follow completely opposite trends. The $(2\times2)(P_2O_6)_2$ surface is chemically reactive. Upon contact with H_2O overlayer, it undergoes a complex, multi-step changes: water dissociates to allow direct hydroxyl adsorption onto active surface P atoms, which triggers proton transfer and hydrogen migration to yield P–OH groups (shifting the surface from a 12-oxygen to 13-oxygen content). This is followed by the insertion of an additional oxygen atom toward the bulk to form structural In_3O complexes, while a separate site forms a new cross-linking In–O–P bond, pushing the final configuration to a 14-oxygen layout. This intense chemical restructuring drives fluctuations in its optical response, ultimately resulting in a persistent negative anisotropy that stands in sharp contrast to the positive anisotropy of its vacuum counterpart.

Conversely, the fully passivated $(2\times2)(P_2O_7)_2$ surface exhibits the inverse behaviour. While its solid–liquid interface remains chemically inert and structurally stabilised by the solvent layer, it is the solid–vacuum interface that experiences a severe temporal evolution. In vacuum, the lack of spatial constraints enables a localised structural degradation of the polyphosphate motif, driving the emergence of a subsurface P–P dimer and a comprehensive reorganisation of the In–O–P connectivity. These major vacuum-phase transformations correlate directly with the appearance of a pronounced negative peak distribution within the 2.0 to 3.5 eV spectral range.

6 Summary and Outlook

The phase stability of InP(001) surfaces was investigated via density functional theory using the PBE exchange-correlation functional, incorporating long-range dispersion interactions through Grimme-D3 corrections. This analysis was a prerequisite to understanding the the behaviour of the semiconductor surface under electrochemical conditions. The surface energy (γ_{surf}) was evaluated to map out the thermodynamic phase stability as a function of the chemical potentials of the surface constituent (γ_{surf} vs. $\Delta\mu_{\text{In}}$). Initially focusing on clean InP(001) reconstructions, our results corroborated well with the previously reported findings of W.G. Schmidt [33]. Along the variation of $\Delta\mu_{\text{In}}$, the mixed-dimer reconstruction was found to be stable under In-rich conditions, consisting of a mixed In–P dimer on an underlying In-layer. The $\beta 2(2\times 4)$ and $\alpha 2(2\times 4)$ stepped surfaces, consisting of 3 and 2 P–dimers on an underlying In-layer,respectively, dominated the intermediate chemical potential region. Interestingly, the previously reported stable (2×2)-1D reconstruction under P-rich conditions was found to be unstable within our framework [33, 83]; this surface is structurally equivalent to (2×2)-2D phase but lacks one P–dimer. This discrepancy in phase stability is attributed to the more refined exchange-correlation treatment and the incorporation of the Grimme-D3 corrections in this work.

Building on these results, the second objective was to analyse oxygen exposure to circumvent the experimental and computational challenges associated with investigating electrochemical interfaces. Obtaining atomistic-scale insight into surface passivation was essential, as the degree of oxygen coverage ($0< \theta <1$) alters both the thermodynamic stability and the electronic properties of the system (via electrochemical and electronic passivation). In this context, surface passivation referred to the formation of P_xO_y polyphosphate motifs via oxygen adsorption. This process was investigated through the sequential adsorption of oxygen atoms across multiple deposition schemes–including sequential adsorption followed by motif transfer, sequential transferring of pre-formed motifs, and the insertion of oxygen atoms into already passivated surfaces. This systematic search identified stable configurations characterised by low enthalpy of formation (ΔH_{f}) for specific coverage, The resulting overall phase diagramm (γ_{surf} vs. $\Delta\mu_{\text{In}}$ and $\Delta\mu_{\text{O}}$) revealed that addatom adsorption of oxygen fundamentally reshapes the landscape of surface stability.

In the P-rich region, P_2O_7, and $(P_2O_7)_2$-passivated $\beta 2(2\times 4)$ surfaces were found to

be stable over a narrow range of $\Delta\mu_{\mathrm{In}}$, whereas an ordered $\beta 2(P_2O_7)_3$ reconstruction exhibited stability over a wider chemical potential window. Under high oxygen-rich conditions, the $(P_2O_6)_2$ and $(P_2O_7)_2$ passivated P-rich (2×2) configurations emerged as thermodynamically stable phases. Specifically, the (2×2)-2D surface passivated with two P_2O_7 units demonstrated stability under O-rich and P-rich domains. Conversely, intermediate 3-O and 4-O atom converges on the same underlying surface fell outside the stability thermodynamic window, corresponding instead to the metallic phosphorus region. Contrary to previous results reported for the widely used mixed-dimer reconstruction, our findings demonstrate that highly passivated, P-rich surfaces dominate over a wide range of indium and oxygen chemical potentials. While the mixed-dimer phase remained stable only with a homogeneous oxygen distribution under highly metallic indium conditions, surfaces obtained from oxygen coverage on the c(4×4) and $\alpha(2\times 4)$ reconstructions failed to occupy any stability domain.

Next, time-resolved spectroscopy was studied for four representative clean or oxygenated phases: the clean $\beta 2(2\times 4)$, the fully passivated $\beta 2(2\times 4)(P_2O_7)_3$, the partially passivated $(2\times2)(P_2O_6)_2$, and the fully passivated $(2\times2)(P_2O_7)_2$ reconstructions. AIMD simulations were employed to capture the finite-temperature (300 K) structural dynamics of these configurations at both solid–vacuum and solid–liquid (specifically, solid–water) interfaces. To compute the optical response, 20 uncorrelated snapshots were extracted from the equilibrated regions over a 10 ps window with a time-step spacing of 500 fs. RA-spectra were calculated within the independent-particle random-phase approximation. To correct for the DFT band-gap limitation, a rigid scissors operator parameters were determined for both interfaces of all phases using mid-trajectory snapshot.

The optical analysis revealed that the solid–vacuum and solid–liquid interfaces of both the clean and fully passivated $\beta(2\times 4)$ systems exhibit highly stable optical signatures over time. Conversely, solid–liquid interface of the $(2\times2)(P_2O_6)_2$ system and the solid–vacuum interface of the $(2\times2)(P_2O_7)_2$ phase exhibited a persistent, pronounced negative anisotropy. While their respective complementary interfaces showed only minor temporal variations. Resolving the intricate details that govern these solid–liquid interfaces remains a challenge in materials science due to the complex, multi-scale coupling of surface dynamics. In this work, AIMD simulations successfully captured real-time interfacial transitions, monitoring how the liquid overlayer triggers site-specific adsorption, molecular dissociation, rapid proton migration, and the temporary formation of Zundel or hydronium ions within the bulk H_2O environment.

Crucially, these geometric rearrangements–manifested as the breaking and forming of local bonding configurations–substantially alter the surface electronic structure. Over the course of the trajectory, these intertwined physical and chemical transformations continuously reconfigure the polarisation dependent transition matrix elements, giving rise to new electronic transitions and modifying the macroscopic dielectric tensor ($\varepsilon_{ij}(\omega)$). That dictates the transient RAS profiles. Ultimately, these findings highlight RAS as an exceptionally sensitive, non-destructive probe for tracking real-time interfacial chemistry, emphasising the absolute necessity of including explicit, realistic electrolyte overlayers in theoretical models to bridge the gap with experimental observations.

Following the analysis of these results, several key aspects can be investigated further, as highlighted below:

1. Oxygen adsorption: The overall phase stability diagram can be systematically extended by incorporating subsurface oxygen atom insertion toward the bulk and substitutive (O $\rightarrow$ P) exchange schemes [87]. Furthermore, this thermodynamic framework should be expanded to identify stable bonding networks of In(P_xO_y) units, as these coordinated complex units emerged as persistent structures during our liquid-phase AIMD trajectories.

2. Computational hydrogen electrode: The current electrochemical boundaries established for H/Cl (co-)adsorption can be extended toward OH/H (co-)adsorption conditions by explicitly evaluating the potential dependent surface free energy surfaces [88].

3. Optimisation of Scissors shift parameters: Tuning the band gap by higher k-point resolution could be one option. To improve accuracy one could also attain specific parameters for each surface (high computational cost), or move beyond IP-RPA formulation. Specifically the independent quasiparticle approximation i.e.the GW approximation to obtain accurate quasiparticle energies, while the BSE framework can be used to account for excitonic effects, accounting for accurate optical response [51]. Furthermore, a scissors shift fitting could be performed between PBE-derived and for e.g. GW or BSE-derived band structure [89].

4. Slab Dimension and Finite-Size Scaling: The slab thickness used in this work was carefully converged with respect to the energy (Sec. 4.3). However, recent studies have shown that the electronic band structure, and hence the optical response, are

very sensitive to the slab thickness [90, 91], such that a very large slab thickness may have to be considered for a direct comparison with experimental data. Concurrently, given the large, dynamic displacements observed in the indium layers of the (2×2) configurations during the AIMD simulations, extending the surface in the *xy*-plane may allow additional dynamic configurations with altered RA-spectra to be captured.

7 List of Abbreviations

AIMD Ab initio molecular dynamics.
BSE Bethe-Salpeter equations,
BoS Balance-of-system.
CHE Computational hydrogen electrode.
DFT Density functional theory.
DRS Differential-reflectance spectroscopy.
DIIS Direct inversion in the iterative subspace.
XC Exchange–correlation functional.
GGA Generalised gradient approximation.
GHG Greenhouse gas.
GPW Gaussian and plane wave.
GTH Goedecker-Teter-Hutter pseudopotential.
GTOs Gaussian-type orbitals.
HEG Homogeneous electron gas.
HF Hartree Fock.
HL Helmholtz layer.
HF Hartree–Fock method.
IP-RPA Independent particle random phase approximation.
KS Kohn–Sham.
LCOH Levelised cost of hydrogen.
LDA Local density approximation.
LEED Low-energy electron diffraction.
NVT Canonical ensemble.
ONCV Optimised norm-conserving vanderbilt pseudopotential.
NDCs Nationally determined contributions.
PAW Projector augmented-wave method.
PBE Perdew-Burke-Ernzerhof functional.
PBE-D3 Dispersion correction with PBE functional.
PEC Photoelectrochemical.
PES Potential energy surface.
PV Photovoltaic

PV-E	Photovoltaic electrolysis.
QMC	Quantum monte carlo.
RA	Reflectance-anisotropy.
RPA	Random phase approximation.
RAS	Reflection anisotropy spectroscopy.
RDF	Radial distribution function.
SCF	Self-consistent field.
SCR	Space charge region.
SDR	Surface differential reflectivity.
SE	Scanning ellipsometry.
SEM	Scanning electron microscopy.
SIE	Self interaction error.
SIC	Self interaction correction.
SMR	Steam methane reforming.
STH	Solar-to-hydrogen.
STM	Scanning tunnelling microscopy.
TRL	Technological readiness level.

8 List of Symbols

α_μ **and** $\mathbf{d}_{\mu p}$ Gaussian component and contraction coefficient for GTOs.

α Mixing parameter for the Hartree-Fock (exact) exchange energy.

α **and** β Mixing parameters in SCF via DIIS.

κ **and** μ Parameters used in PBE framework.

ρ Electron density.

$\tilde{\rho}(\mathbf{r})$ Trial electron density.

$\psi(\mathbf{r})$ Kohn–Sham orbital.

$\{\chi(\mathbf{r})\}$ Basis function for linear-combination approach.

$\varepsilon_{xc}^{\mathbf{HEG}}(\rho)$ Exchange-correlation energy per atom of a uniform density.

$\varepsilon_{x}^{\mathbf{LDA}}(\rho)$ Exchange component of the in the LDA framework.

ε_s**'** **and** ε_s**"** Real and imaginary part of the bulk dielectric function.

λ Photon wavelength.

ε_b Bulk dielectric function.

$\Delta\varepsilon_s$ Anisotropic part of surface dielectric tensor.

$\Delta\varepsilon$**'** **and** $\Delta\varepsilon$**"** Anisotropic real and imaginary part of the surface dielectric function.

ΔH_f^{InP} Bulk formation energy of InP.

$\mathbf{N}_e$ Number of electrons.

ΔR Change in absolute reflectivity.

$\nabla\rho(\mathbf{r})$ Reduced density gradient.

γ Gibbs free surface energy.

$\mathbf{A}$ Slab surface area.

μ Chemical potential.

$\mu_{In,bulk}$ Bulk indium chemical potential.

$\mu_{P,bulk}$ Bulk phosphorus chemical potential.

λ Thermal wavelength of O_2.

Φ Work function difference between the semiconductor and the redox couple.

$\mathbf{C}_{ij}^n$ Dispersion energy coefficients for D3 correction.

$\mathbf{C}_{ij}^n$ Dispersion energy coefficients for D3 correction.

C_μ SCF determined expansion coefficient.

$\mathbf{G}$ Reciprocal lattice vector.

$E[\rho_0]$ Energy for the ground-state electron density.

$E[\tilde{\rho}]$ Energy for the trial electron density.

$E_{xc}[\rho]$ Exchange-correlation functional.

$\mathbf{E}_{cut}$ Kinetic energy cutoff.

$E_{xc}^{LDA}[\rho]$ Exchange-correlation functional in the LDA framework.

$\mathbf{F}_{x}^{PBE}\mathbf{(s)}$ Enhancement factor used in PBE framework.

$\mathbf{E}_{x}^{hybrid}$ Hybrid XC energy.

$\mathbf{E}_{x}^{PBE}$ Exchange energy component in PBE framework.

$\mathbf{E}_{C}^{PBE}$ Correlation energy component in PBE framework.

$\mathbf{E}_{x}^{HF}$ Hartree–Fock (exact)exchange energy.

$\mathbf{E}_{DFT-D3}$ Ground state energy after dispersion correction.

$\mathbf{E}_{disp}^{D3}$ Pairwise dispersion energy correction in D3 correction.

$\mathbf{E}_{x}^{hybrid}$ Hybrid XC energy.

$\mathbf{E}_{x}^{PBE}$ Exchange energy component in PBE framework.

$\mathbf{E}_{x}^{HF}$ Hartree–Fock (exact)exchange energy.

$\mathbf{E}_{DFT-D3}$ Ground state energy after dispersion correction.

$\mathbf{E}_{cut}$ Kinetic energy cutoff.

$E_{xc}^{LDA}[\rho]$ Exchange-correlation functional in the LDA framework.

$\mathbf{E}_{disp}^{D3}$ Pairwise dispersion energy correction in D3 correction.

$\mathbf{E}_{C}^{PBE}$ Correlation energy component in PBE framework.

$\mathbf{E}_{O_2}$ Spin-triplet ground state energy of O_2 from DFT.

E_{CB} Conduction band minimum.

E_{VB} Valence band maximum.

E_{VAC} Energy of the vacuum level.

E_{F} Fermi level.

$E_{R,O}$ Redox level of the electrolyte.

$\mathbf{E}_{nk}$ Energy of the n^{th} band at the wave-vector k.

$\mathbf{F}_{x}^{PBE}\mathbf{(s)}$ Enhancement factor used in PBE framework.

$\mathbf{R}_{clean}$ Reflectivity of a clean sample.

$\mathbf{R}_{ref}$ Reflectivity of a reference sample.

$\mathbf{H}$ Non-relativistic electronic hamiltonian.

$V_{Hartree}(\mathbf{r})$ Electrostatic potential for e–e repulsion.

$V_{xc}(\mathbf{r})$ Exchange-Correlation potential.

$V_{\mathbf{KS}}[\rho(\mathbf{r})]$ Effective(fictitious) external potential.

$V_{\mathbf{ext}}$ Electron–nulcei interaction in Kohn–Sham framework.

$V_{\mathbf{loc^{PP}}}$ Local pseudoptential.

$V_{\mathbf{nl^{PP}}}$ Non-local pseudopotential.
$v_H(\mathbf{r})$ Hartree potential.
$v_{\mathbf{ext}}(\mathbf{r})$ external potential.
$\mathbf{N}_{nucl}$ Number of nulcei.
$T_s[\rho]$ Kinetic energy of non-interacting electrons.
R_i Residual vector between input $ densities.
$\mathbf{k}_B$ Boltzmann constant.
$\mathbf{Z}_{rot}$ Rotational partition function.
$\mathbf{Z}_{vib}$ Vibrational partition function.
$L(\{\mathbf{R}_I\},\{\dot{\mathbf{R}}_I\})$ Lagrangian used in AIMD for depicting nuclear motion.
r[110] Reflectivity along [110] direction.
P_{vc} Momentum transition matrix(valence to conduction).
d Layer thickness.
d_{sc} Thickness of the space charge region d_H Helmholtz layer width.
$\mathbf{f}^n_{damp}$ Damping coefficient for D3 correction.
r Total reflectivity.
V_{bb1} Band bending induced potential drop in the absence of surface states.
V_{bb2} Band bending potential drop in the presence of surface states. $\mathbf{Z}$ Charge of nucleus.
Ψ_H Potential drop across the Helmholtz layer.
$\Delta\mathbf{r}$ Reflectivity difference between two orthogonal in–plane directions.
r[$\tilde{1}$10] Reflectivity along [$\tilde{1}$10] direction.
[110] Reflectivity along [110] direction.
ω Photon frequency.
$\mathbf{r}^{surf}_{In-P}$ Bond distance of In, P atoms at the surface.
$\mathbf{r}^{bulk}_{In-P}$ Bond distance of In, P atoms in the bulk.
$\mathbf{r}_{(In-P)}\mathbf{(t)}$ Time distribution of In, P atomic distances for surface, near-surface regions.

9 Appendix

Herein, we provide the technical details and the approach that support the analysis of the publication *A2*. This appendix includes regarding electronic property calculations

wrt. different exchange-correlation functionals, and the "*scissor operator*" fitting procedures used to align PBE-derived with PBE0-derived band structure. This is to ensure the accuracy of the optical spectra.

9.1 Electronic Properties

The electronic band structure of semiconductor surfaces plays a crucial role in the efficiency and stability of PEC devices. However, accurate modelling of electronic properties remains a challenge, especially at the solid–liquid interface, due to the interplay between surface reconstruction, adsorbate coverage, and electrochemical environment.

DFT, using the PBE exchange-correlation functional as applied in this work is a common tool. However, there are some problems in this approach:

1. Underestimation of the Band Gap: GGA-type functionals (Sec. 4.1.6), such as PBE, underestimate the band gap due to self-interaction errors (SIE) and the absence of the derivative discontinuity in the exchange-correlation potential. Furthermore, even after application of self-interaction corrections (SIC) in the GGA framework, these methods incorporate gauge inconsistency issues [92, 93].

2. Finite supercell and sampling Effects: The finite-size of the surface slabs and limited k-point sampling (Fig. 34) can affect the results based on surface properties, such as RAS.

Herein, Fig. 35a represents the band structure of the $\beta 2(2\times 4)(P_2O_7)_2$ surface, showing the presence of surfaces states. Fig. 35b, corresponds to the change in the band gap value obtained for stable surfaces at each specific oxygen coverage (θ). The band gap evolution shows a non-uniform distribution with coverage, showcasing the sensitivity of electronic properties to fluctuations as the coverage increases. Due to the inclusion of the exact exchange Eq. (4.27), the PBE0 hybrid functional yields a larger band gap, resulting in a value closer to experimental one. Changes in the band gap wrt. θ (Fig. 35b) can be correlated to shifting or removal of mid-gap states, which can alter the anisotropic response of the surface, as exemplified in Sec. 5.2.1 and 5.2.2.

One must address the limitations of semi-local functionals, particularly in calculations of optical anisotropy, which is highly sensitive to the distribution of surface electronic states in the reciprocal space. Since RAS calculations require an accurate band structure calculation, the PBE band structures were corrected to match the BE0-derived energies,

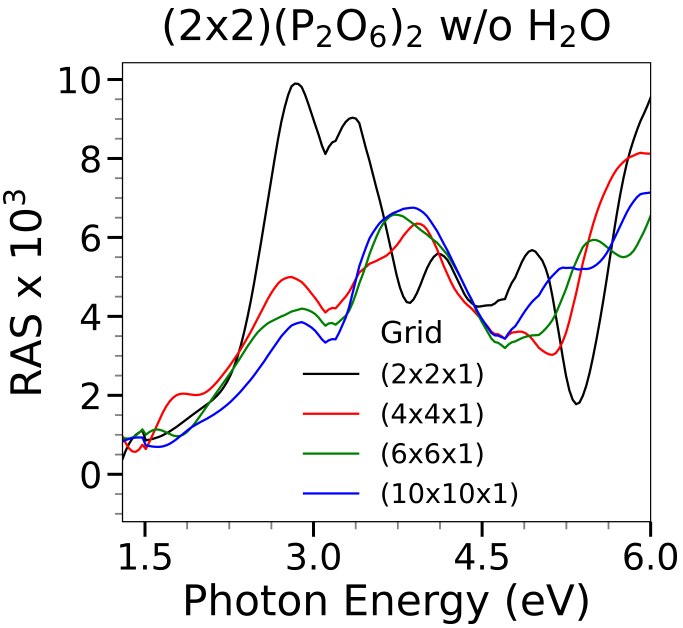

Figure 34: (a) Change in RA-spectra wrt. different k-point grids for $(2\times2)(P_2O_6)_2$ solid–vacuum interface. The RA-spectra for the $(4\times4\times1)$ grid corresponds to the 14.5 ps snapshot.

using a linear fitting and *scissors operator* approach. For each oxygen coverage, separate linear regressions were performed for the valence- and conduction-band energies within a varying energy window around the valence band maximum (VBM) and conduction band minimum (CBM), as implemented in a custom made fitting script. After applying the fitting procedure we get the scaling parameters that relate the PBE bands to their PBE0 counterparts:

$$E_{\mathrm{VB}}^{\mathrm{fit}}(k) = \left(E_{\mathrm{VB}}^{\mathrm{PBE}}(k) - E_{\mathrm{VB,max}}^{\mathrm{PBE}}\right) \cdot v_{\mathrm{slope}} + v_{\mathrm{int}}\,, \tag{9.1}$$

$$E_{\mathrm{CB}}^{\mathrm{fit}}(k) = \left(E_{\mathrm{CB}}^{\mathrm{PBE}}(k) - E_{\mathrm{VB,max}}^{\mathrm{PBE}}\right) \cdot c_{\mathrm{slope}} + c_{\mathrm{int}} + \Delta_{\mathrm{scissor}}\,. \tag{9.2}$$

where v_{slope} and c_{slope} are the regression-derived scaling factors for the valence and conduction bands, respectively, while v_{int} and c_{int} denote the corresponding intercepts. The parameter $\Delta_{\mathrm{scissor}}$ represents an empirical energy shift applied to rigidly correct the underestimated PBE band gap. This correction is determined such that the adjusted bulk gap reproduces the experimental value of 1.34 eV, guided by the PBE0 reference calculations [94, 95]. The applied parameters for this surface configuration are illustrated in

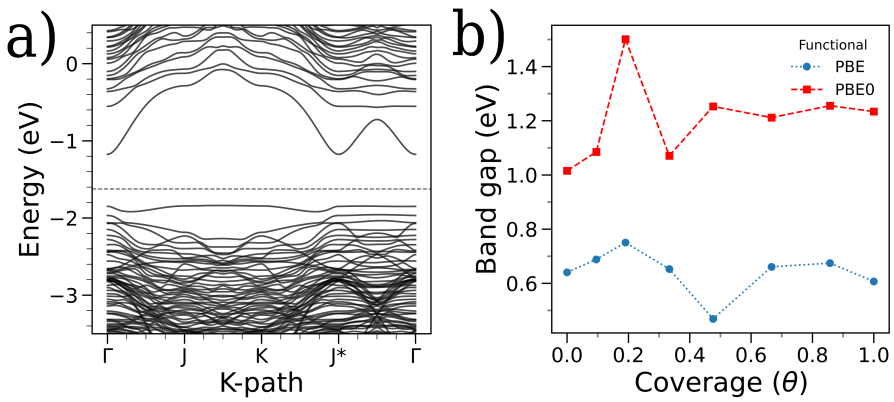

Figure 35: (a) PBE-derived band structure of the oxygen-covered $\beta_2(2\times4)(P_2O_7)_2$ reconstruction of InP(001), (b) PBE and the PBE0-derived band gaps as a function of oxygen coverage (θ), showing a fluctuation in the electronic states during the transformation between different surface phases.

Fig. 36, where the values ($\Delta_{\textbf{scissor}}$**: 0.632,** $c_{\textbf{slope}}$**: 1.089**, $v_{\textbf{slope}}$**: 1.133**) correspond to the scissor shift, conduction-band slope, and valence-band slope respectively.

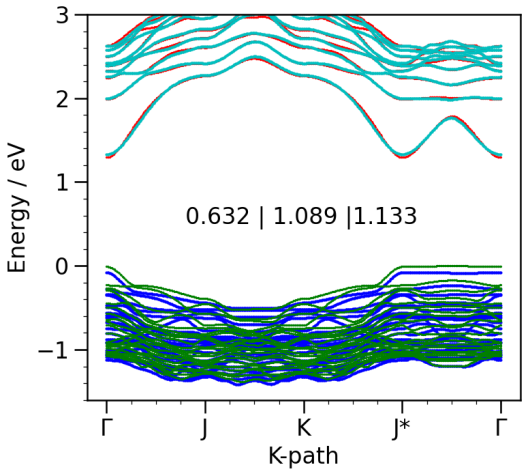

Figure 36: Comparison of the PBE (blue/green) and PBE0 (red/cyan) band structures for the oxidised $\beta 2(2\times4)$ surface at a representative oxygen coverage. The bands are aligned at the valence band maximum and scaled using a linear regression fit to match the PBE0-like dispersion. This figure is taken from the paper *A2*.

. Hence, applying a scissor shift for calculation of optical response provides a more accurate representation of the quasiparticle gap, ensuring a more realistic description of

optical and electronic transitions without the full computational expense of hybrid-DFT based calculations.

The scissor shift correction is used in the calculation of time-resolved reflection anisotropy spectroscopy for all solid–liquid and solid–vacuum interfaces, as discussed in Sec. 5.2.

9.2 Data availability

The data that support the findings of the publication *A1*, including structure files of the most stable structures, are openly available at: NOMAD [96].

The molecular dynamics trajectories that support the findings of the publication *A2* are openly available at: ZENODO [97].

The data underlying the study of publication *A3* will be made openly available upon reasonable request to the authors.

Bibliography

[1] Lee H. and Romero J., editors. Climate Change 2023: Synthesis Report. Intergovernmental Panel on Climate Change (IPCC), July 2023. [Core Writing Team, H. Lee and J. Romero (eds.)].

[2] Pörtner H-O., Roberts D. C., Masson-Delmotte V., Zhai P., Tignor M., et al. The ocean and cryosphere in a changing climate. IPCC special report on the ocean and cryosphere in a changing climate, 1155:10–1017, 2019.

[3] Halkos G. E. and Gkampoura E-C. Reviewing usage, potentials, and limitations of renewable energy sources. Energies, 13(11):2906, June 2020.

[4] Xu J., Cai X., Cai S., Shao Y., Hu C., et al. High-energy lithium-ion batteries: Recent progress and a promising future in applications. Energy Environ. Mater., 6(5):e12450, January 2023.

[5] Abdelkareem M. A., Ayoub M., Khuri S., Alami A. H., Sayed E. T., et al. Environmental aspects of batteries. Sustain. Horiz., 8:100074, December 2023.

[6] McManus M. C. Environmental consequences of the use of batteries in low carbon systems: The impact of battery production. Appl. Energ., 93:288–295, May 2012.

[7] Oliveira L. M., Messagie M., Rangaraju S., Sanfelix J., Hernández Rivas M. F., et al. Key issues of lithium-ion batteries – from resource depletion to environmental performance indicators. J. Clean Prod., 108:354–362, December 2015.

[8] Mauger. A. and Julien C. M. Critical review on lithium-ion batteries: are they safe? sustainable? Ionics, 23(8):1933–1947, June 2017.

[9] IEA. Net Zero by 2050: A roadmap for the global energy sector (2021a), May 2021.

[10] May M. M. Seeking Order in Complex Electrochemical Interfaces: Insights for Energy Conversion Devices. ACS Energy Letters, 11(1):195–201, December 2025.

[11] Shaner M. R., Atwater H. A., Lewis N. S., and McFarland E. W. A comparative technoeconomic analysis of renewable hydrogen production using solar energy. Energy Environ. Sci., 9(7):2354–2371, May 2016.

[12] Farhana K., Mahamude A. S., and Kadirgama K. Comparing hydrogen fuel cost of production from various sources - a competitive analysis. Energ. Convers. Manage., 302:118088, February 2024.

[13] Pinaud B. A., Benck J. D., Seitz L. C., Forman A. J., Chen Z., et al. Technical and economic feasibility of centralized facilities for solar hydrogen production via photocatalysis and photoelectrochemistry. Energy Environ. Sci., 6(7):1983, June 2013.

[14] Grimm A., de Jong W. A., and Kramer G. J. Renewable hydrogen production: A techno-economic comparison of photoelectrochemical cells and photovoltaic-electrolysis. Int. J. Hydrogen Energ., 45(43):22545–22555, September 2020.

[15] May M. M., Stange H., Weinrich J., Hannappel T., and Supplie O. The impact of non-ideal surfaces on the solid-water interaction: a time-resolved adsorption study. SciPost Physics, 6(5):58, May 2019.

[16] Suresh Babu D., Schneider S., Rieth T., Sharp I. D., and Van de Krol R. Unassisted pec water splitting using iii–v multijunction photoabsorbers: Insights into the degradation mechanism. ACS Appl. Energy Mater., pages 16320–16332, October 2025.

[17] Heller A., Miller B., Lewerenz J., and Bachmann K. J. An efficient photocathode for semiconductor liquid junction cells: 9.4% solar conversion efficiency with p-InP/VCl_3-VCl_2-HCl/C. JACS, 102(21):6555–6556, October 1980.

[18] Schmitt E. A., Guidat M., Nusshör M., Renz A-L, Möller K., et al. Photoelectrochemical Schlenk cell functionalization of multi-junction water-splitting photoelectrodes. Cell Rep. Phys. Sci., 4(10):101606, October 2023.

[19] May M. M., Lewerenz H-J., and Hannappel T. Optical in Situ Study of InP(100) Surface Chemistry: Dissociative Adsorption of Water and Oxygen. J. Phys. Chem. C, 118(33):19032–19041, August 2014.

[20] Muñoz A. G., Heine C., Klemm H. W., Hannappel T., Szabo N., et al. Electrochemical Passivation of Homoepitaxial InP (100) Thin Films for Light Induced Hydrogen Evolution: A Synchrotron Radiation Photoelectron Spectroscopy Study. ECS Trans., 35(8):141–150, April 2011.

[21] Young J. L., Döscher H., Turner J. A., and Deutsch T. G. Reversible $GaInP_2$ Surface Passivation by Water Adsorption: A Model System for Ambient-Dependent Photoluminescence. J. Phys. Chem. C, 120(8):4418–4422, February 2016.

[22] Yadav V., Euchner H., and May M. M. Surface Dynamics of Clean and Oxygenated InP(001) Surfaces in Contact with Water—Insights from Computational Spectroscopy. ChemCatChem, 18(1):e01347, January 2026.

[23] Hannppel T., Shekarabi S., Jaegermann W., Runge E., Hofmann J.P., et al. Integration of Multijunction Absorbers and Catalysts for Efficient Solar-Driven Artificial Leaf Structures: A Physical and Materials Science Perspective. Sol. RRL, 8(11):2301047, April 2024.

[24] Schleuning M., Ahmet I. Y., Van de Krol R., and May M. M. The role of selective contacts and built-in field for charge separation and transport in photoelectrochemical devices. Sustainable Energy Fuels, 6(16):3701–3716, June 2022.

[25] Jacobsson T. J., Fjällström V., Edoff M., and Edvinsson T. Sustainable solar hydrogen production: from photoelectrochemical cells to PV-electrolyzers and back again. Energy Environ. Sci., 7(7):2056–2070, April 2014.

[26] Kaufman. A. J., Nielander A. C., Meyer G. J., Maldonado S., Ardo S., et al. Absolute band-edge energies are over-emphasized in the design of photoelectrochemical materials. Nat. Catal., 7(6):615–623, June 2024.

[27] Flieg M., Guidat M., and May M. M. Observation and Control of Potential-Dependent Surface-State Formation at a Semiconductor-Electrolyte Interface via Optical Anisotropy. Phys. Rev. Lett., 135(26):268001, December 2025.

[28] Gerischer H. The role of semiconductor structure and surface properties in photoelectrochemical processes. J. Electroanal. Chem. Interf. Electrochem., 150(1–2):553–569, July 1983.

[29] Tournet J., Lee Y., Karuturi S. K., Tan M. H., and Jagadish C. III-V Semiconductor Materials for Solar Hydrogen Production: Status and Prospects. ACS Energy Lett., 5(2):611–622, February 2020.

[30] Nielander A. C., Shaner M. R., Papadantonakis K. M., Francis S. A., and Lewis N. S. A taxonomy for solar fuels generators. Energy Environ. Sci., 8:16–25, September 2015.

[31] Feifel M., Lackner D., Ohlmann J., Benick J., Hermle M., et al. Direct Growth of a GaInP/GaAs/Si Triple-Junction Solar Cell with 22.3% AM1.5g Efficiency. Solar RRL, 3(12):1900313, December 2019.

[32] Schmidt W. G., Fattebert J. L., Bernholc J., and Bechstedt F. Self-energy effects in the optical anisotropy of GaP(001). Surf. Rev. Lett., 06(06):1159–1165, December 1999.

[33] Schmidt W. G. III-V compound semiconductor (001) surfaces. Appl. Phys. A, 75(1):89–99, July 2002.

[34] Pham T. A., Zhang X., Wood B. C., Prendergast D., Ptasinska S., et al. Integrating Ab Initio Simulations and X-ray Photoelectron Spectroscopy: Toward A Realistic Description of Oxidized Solid/Liquid Interfaces. J. Phys. Chem. Lett., 9(1):194–203, December 2017.

[35] Wood B. C., Ogitsu T., and Schwegler E. Local structural models of complex oxygen- and hydroxyl-rich GaP/InP(001) surfaces. J. Chem. Phys., 136(6):064705, February 2012.

[36] May M. M., Lewerenz H-J., Lackner D., Dimroth F., and Hannappel T. Efficient Direct Solar-to-Hydrogen Conversion by In Situ Interface Transformation of a Tandem Structure. Nat. Commun., 6:8286, 09 2015.

[37] Wood B. C., Schwegler E., Choi W. I., and Ogitsu T. Surface Chemistry of GaP(001) and InP(001) in Contact with Water. J. Phys. Chem. C, 118(2):1062–1070, December 2014.

[38] Wood B. C., Schwegler E., Choi W. I., and Ogitsu T. Hydrogen-Bond Dynamics of Water at the Interface with InP/GaP(001) and the Implications for Photoelectrochemistry. J. Am. Chem. Soc., 135(42):15774–15783, October 2013.

[39] Löw M., Guidat M., Kim J., and May M. M. The Interfacial Structure of InP(100) in Contact with HCl and H_2SO_4 studied by Reflection Anisotropy Spectroscopy. RSC Adv., 12:32756–32764, November 2022.

[40] Selci. S., Ciccacci F., Chiarotti G., Chiaradia P., and Cricenti A. Surface differential reflectivity spectroscopy of semiconductor surfaces. J. Vac. Sci. Technol., A, 5(3):327–332, May 1987.

[41] Cchiaradia P. and Sole R. D. Differential-reflectance spectroscopy and reflectance-anisotropy spectroscopy on semiconductor surfaces. Surf. Rev. Lett., 06(03n04):517–528, June 1999.

[42] Weightman P., Martin D. S., and Maunder A. J. RAS: a new probe of surface states. J. Electron Spectrosc. Relat. Phenom., 114:1069–1076, March 2001.

[43] Vazquez-Miranda S., Solokha V., Balderas-Navarro R. E., Hingerl K., and Cobet C. Adsorbate Isotherm Analysis by Reflection Anisotropy Spectroscopy on Copper (110) in Hydrochloric Acid. J. Phys. Chem. C, 124(9):5204–5212, February 2020.

[44] Hingerl L., Aspnes D. E., and Kamiya I. Comparison of reflectance difference

spectroscopy and surface photoabsorption used for the investigation of anisotropic surfaces. Surf. Sci., 287–288:686–692, May 1993.

[45] Ortega-Gallegos J., Guevara-Macías L. E., Ariza-Flores A. D., Castro-García R., Lastras-Martínez L. F., et al. On the origin of reflectance-anisotropy oscillations during GaAs (001) homoepitaxy. Appl. Surf. Sci., 439:963–967, May 2018.

[46] Großmann M., Hanke K. D., Bohlemann C. Y., Paszuk A., Hannappel T., et al. On the origin of bulk-related anisotropies in surface optical spectra. Commun. Mater., 7(1), February 2026.

[47] McGilp J. Epioptics: linear and non-linear optical spectroscopy of surfaces and interfaces. J. Phys. Condens. Matter, 2(40):7985–8006, October 1990.

[48] Martin D. S., Maunder A., and Weightman P. Thermal behavior of the Cu(110) surface studied by reflection anisotropy spectroscopy and scanning tunneling microscopy. Phys. Rev. B, 63(15):155403, March 2001.

[49] Oliveira E., Strassner J., Doering C., and Fouckhardt H. Reflectance anisotropy spectroscopy (RAS) for in-situ identification of roughness morphologies evolving during reactive ion etching (RIE). Appl. Surf. Sci., 611:155769, February 2023.

[50] May M. M. and Sprik M. Water adsorption on the P-rich GaP(100) surface: optical spectroscopy from first principles. New J. Phys., 20(3):033031, March 2018.

[51] Schmidt W. G. Calculation of reflectance anisotropy for semiconductor surface exploration. Phys. Status Solidi B, 242(13):2751–2764, October 2005.

[52] Albrecht S., Reining L., Sole R. D., and Onida G. Ab Initio Calculation of Excitonic Effects in the Optical Spectra of Semiconductors. Phys. Rev. Lett., 80(20):4510–4513, May 1998.

[53] Ruiz Alvarado I. A., Zare Pour M. A., Hannappel T., and Schmidt W. G. Structural fingerprints in the reflectance anisotropy of AlInP(001). Phys. Rev. B, 108(4):045410, July 2023.

[54] Leist J., Kim J., Euchner H., and May M. M. The relevance of structural variability in the time-domain for computational reflection anisotropy spectroscopy at solid–liquid interfaces. J. Phys.: Condens. Matter, 36(18):185002, February 2024.

[55] Hohenberg P. and Kohn W. Inhomogeneous Electron Gas. Phys. Rev., 136(3B):B864–B871, November 1964.

[56] Seidl A., Görling A., Vogl P., Majewski J. A., and Levy M. Generalized Kohn-Sham schemes and the band-gap problem. Phys. Rev. B, 53(7):3764–3774, February 1996.

[57] Martin R. M. Important preliminaries on atoms, page 173. Cambridge University Press, June 2004.

[58] Martin R. M. Electronic Structure: Basic Theory and Practical Methods. Cambridge University Press, April 2004.

[59] Goedecker S., Teter M., and Hutter J. Separable dual-space Gaussian pseudopotentials. Phys. Rev. B, 54(3):1703–1710, July 1996.

[60] Hamann D. R., Schlüter M., and Chiang C. Norm-Conserving Pseudopotentials. Phys. Rev. Lett., 43(20):1494–1497, November 1979.

[61] Vanderbilt D. Soft self-consistent pseudopotentials in a generalized eigenvalue formalism. Phys. Rev. B, 41(11):7892–7895, April 1990.

[62] Blöchl P. E. Projector augmented-wave method. Phys. Rev. B, 50(24):17953–17979, December 1994.

[63] VandeVondele J. and Hutter J. Gaussian basis sets for accurate calculations on molecular systems in gas and condensed phases. J. Chem. Phys., 127(11):114105, September 2007.

[64] Giannozzi P., Baroni S., Bonini N., Calandra M., Car R., et al. QUANTUM ESPRESSO: a modular and open-source software project for quantum simulations of materials. J. Phys.: Condens. Matter, 21(39):395502, September 2009.

[65] Kühne. T. D., Iannuzzi M., Del Ben M., Rybkin V. V., Seewald P., et al. CP2K: An electronic structure and molecular dynamics software package - Quickstep: Efficient and accurate electronic structure calculations. J. Chem. Phys., 152(19):194103, May 2020.

[66] Ceperley D. M. and Alder B. J. Ground State of the Electron Gas by a Stochastic Method. Phys. Rev. Lett., 45(7):566–569, August 1980.

[67] Parr R. G. Density Functional Theory of Atoms and Molecules, pages 5–15. Springer Netherlands, 1980.

[68] Gell-Mann M. and Brueckner K. A. Correlation Energy of an Electron Gas at High Density. Phys. Rev., 106(2):364–368, April 1957.

[69] Perdew J. P., Burke K., and Ernzerhof M. Generalized Gradient Approximation Made Simple. Phys. Rev. Lett., 77(18):3865–3868, October 1996.

[70] Grimme S., Antony J., Ehrlich S., and Krieg H. A consistent and accurate ab initio parametrization of density functional dispersion correction (DFT-D) for the 94 elements H-Pu. J. Chem. Phys., 132(15):154104, April 2010.

[71] Vydrov O. A. and Van Voorhis T. Nonlocal van der Waals density functional: The simpler the better. J. Chem. Phys., 133(24):244103, December 2010.

[72] Niklasson A. M., Steneteg P., and Bock N. Extended Lagrangian free energy molecular dynamics. J. Chem. Phys., 135(16):164111, October 2011.

[73] Omelyan I. P., Mryglod I. M., and Folk R. Optimized Verlet-like algorithms for molecular dynamics simulations. Phys. Rev. E, 65(5):056706, May 2002.

[74] Jones A. and Leimkuhler B. Adaptive stochastic methods for sampling driven molecular systems. J. Chem. Phys., 135(8):084125, August 2011.

[75] Marx D. and Hutter J. Ab initio molecular dynamics: Theory and implementation. Modern methods and algorithms of quantum chemistry, 1(301-449):141, 2000.

[76] Kirchner B., di Dio P. J., and Hutter J. Multiscale Molecular Methods in Applied Chemistry. Springer Berlin Heidelberg, 2012.

[77] McIntyre J. D. E. and Aspnes D. E. Differential reflection spectroscopy of very thin surface films. Surf. Sci., 24(2):417–434, February 1971.

[78] Hogan C., Pulci O., Gori P., Bechstedt F., Martin D. S., et al. Optical properties of silicene, Si/Ag(111), and Si/Ag(110). Phys. Rev. B, 97(19):195407, May 2018.

[79] Hogan C., Del Sole R., and Onida G. Optical properties of real surfaces from microscopic calculations of the dielectric function of finite atomic slabs. Phys. Rev. B, 68(3):035405, July 2003.

[80] Marini A., Hogan C., Grüning M., and Varsano D. yambo: An ab initio tool for excited state calculations. Comput. Phys. Commun., 180(8):1392–1403, August 2009.

[81] Sangalli D., Ferretti A., Miranda H., Attaccalite C., Marri I., et al. Many-body perturbation theory calculations using the yambo code. J. Phys.: Condens. Matter, 31(32):325902, May 2019.

[82] Zhang X., Ogitsu T., Wood B. C., Pham T. A., and Ptasinska S. Oxidation-induced polymerization of inp surface and implications for optoelectronic applications. J. Phys. Chem. C, 123(51):30893–30902, November 2019.

[83] Yadav V., Euchner H., and May M. M. The phase stability of InP(001) surfaces upon oxygen exposure from first principles. RSC Adv., 15(11):8464–8470, March 2025.

[84] Guo Q., Pemble M. E., and Williams E. M. Structural transformations of InP(001) surfaces. Surf. Sci., 468(1–3):92–100, November 2000.

[85] Schmidt W. G., Bechstedt F., Esser N., Pristovsek M., Schultz Ch., and Richter W. Atomic structure of InP(001)-(2×4): A dimer reconstruction. Phys. Rev. B, 57(23):14596–14599, June 1998.

[86] Chen G., Visbeck S. B., Law D. C., and Hicks R. F. Structure-sensitive oxidation of the indium phosphide (001) surface. J. Appl. Phys., 91(11):9362–9367, June 2002.

[87] Ruiz Alvarado I. A., Karmo M., Runge E., and Schmidt W. G. InP and Al-InP(001)(2 × 4) Surface Oxidation from Density Functional Theory. ACS Omega, 6(9):6297–6304, February 2021.

[88] Euchner H., Yadav V., and May M. M. The InP(100) Surface Phase Diagram: From the Gas Phase to the Electrochemical Environment. ACS Appl. Mater. Interfaces, 17:8601–8609, January 2025.

[89] Großmann M., Thieme M., Grunert M., and Runge E. Many-body perturbation theory vs. density functional theory: a systematic benchmark for band gaps of solids. npj Computational Materials, 12(1), January 2026.

[90] Sagisaka K., Nara J., and Bowler D. Importance of bulk states for the electronic structure of semiconductor surfaces: implications for finite slabs. J. Phys. Condens. Matter, 29(14):145502, March 2017.

[91] Vazhappilly T. and Micha D. A. Computational Modeling of the Dielectric Function of Silicon Slabs with Varying Thickness. J. Phys. Chem. C, 118(8):4429–4436, February 2014.

[92] Bhattarai P., Wagle K., Shahi C., Yamamoto Y., Romero S., et al. A step in the direction of resolving the paradox of Perdew–Zunger self-interaction correction. II. Gauge consistency of the energy density at three levels of approximation. J. Chem. Phys., 152(21):214109, June 2020.

[93] Bhattarai P., Santra B., Wagle K., Yamamoto Y., Zope R. R., et al. Exploring and enhancing the accuracy of interior-scaled Perdew–Zunger self-interaction correction. J. Chem. Phys., 154(9):094105, March 2021.

[94] Adamo C. and Barone V. Toward reliable density functional methods without adjustable parameters: The PBE0 model. J. Chem. Phys., 110(13):6158–6170, April 1999.

[95] Borlido P., Aull T., Huran A. W., Tran F., Marques M. A., et al. Large-Scale Benchmark of Exchange–Correlation Functionals for the Determination of Electronic Band Gaps of Solids. J. Chem. Theory Comput., 15(9):5069–5079, July 2019.

[96] Vibhav Yadav, Holger Euchner, and Matthias M. May. NOMAD dataset: InP(001)-Ox, 2025.

[97] Vibhav Yadav, Holger Euchner, and Matthias M. May. ZENODO dataset: InP(001)-Ox-AIMD, 2025.

RSC Advances

PAPER

View Article Online
View Journal | View Issue

Cite this: *RSC Adv.*, 2025, **15**, 8464

The phase stability of InP(001) surfaces upon oxygen exposure from first principles

Vibhav Yadav,[a] Holger Euchner [a] and Matthias M. May *[ab]

Received 5th February 2025
Accepted 12th March 2025

DOI: 10.1039/d5ra00855g

rsc.li/rsc-advances

III–V semiconductors such as indium phosphide and multinary alloys derived thereof have shown high performance in multi-junction photoelectrochemical devices for solar water splitting. However, electrochemical conditions, especially in aqueous electrolytes, often lead to changes in surface structure and stoichiometry. These changes then affect the electronic structure, for instance leading to the formation of charge-carrier recombination centers or points of attack for dissolution of the material. It is therefore important to understand the surface structures that may arise in electrochemical environments to identify routes for electronic and electrochemical surface passivation. In this work, we assess the impact of oxygen adsorption on surface reconstructions of InP(001) *via* first principle calculations. We observe predominantly P-rich surfaces for a large range of indium and oxygen chemical potentials, showing P_xO_y-type polyphosphate motifs. On the other hand, the frequently assumed In-rich (2 × 4) mixed-dimer surface reconstruction is found to be unstable for a large range of oxygen chemical potentials.

1 Introduction

Transitioning towards renewable energy sources to reduce the reliance on fossil fuels is crucial for limiting global warming.[1] Hydrogen produced from solar water splitting, as a carbon-neutral fuel has had a substantial amount of research put-forth in the recent years.[2–4] In particular, photo-electrochemical (PEC) water splitting is a promising option for hydrogen production. However, maintaining high solar-to-hydrogen efficiency over the necessary lifetime of the device remains a problem due to the semiconductor–electrolyte interface on the top photoabsorber.[5,6] Hence, it is crucial to understand the underlying facets necessary to improve the sustenance of photoelectrodes for direct solar water splitting, where the photabsorber is in contact with the electrolyte.[4,7]

Limiting (photo)corrosion that can lead to mid-gap states resulting in charge-recombination is therefore essential for viable PEC devices. Here, suitable surface passivation can suppress surface states, reduce recombination, and protect the surface from corrosion, thus solving problems related to the device's instability.[4,8] The first step for the knowledge-driven design of such a surface passivation is to understand the change in the electronic structure that may arise at the semiconductor surface under operating conditions. Here, Indium Phosphide (InP) is often applied as model system to gain insights into (photo)-electrochemical processes. InP is a (cubic) zinc-blende structured III–V semiconductor compound with electrical and optical properties that render it valuable for a range of opto-electronic applications, including photonic crystals,[9] energy harvesting and storage.[10] InP possesses a direct bandgap of 1.34 eV alongside high electron mobility. The material can be prepared epitaxially in high-quality, but also serves as a wafer-based substrate for a variety of opto-electronic devices.[11] These properties make InP particularly attractive for high-efficiency solar cells and photoelectrochemical water splitting applications. For instance, when alloyed with gallium to form $GaInP_2$, InP demonstrates promising solar-to-hydrogen conversion efficiencies as part of the absorber stack in tandem configurations, but also the charge-selective window layer in the form of $Al_xIn_{1-x}P$.[4] Due to the challenges that arise for the study of electrochemical systems under realistic conditions, both experimentally and computationally,[12,13] a widely used approach is to study the surface chemistry in vacuum conditions under the supply of oxygen or water.[14–18] These studies found the oxidation of InP to be a highly structure-sensitive process that exhibits distinct behaviour for In- and P-rich surfaces. The supply of molecular oxygen leads to oxygen insertion into In–In and In–P back bonds on the respective surfaces,[14] while water preferentially interacts with surface In–P bonds.[15] An in-depth computational study of Wood *et al.*[19] was mainly based on the In-rich, mixed-dimer reconstruction of InP(001) and used adatom adsorption and density-functional theory (DFT)-based molecular dynamics calculations of the solid–liquid-interface. They found the predominant formation of In–O–In and In–O–P bonds for the mixed-dimer reconstruction, identifying In–O–In as being more detrimental due to in-gap electronic states.[19,20] An adsorbate-assisted kinetic H_2O dissociation was also

[a]*Universität Tübingen, Institute of Physical and Theoretical Chemistry, D-72076 Tübingen, Germany. E-mail: matthias.may@uni-tuebingen.de*
[b]*Universität Tübingen, Center for Light-Matter Interaction, Sensors and Analytics LISA+, D-72076 Tübingen, Germany*

suggested, together with a long-range Grotthuss mechanism of surface hydrogen migration, which could enhance proton adsorption and hydrogen evolution at different surface sites. Work on the ternary $Al_xIn_{1-x}P$ suggested symmetric oxygen distribution on the InP mixed-dimer reconstructions after adsorption or substitutive insertion.[16] More complex motifs were found in a study combining near-ambient pressure photoelectron spectroscopy and DFT,[21] but the exact starting surface of the experimental study was not well-established. The sputtering routine described and the low-energy electron diffraction patterns suggest that the starting point was a surface similar to the mixed-dimer surface with a relatively high density of defects.[17] Surface defects, however, can qualitatively change the interaction of the III–V(001) surfaces with adsorbed water.[22] A recent computational study also suggested that the interaction of InP surfaces with hydrogen is strongly influenced by substrate doping, and the surface hydrogen content will impact electronic properties such as Fermi level pinning.[23]

Surface chemistry studies of clean InP(001) reconstructions apart from the mixed-dimer reconstruction are, however, rather limited, both computationally and experimentally. While well-ordered interfaces between InP and aqueous electrolytes have indeed been demonstrated to exist, their exact nature is not yet established.[24] In-rich and Cl-rich surfaces might be present in limited potential ranges. While our recent work using the computational hydrogen electrode suggests that H–Cl co-adsorption in these conditions may be thermodynamically limited under these conditions,[25] we did not consider oxygen as ingredient for the surface phases. To understand possible surface oxidation pathways, it is therefore necessary to systematically assess the phase diagram of InP(001) with respect to oxygen chemisorption with a broad structural basis.

In this work, we therefore first analyse the stability of clean InP(001) stable surface reconstructions with respect to the surface constituents chemical potential *via* density functional theory. Next, for stable surface reconstructions, we study the resulting phase stability due to dissociative chemisorption of O_2 *via* two different approaches. We find that the phase stability of polyphosphate moieties along with the insertion of O-atoms into the underlying In–P back bonds at higher coverages is evident in the overall phase diagram.

2 Methods

2.1 Computational details

For structural relaxation, we employed the Gaussian and Plane Wave (GPW) method with DZVP basis set as implemented in the DFT code CP2K[26] in combination with the non-local and norm-conserving GTH-PBE pseudopotentials. Exchange and correlation were accounted for *via* the generalised gradient approximation in the form introduced by Perdew, Burke, and Ernzerhof.[27,28] Furthermore, the Grimme-D3 correction[29] was added to consider van der Waals interactions in a pair-wise dispersion correction. After performing convergence tests to determine suitable layer and vacuum thickness, InP(001) slabs were generated for the subsequent surface studies. These slabs comprised 6 In and 6 P layers, where the bottom 5 bilayers were fixed to ideal bulk positions, and a vacuum of approximately $\approx$36 Å added along the surface normal. All surface calculations were conducted using an asymmetric slab, with the bottom In-layer being passivated with pseudo-hydrogen atoms ($Z = 1.25$). For k-space integration, $4 \times 4 \times 1$ and $4 \times 2 \times 1$ k-grids were selected, depending on the respective surface size.

2.2 Surface phase diagrams

To access the stability of different surface reconstructions with respect to each other, the Gibbs free surface energy, $\gamma = \Delta G/A$, was determined following eqn (1).

$$\gamma(T,p) = \frac{1}{A}\left(G(T,p,N_i) - \sum_i N_i\mu_i(T,p)\right) \quad (1)$$

Here, T and p represent temperature and pressure, whereas N_i and μ_i correspond to number and chemical potential of species i, respectively. While G in principle depends on temperature and pressure, it is often simply approximated in ab initio-based approaches by the calculated total energy of the corresponding slab, thus neglecting entropy and volume change. Moreover, for the sake of representation, the chemical potential is frequently normalised with respect to the bulk energies of the respective elements ($\Delta\mu_i(T, p) = \mu_i(T, p) - E_i$), thus yielding:

$$\gamma(T,p) = \frac{1}{A}\left(E_{\text{surf}} - \sum_i N_i\Delta\mu_i(T,p)\right) \quad (2)$$

Next, the fact that, in equilibrium, μ_{In} and μ_{P} are connected *via* the bulk formation energy of InP, can be exploited:

$$\mu_{\text{In}} + \mu_{\text{P}} = \mu_{\text{InP,bulk}} \quad (3)$$

$$= \mu_{\text{In,bulk}} + \mu_{\text{P,bulk}} - \Delta H_{\text{f}}^{\text{InP}} \quad (4)$$

Now, the surface free energy of the plain surfaces can be expressed solely as a function of $\Delta\mu_{\text{In}}$.[25]

The above expressions (see eqn (4)) can furthermore be used to determine the limits for $\Delta\mu_{\text{In}}$ (and $\Delta\mu_{\text{P}}$):

$$\Delta H_{\text{f}}^{\text{InP}} \leq \Delta\mu_{\text{In}} \leq 0 \quad (5)$$

The experimentally determined value for the InP formation energy corresponds to $\Delta H_{\text{f}}^{\text{InP}} = -0.81$ eV.

Starting from the clean surface reconstructions, the phase stability upon oxygen adsorption can consequently be represented as a function of $\Delta\mu_{\text{In}}$ and $\Delta\mu_{\text{O}}$. Here, it should be noted that the oxygen chemical potential can be expressed as a function of partial pressure, p, and temperature, T, as represented by the following equation:

$$\Delta\mu_{\text{O}}(p,T) = \frac{k_{\text{B}}T}{2}\left[\frac{p\lambda^3}{k_{\text{B}}T} - \ln Z_{\text{rot}} - \ln Z_{\text{vib}}\right] - \frac{1}{2}E_{\text{O}_2} \quad (6)$$

where k_{B} is the Boltzmann constant, λ is the de Broglie thermal wavelength of the O_2 molecule, and Z_{rot}, Z_{vib} are the rotational and vibrational partition functions of O_2, respectively. E_{O_2}

represents the energy of the oxygen molecule in its computational spin-triplet ground state.

3 Results & discussion

3.1 Phase stability – plain surface

As a first step, surface reconstructions of P-rich and In-rich phases, known to occur in InP and/or related compounds,[30–32] were re-examined to determine the surface phase diagram of InP(001) with the inclusion of dispersion corrections. Plausible structures that have been found to be stable in earlier studies were extracted from the literature and subsequently optimised. The ground state energies of the optimised structures were then used to determine the surface phase diagram as a function of the indium chemical potential as shown in Fig. 1. Five stable surface reconstructions are observed (see Fig. 2). The (2×2)-2D reconstruction is stable for a large range under P-rich conditions. For increasing $\Delta\mu_{In}$, the closely related $c(4 \times 4)$ phase becomes stable in a narrow potential range. Intermediate In chemical potentials stabilise the stepped $\beta2(2 \times 4)$ and $\alpha2(2 \times 4)$ phases, whereas the mixed-dimer surface is observed for In-rich conditions. On the contrary, the (2×2)-1D surface is found to be slightly unstable in contrast to previous reports in the literature.[32] This is most likely a consequence of the different exchange-correlation functional (LDA in their work, GGA in ours) as well as the fact that our work accounts for dispersion correction *via* the vdW-D3 scheme. For comparison, the phase-diagram was also recalculated, using LDA, to recognise the differences due to different classes of XC functional as previously reported.[32] The instability of (2×2)-1D reconstruction for PBE could be due to the inaccurate correlation energy calculation using LDA for inhomogeneous systems. In general, the results obtained *via* the here applied PBE-D3 approach are expected to be more reliable. However, it has to be noted that the observed differences to the previously published LDA phase diagram are small and that additional uncertainties, as *e.g.* entropic effects, are not considered.

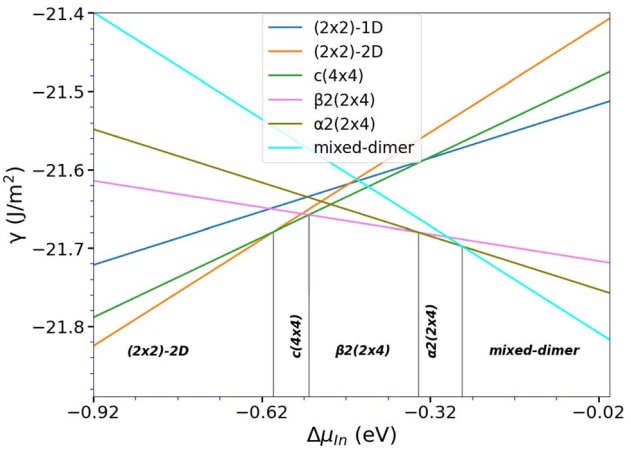

Fig. 1 Surface free energy for the different InP(001) reconstructions as function of the indium chemical potential.

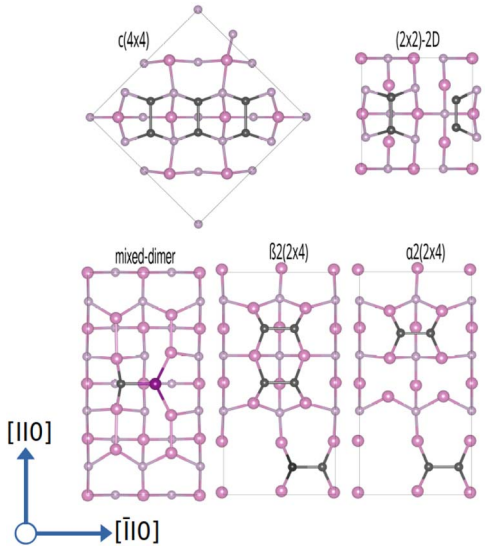

Fig. 2 Ball-and-stick representation for stable InP(001) surface reconstructions, viewed along the (001) surface normal. Surface dimers, *i.e.* P-dimers are indicated in dark grey, and In–P dimers are indicated in a magenta-dark grey format. In and P atoms are indicated by pink and grey respectively.

Finally, the unstable – no hydrogen termination was taken into account – P-rich (2×2) surface is also shown, as this surface becomes important as basis structure for the oxygenation study presented below.

The above-discussed surface reconstructions are depicted in Fig. 2. As these will be the starting point for the calculations in the presence of oxygen, their structural features will be quickly discussed. The P-rich (2×2)-2D and $c(4 \times 4)$ surfaces are terminated by additional P-dimers that are located on the already P-terminated InP(001) surface. In the case of the (2×2)-2D surface, two dimers that differ in length and position with respect to the underlying P-layer are observed. The closely related $c(4 \times 4)$ reconstruction is based on a $\sqrt{2} \times \sqrt{2}$ surface unit cell that is rotated by 45° wrt. the conventional one. This surface reconstruction corresponds to a P-terminated surface as well, however, with an additional row of three P-dimers on top. The $\beta2(2 \times 4)$ phase can be described as a stepped surface with In-termination, with two P-dimers on the upper and one on the lower plateau. The $\alpha2(2 \times 4)$ surface reconstruction, on the other hand, is based on the same stepped surface, however, with one P-dimer on top of and one below the step. Similarly, the P-rich (2×2) structure corresponds to a flat, In-terminated surface with P-dimers on top. This structure forms when a P-terminated surface is optimised and should not be confused with the above-discussed (2×2)-2D phase, where additional P-dimers are present. Finally, the mixed-dimer reconstruction corresponds to an In-rich surface, again based on a (2×4) surface unit cell with a single mixed-dimer on top of the In-termination.

3.2 Phase stability – oxygenated surface

Starting from the clean phase diagram, the above-mentioned stable reconstructions were investigated in the presence of

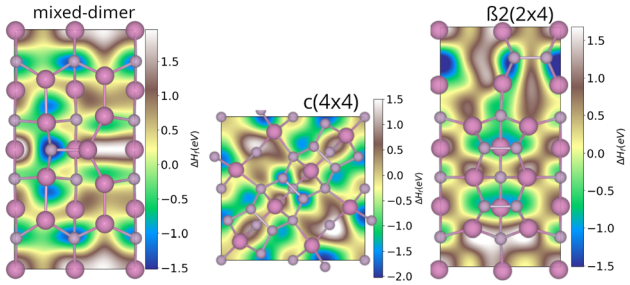

Fig. 3 Potential energy surfaces for oxygen adsorption on different InP(001) surface reconstructions. In and P atoms were constrained, whereas O was allowed to relax along the surface normal.

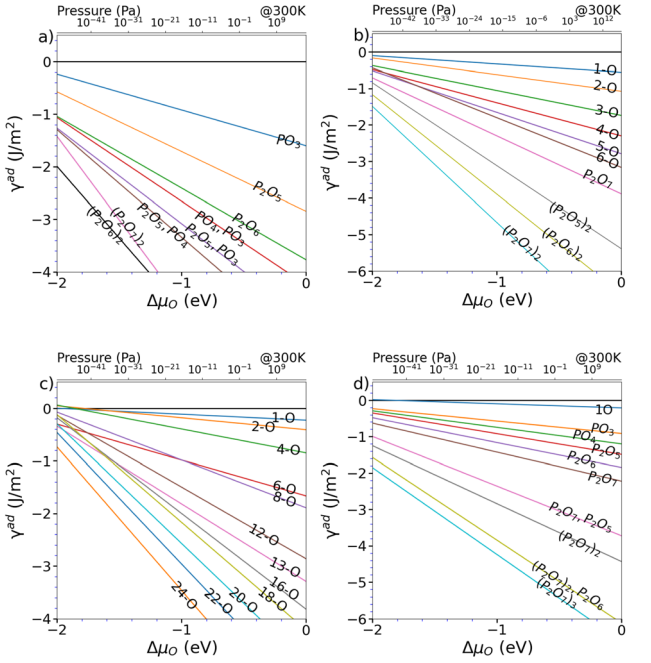

Fig. 4 Surface energy wrt. oxygen chemical potential of the energetically favourable O adsorption sites for (a) (2 × 2), (b) (2 × 2)-2D, (c) mixed-dimer and (d) β2(2 × 4) surface reconstructions.

oxygen. As a first step, the potential energy landscape of the respective surfaces was scanned by placing single oxygen atoms on a grid of equidistant points. The oxygen atoms were then relaxed along the surface normal, while the surface was kept fixed, thus yielding first insights with respect to the most likely adsorption sites. For the In-rich mixed-dimer surface, the energetically most favourable adsorption site was found to be the P-atom of the InP-dimer (see Fig. 3). This is in contrast with earlier findings on AlInP, where In was found to be more favourable for the mixed-dimer surface.[16] In addition, the In atoms next to the P atom of the InP dimer are likely to form In–O–In bonds, also showing negative adsorption energies. Finally, the P atoms below the top-most In layer, that are directly accessible, offer favourable adsorption sites indicating the formation of In–O–P bonds with neighbouring In atoms. For all P-rich surfaces, adsorption minima were found to be preferentially on P-dimer sites. This is exemplified for the β2(2 × 4) and $c(4 \times 4)$ phases in Fig. 3. Interestingly, for β2(2 × 4), the most favourable adsorption sites are on the P-dimers of the lower plateau, which can be explained by the vicinity of the step edge. The dimers on the upper plateau are also favourable adsorption sites, however, to a smaller extent. For the $c(4 \times 4)$ surface, the P-dimer sites, but also the P-atoms of the P-layer below, are favourable adsorption sites. Thus, it can be concluded that the P-sites are particularly reactive towards oxygen, even for In-rich surfaces.

Starting from the such determined minima, the surface was also allowed to relax and the amount of surface oxygen was then gradually increased. For the In-rich, mixed dimer surface, in accordance to literature, a screening-based increase of the oxygen content resulted in a rather uniform oxygen distribution. This is due to the fact that In–O–P and In–O–In bonds are formed preferentially, as already indicated by the colour map in Fig. 3. While the structures with rather low oxygen coverage keep the symmetry of the underlying mixed dimer surface, this symmetry is getting lost at higher oxygen concentration. Increasing the coverage beyond 12 oxygen atoms results in more strongly disordered arrangements on the surface as can be inferred from the (mixed) 24-O-structure in Fig. 5 and the supplementary dataset.[33] To evaluate the stability of the structures with different oxygen coverage, the corresponding phase diagram – depicting the surface free energy with respect to the oxygen chemical potential – were determined (see Fig. 4c). This clearly shows that oxygen-rich surfaces are rapidly stabilised with increasing $\Delta\mu_O$, with the surface that features the highest considered oxygen loading being stable over a wide range. Only at very low oxygen chemical potentials ($\Delta\mu_O < -2$ eV), some of the ordered low coverage phases become stabilised. However, at room temperature, such low chemical potentials would correspond to extremely low oxygen partial pressure, thus making their occurrence rather unlikely.

Interestingly, the oxygenation of the In-terminated surfaces with P-dimers on top was found to follow a different path. For example, for the case of the β2(2 × 4) phase, surface configurations with increased oxygen content were obtained by sequentially determining the most favourable position for each added oxygen. This resulted in the preferential formation of P–O and In–O–P bonds on P-dimers. However, at increased oxygen content, the occurrence of characteristic P_xO_y polyphosphate-type moieties was observed. The observation of these polyphosphates resulted in the question if such motifs might be stable also at lower oxygen contents. Consequently, an additional approach, based on the decoration of the surface with such structural motifs was followed. For this purpose, isolated PO_3, PO_4, P_2O_5, P_2O_6, and P_2O_7 motifs and combinations thereof were investigated and indeed proved to be more stable than the previously obtained structures with a more uniform distribution of oxygen. While the different polyphosphate moieties are in general observed to be the most stable structures for a given oxygen content, the P_2O_7-based motifs are found to be particularly stable configurations (see Fig. 5). A subset of these structures was also suggested by a study of Zhang *et al.*,[21] based on the interpretation of photoelectron spectroscopy data. The reason for this motif formation lies in

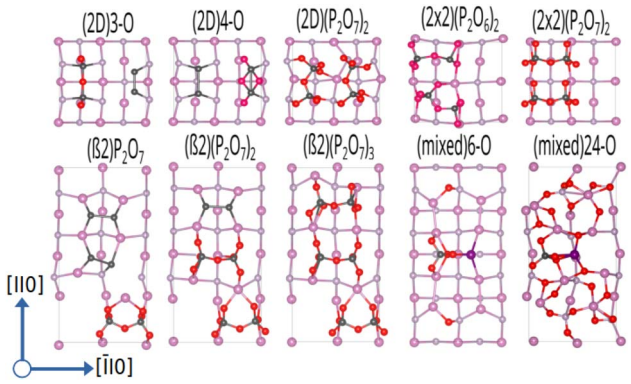

Fig. 5 Ball-and-stick representation for InP(001) oxygenated surface reconstructions, viewed along the (001) direction. To distinguish between the types of dimers, surface P-dimers are shown in dark grey, and In–P dimers are represented with a magenta-grey pattern. In, P, and O atoms are shown in pink, grey, and red, respectively.

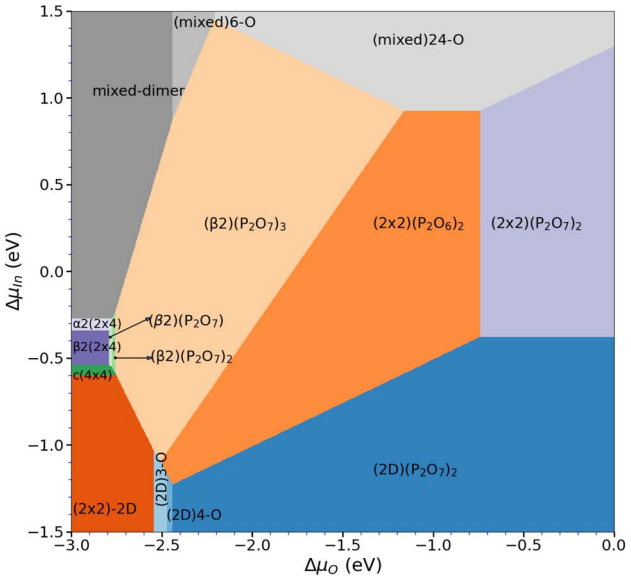

Fig. 6 Overall phase diagram of the oxygenated InP(001) surface, showing the most stable surface reconstructions as function of the chemical potentials of indium and oxygen.

the fact that oxygen strongly prefers to form bonds with phosphorous, such that P–O, P–O–P and predominantly P–O–In bonds are formed at higher oxygen content. Consequently, the number of available P-dimers on the β2(2 × 4) surface limits the polyphosphate formation, thus reaching its maximum when all three P-dimers are part of a P_2O_7 motif, corresponding to a surface with 21 adsorbed oxygen atoms, in the following also referred to as 21-O surface. With respect to the surface free energy, as in the case of the mixed dimer, the oxygen rich surfaces are, already at low values for $\Delta\mu_O$, dominating the phase diagram, with the maximum coverage of three P_2O_7 units being the most stable configuration over a wide chemical potential range (see Fig. 4d).

The α2(2 × 4) phase behaves in a similar fashion, the limiting concentration for polyphosphate formation here does, however, correspond to the 14-O surface, which shows P_2O_7 motifs on both available P-dimers. Increasing the oxygen content of the α2(2 × 4) phase beyond 14-O leads to an equivalent distribution of O-atoms around In sites. This results in the formation of In–O–In bonds with a disordered underlying In-layer.

As β2(2 × 4) and α2(2 × 4) correspond to stepped surfaces that are terminated by P-dimers, the question on the potential stability of a fully P-terminated, flat surface arises. For this purpose, the P-rich (2 × 2) surface, which previously was found to be unstable, was investigated for oxygen adsorption. Interestingly, P_2O_6 and P_2O_7 motifs forming additional In–O–In bonds in the In-termination are observed as most stable entities. The saturation of both P-dimers with oxygen results in the (2 × 2) phase, containing 14 oxygen atoms (14-O surface) as limiting case, as shown in Fig. 5. It has to be noted that this corresponds to a 28-O coverage for a (2 × 4) surface. With respect to the surface free energy, we again see a stabilisation of the structures with increased oxygen content already at low oxygen chemical potential. The maximum coverage of two P_2O_7 motifs is the energetically most favourable structure over a wide chemical potential range, down to $\Delta\mu_O \approx -1.75$ eV.

When considering the P-rich phases, the (2 × 2)-2D surface exhibits a strong preference for the formation of pholyphosphate moities (see Fig. 5). This involves the insertion of oxygen into the underlying In-layer of a P-terminated 2-P-dimer surface forming an In–O–P bond. As for the previous cases, P_2O_7 motifs were found to be the limiting case. This corresponds to a maximum of 14 oxygen (14-O phase) atoms when both top P-dimers are part of a P_2O_7 moiety. When the surface energy is considered, the oxygen-rich phases are again dominant, with the 14-O surface, *i.e.* (2 × 2)-2D$(P_2O_7)_2$, being the most stable one down to $\Delta\mu_O \ll -2.5$ eV (see Fig. 4b).

3.3 Phase stability – overall phase diagram

After assessing the phase diagrams of the different surface reconstructions with respect to the oxygen chemical potential, the question on the respective stability of these phases remains. For this purpose, we have determined the overall phase diagram, taking the chemical potentials of indium and oxygen into account (see eqn (2)). Indeed, already at rather low oxygen chemical potential, oxygenated surfaces become quickly more stable than the pristine clean surface reconstructions. However, the stability range of the different phases shifts significantly on the $\Delta\mu_{In}$ scale as can be seen in Fig. 6. In fact, starting from the clean surfaces, the β phase becomes dominant at rather low oxygen chemical potential covering a wide range of $\Delta\mu_{In}$ values. For increasing $\Delta\mu_O$, meaning more oxygen-rich conditions, (2 × 2)-based phases become more stable. This is simply due to the fact that these surfaces can adsorb one additional P_2O_7 motif per (2 × 4) surface unit before reaching saturation. At low $\Delta\mu_{In}$ (≤ -1.09 eV) and for $\Delta\mu_O \leq -2.45$ eV, P-rich, (2 × 2)-2D-based structures with low oxygen content become stable. In general, lower $\Delta\mu_O$ shifts P-rich surfaces to lower $\Delta\mu_{In}$ values. Conversely, for larger $\Delta\mu_O$, the P-rich, (2 × 2)-2D based surface

expands its region of thermodynamic stability. Furthermore, apart from the clean surface, mixed dimer-based structures are only stabilised for largely positive $\Delta\mu_{In}$ ($\geq$0.85 eV) values. This is already far in the range, where In-metal should form and therefore it seems unlikely that mixed-dimer- or $\alpha2(2 \times 4)$-based structures are observable in the presence of oxygen. This is a rather surprising finding, as experimental and computational studies on InP-based surfaces have usually focused on the mixed dimer structure and derivatives thereof.[16] In fact, the here presented results clearly show that the formation of PO_x-based motifs is the dominant mechanism on the InP(001) surface, thus determining the surface passivation in the presence of oxygen.

4 Conclusions

In conclusion, this paper re-investigated the stability of the (2×2)-2D- and $c(4 \times 4)$-based surface reconstructions in the P-rich domain *via* DFT calculations with the inclusion of van der Waals interactions. The surface reconstructions $\beta2(2 \times 4)$ and $\alpha2(2 \times 4)$ are observed for intermediate chemical potential, while for the In-rich domain, the mixed-dimer reconstruction is observed.

The introduction of oxygen changes the picture significantly. While P-rich phases strongly favour the formation of (P_xO_y) polyphosphate moieties, with P_2O_7 motifs being particularly stable, the In-rich mixed dimer phase shows a rather homogeneous distribution of oxygen on the surface. In the overall phase diagram, this results in the finding that the typically investigated mixed-dimer reconstruction and ordered derivatives thereof are unlikely to be observed in the presence of oxygen. This corroborates experimental findings,[15] where oxygen adsorption on InP in vacuum was found to turn the surface optically isotropic starting from the mixed-dimer reconstruction, but not for the P-rich, (2×2)-2D–2H surface. This is an important finding as the mixed-dimer surface has typically been considered as being the dominant surface reconstruction in the presence of oxygen, probably because this surface reconstruction is experimentally more easily accessible *via* sputtering–annealing routines. Our results now show that P-rich phases are stable over a wide range of $\Delta\mu_{In}$ (and $\Delta\mu_P$), which means that for instance in electrochemical environments, these phases can be expected to be observed, whereas ordered mixed-dimer based phases seem very unlikely.

Data availability

The data that support the findings of this study, including structure files of the most stable structures, are openly available on NOMAD at **https://doi.org/10.17172/NOMAD/2025.03.11-2**.[33]

Conflicts of interest

There are no conflicts to declare.

Acknowledgements

This work was funded by the German Research Foundation (DFG) under project number 434023472. The authors acknowledge support by the state of Baden-Württemberg through bwHPC and the German Research Foundation (DFG) through grant no INST 40/575-1 FUGG (JUSTUS 2 cluster). Part of this work was performed on the HoreKa supercomputer funded by the Ministry of Science, Research and the Arts Baden-Württemberg and by the Federal Ministry of Education and Research. We acknowledge support by the Open Access Publishing Fund of the University of Tübingen.

References

1 N. S. Lewis and D. G. Nocera, *Proc. Natl. Acad. Sci. U. S. A.*, 2006, **103**, 15729–15735.
2 J. L. Young, M. A. Steiner, H. Döscher, R. M. France, J. A. Turner and T. G. Deutsch, *Nat. Energy*, 2017, **2**, 17028.
3 H. Song, S. Luo, H. Huang, B. Deng and J. Ye, *ACS Energy Lett.*, 2022, **7**, 1043–1065.
4 E. A. Schmitt, M. Guidat, M. Nusshör, A.-L. Renz, K. Möller, M. Flieg, D. Lörch, M. Kölbach and M. M. May, *Cell Rep. Phys. Sci.*, 2023, **4**, 101606.
5 H. Gerischer, *J. Electroanal. Chem. Interf. Electrochem.*, 1983, **150**, 553–569.
6 J. Tournet, Y. Lee, S. K. Karuturi, H. H. Tan and C. Jagadish, *ACS Energy Lett.*, 2020, **5**, 611–622.
7 A. C. Nielander, M. R. Shaner, K. M. Papadantonakis, S. A. Francis and N. S. Lewis, *Energy Environ. Sci.*, 2015, **8**, 16–25.
8 A. G. Muñoz, C. Heine, H. W. Klemm, T. Hannappel, N. Szabo and H.-J. Lewerenz, *ECS Trans.*, 2011, **35**, 141–150.
9 T. Baba and M. Koma, *Jpn. J. Appl. Phys.*, 1995, **34**, 1405–1408.
10 E. Aharon-Shalom and A. Heller, *J. Electrochem. Soc.*, 1982, **129**, 2865–2866.
11 I. Vurgaftman, J. R. Meyer and L. R. Ram-Mohan, *J. Appl. Phys.*, 2001, **89**, 5815–5875.
12 C. Zhang, T. Sayer, J. Hutter and M. Sprik, *J. Phys.: Energy*, 2020, **2**, 032005.
13 M. M. May and W. Jaegermann, *Curr. Opin. Electrochem.*, 2022, **34**, 100968.
14 G. Chen, S. B. Visbeck, D. C. Law and R. F. Hicks, *J. Appl. Phys.*, 2002, **91**, 9362–9367.
15 M. M. May, H.-J. Lewerenz and T. Hannappel, *J. Phys. Chem. C*, 2014, **118**, 19032–19041.
16 I. A. Ruiz Alvarado, M. Karmo, E. Runge and W. G. Schmidt, *ACS Omega*, 2021, **6**, 6297–6304.
17 T. A. Pham, X. Zhang, B. C. Wood, D. Prendergast, S. Ptasinska and T. Ogitsu, *J. Phys. Chem. Lett.*, 2018, **9**, 194–203.
18 D. C. Moritz, I. A. Ruiz Alvarado, M. A. Zare Pour, A. Paszuk, T. Frieß, E. Runge, J. P. Hofmann, T. Hannappel, W. G. Schmidt and W. Jaegermann, *ACS Appl. Mater. Interfaces*, 2022, **14**, 47255–47261.
19 B. C. Wood, E. Schwegler, W. I. Choi and T. Ogitsu, *J. Am. Chem. Soc.*, 2013, **135**, 15774–15783.

20 B. C. Wood, E. Schwegler, W. I. Choi and T. Ogitsu, *J. Phys. Chem. C*, 2014, **118**, 1062–1070.
21 X. Zhang, T. Ogitsu, B. C. Wood, T. A. Pham and S. Ptasinska, *J. Phys. Chem. C*, 2019, **123**, 30893–30902.
22 M. M. May, H. Stange, J. Weinrich, T. Hannappel and O. Supplie, *SciPost Phys.*, 2019, **6**, 58.
23 R. Sciotto, I. A. Ruiz Alvarado and W. G. Schmidt, *Surfaces*, 2024, **7**, 79–87.
24 M. Löw, M. Guidat, J. Kim and M. M. May, *RSC Adv.*, 2022, **12**, 32756–32764.
25 H. Euchner, V. Yadav and M. M. May, *ACS Appl. Mater. Interfaces*, 2025, **17**, 8601–8609.
26 T. D. Kühne, M. Iannuzzi, M. Del Ben, V. V. Rybkin, P. Seewald, F. Stein, T. Laino, R. Z. Khaliullin, O. Schütt, F. Schiffmann, D. Golze, J. Wilhelm, S. Chulkov, M. H. Bani-Hashemian, V. Weber, U. Borštnik, M. Taillefumier, A. S. Jakobovits, A. Lazzaro, H. Pabst, T. Müller, R. Schade, M. Guidon, S. Andermatt, N. Holmberg, G. K. Schenter, A. Hehn, A. Bussy, F. Belleflamme, G. Tabacchi, A. Glöß, M. Lass, I. Bethune, C. J. Mundy, C. Plessl, M. Watkins, J. Vande Vondele, M. Krack and J. Hutter, *J. Chem. Phys.*, 2020, **152**, 194103.
27 J. P. Perdew, K. Burke and M. Ernzerhof, *Phys. Rev. Lett.*, 1996, **77**, 3865–3868.
28 J. P. Perdew, K. Burke and M. Ernzerhof, *Phys. Rev. Lett.*, 1997, **78**, 1396.
29 S. Grimme, J. Antony, S. Ehrlich and H. Krieg, *J. Chem. Phys.*, 2010, **132**, 154104.
30 M. Zorn, T. Trepk, J. T. Zettler, B. Junno, C. Meyne, K. Knorr, T. Wethkamp, M. Klein, M. S. Miller, W. Richter and L. Samuelson, *Appl. Phys. A*, 1997, **65**, 333–339.
31 B.-X. Yang and H. Hasegawa, *Jpn. J. Appl. Phys.*, 1991, **30**, 3782.
32 W. Schmidt, *Appl. Phys. A*, 2002, **75**, 89–99.
33 V. Yadav, H. Euchner and M. M. May, *NOMAD dataset: InP(001)-Ox*, 2025, DOI: **10.17172/NOMAD/2025.03.11-2**.

ChemCatChem

Research Article
doi.org/10.1002/cctc.202501347

Chemistry Europe
European Chemical Societies Publishing

www.chemcatchem.org

Surface Dynamics of Clean and Oxygenated InP(001) Surfaces in Contact with Water—Insights from Computational Spectroscopy

Vibhav Yadav,[a] Holger Euchner,[a] and Matthias M. May*[a]

Understanding the structure of semiconductor–electrolyte interfaces under operating conditions is crucial for designing electrodes in photoelectrochemistry and electrocatalysis. However, only few experimental methods exist that give real-time access to the very interface. Here, reflection anisotropy spectroscopy (RAS) is an emerging technique in the field of spectroelectrochemistry. We computationally investigate how the surface structure of clean and oxygenated InP(001) surfaces—in vacuum and in contact with water—and its evolution over time affect the optical response. Depending on the electronic structure of the respective surfaces, different species are adsorbed, resulting in changes of the anisotropy clearly visible in the spectroscopic fingerprint, while the presence of H_2O stabilizes certain configurations. Distinct fluctuations of the individual spectra are observed during the molecular dynamics trajectory. However, the resulting time-averaged spectra show a rather good agreement with the respective spectra of the reference structure for most structures. This means that—depending on the surface—the geometry-optimized structures might be suitable for comparison with experiment or not. This behavior differs from the case of metals and can be attributed to the semiconducting nature of the system. Our findings highlight the need to account for the electrochemical environment in computational RAS.

1. Introduction

The structure of electrochemical interfaces plays an important role for a range of applications, such as energy storage in batteries and hydrogen generation, but also electrocatalysis for more complex products. Both structure and potential distributions of an electrochemical interface can be altered by an applied external potential and may evolve over time, especially in the case of semiconductors, where electric fields are not as directly screened as in metals.[1] Consequently, understanding these interfacial structures and their properties is crucial for improving electrochemical device performance and stability. However, characterizing the structure of these interfaces under working, *operando* conditions at sufficient structural and temporal resolution by experimental methods remains a challenge, with no single method providing all the information necessary to fully understand a given system.[2]

Here, reflection anisotropy spectroscopy (RAS) is an emerging optical *operando* technique which offers high sensitivity for the detection of structural changes at the electrochemical interface.[3,4] For instance, RAS allows for the real-time monitoring of adsorption processes or the evolution of intermediate species under growth conditions.[5,6] The details on surface chemistry, such as the fact that P-rich GaP(001) surfaces in contact with gas-phase H_2O show surface reordering without oxidizing, can be revealed by a combination of experimental and computational RAS.[7] In electrochemical environments, RAS allows the direct correlation of spectroscopic features with electrochemical responses such as cyclic voltammograms.[8] With a temporal resolution of 10 ms provided already by commercial spectrometers, time-resolved RAS allows to study kinetics at the electrochemical interface[9] and indirectly probes potential distributions modified by the electrochemically induced formation of surface states.[10] However, deriving the structure of surfaces or interfaces from the experimental spectra alone is typically not directly possible, but requires correlation with other experimental techniques or computational spectroscopy to establish a firm relation between structure and RA spectrum.

While computational RAS of surfaces in vacuum, starting from a groundstate structure provided by density functional theory (DFT), is well-established,[11] this is not the case for the context of electrochemistry or heterogeneous catalysis. Here, similar challenges as for electronic structure modeling of electrochemical systems apply, taking into account the dynamics of the electrolyte under periodic boundary conditions in a comparatively small supercell.[4] Our recent ab initio molecular dynamics (AIMD)-based work investigated how surface dynamics can influence the RA spectra of a reconstructed Au(110) surfaces in contact with water.[12] This demonstrated that the thermally induced variability of the surface structure—even without chemical reactions—can lead to spectral differences in terms of

[a] V. Yadav, H. Euchner, M. M. May
Institute of Physical and Theoretical Chemistry, Universtiät Tübingen, Auf der Morgenstelle 15 72076, Tübingen, Germany
E-mail: matthias.may@uni-tuebingen.de

Supporting information for this article is available on the WWW under https://doi.org/10.1002/cctc.202501347

intensities, and features between the standard approach of computational spectroscopy on top of a geometry-optimized structure and a snapshot from MD at finite temperature, emphasizing the importance of including time-dependent effects for computational RAS. To what extent this holds true for a more reactive, semiconducting system, is the scope of the present work.

Indium phosphide (InP), a III-V semiconductor used in a variety of opto-electronic applications, and its related multinary compounds play an important role in highly efficient photovoltaic or photoelectrochemical solar cells as photoabsorbers or window layers.[13–15] Here, for instance, $Ga_{1-x}In_xP$ and $Al_{1-x}In_xP$ phases are typically used.[15] Tailoring the properties of these ternary compounds firstly calls for a full understanding of the underlying binary InP phase. It has been indeed shown experimentally that insights from InP can be transferred for instance to GaInP.[5,16] Also, CO_2 reduction to CO and formic acid has been demonstrated for InP photoelectrodes.[17] A fundamental understanding of the thermodynamically stable surface structures of InP, that emerge in electrochemical environments, is essential for developing effective strategies for electronic and electrochemical surface passivation, as structural and stoichiometric changes can and typically will result in the formation of recombination centers, material dissolution or corrosion.[5,15]

In this context, oxygen chemisorption and the resulting surface phases as well as their thermodynamic stability are of particular interest. In contact with oxygen, InP surfaces tend to form P_xO_y polyphosphate motifs—also as dissociative products from water adsorption—as demonstrated by a number of experimental and computational studies.[5,18–22] Some of these phosphates were experimentally found to stabilize devices under operating conditions,[13,23] highlighting the central role of oxygen for passivating surface structures. This importance of P_xO_y has recently been confirmed by the dominant occurrence of polyphosphate-terminated surface reconstructions observed for a wide range of oxygen chemical potentials in the computationally assessed phase diagram of InP(001) in contact with oxygen.[22] DFT calculations on In-rich surface reconstructions, focusing on oxygen and hydroxyl adsorption on InP surfaces, on the other hand, identify distinct bonding motifs, such as M–O–M and M–O–P bridges.[19] These are associated with specific electronic signatures, with, for instance, M–O–M bridges acting as hole traps that can contribute to charge-carrier recombination[19] and were experimentally found to form preferentially under oxygen, to a lesser extent under water exposure.[5] Similar results were found computationally by Alvarado et al.,[24,25] again focusing on the mixed-dimer reconstruction as the starting point.[24]

The focus of many experimental and computational studies on (2 × 4) mixed-dimer based reconstructions originates in the boundary condition that this surface is experimentally most straightforward to prepare by epitaxial growth and especially by vacuum-based sputter-annealing routines.[5,20] Recent experimental work using electrochemical RAS did, however, show that highly ordered, reconstructed InP(001) surfaces can be prepared directly in the electrolyte under suitable conditions and that these are not necessarily based on the mixed-dimer reconstruction.[8,10,26] When moving toward a realistic DFT-based representation of electrochemical interfaces, the presence of an electrolyte, which is typically aqueous, has to be considered. Consequently, for correctly predicting and designing durable, passivated, and catalytically active materials, it is important to understand the resulting solid–liquid interface at ambient temperatures as well as starting from realistic surface configurations, where both parameters typically lead to qualitatively different interactions with water.[5,27]

While pristine InP(001) surfaces exhibit high barriers for gas-phase H_2O dissociation, the presence of a submonolayer native oxide was predicted to significantly alter this, leading to strongly exothermic, barrier-less H_2O dissociation via strong, low-barrier H-bonds and rapid proton hopping via a Grotthus-type mechanism at the solid–liquid interface.[28] DFT calculations suggest that H_2O adsorption on In-rich InP(001) surfaces is molecular at first, but becomes more dissociative with coverage, stabilizing hydroxyl-anchored H_2O films that reduce the reaction barrier.[25] While a significant body of literature already exists for InP in contact with water, an understanding of structures of this reactive semiconductor under realistic electrochemical conditions is only slowly starting to emerge. Here, electrochemical RAS offers the unique opportunity to prepare and study highly ordered semiconductor-electrolyte interfaces under static and transient conditions, but this requires to first establish robust computational approaches for this environment.

In this study, we computationally determine the optical anisotropy of InP(001) surfaces in contact with oxygen for several P-rich oxygenated surfaces that have been found stable in the surface phase diagram with respect to oxygen exposure. In addition, we specifically investigate the impact of aqueous environments by adding several water layers on top of these oxygenated surfaces. By computing RA spectra for different snapshots along AIMD trajectories, we examine how the structural dynamics of clean and oxygen-terminated surfaces as well as the presence of H_2O affect the electronic structure and the resulting optical anisotropy. Our results show that the optical response is less strongly affected by thermal fluctuations as expected from earlier findings on metal surfaces,[12] which is an inherent consequence of the semiconducting nature of InP. Whether interfacial H_2O results in adsorption or decomposition depends on the respective surface reconstruction. In some cases, this is found to result in a restructuring of the surface, whereas for others, the H_2O stabilizes the present surface structure. These qualitatively different responses of the surface reconstructions highlight the necessity for considering AIMD trajectories for computational RAS at semiconductor electrodes under realistic conditions.

2. Methods

In RAS, linearly polarized light at nearnormal incidence is employed to study a surface or interface. The reflectivity difference along two orthogonal crystal directions r_x and r_y—for cubic (001) surfaces typically the [$\bar{1}$10] and [110] directions—in the surface plane is measured and analyzed as a function of the incoming photon energy. This observed reflectivity difference, Δr, is normalized by the total reflectivity, r, leading to the

following expression:[3]

$$\mathrm{RAS} := \frac{\Delta r}{r} = 2\frac{r_{[\bar{1}10]} - r_{[110]}}{r_{[\bar{1}10]} + r_{[110]}};\ r \in \mathbb{C}. \quad (1)$$

In the case of optically isotropic bulk materials, the signal is generated solely by the optical anisotropy of the surface region and also the bulk electrolyte (water) does not contribute to the signal.[7] Consequently, RAS can monitor surface modifications that perturb the surface's symmetry or modify the optical properties of the very electrochemical interface. RAS is sensitive to the anisotropy of the dielectric function and the electronic structure at the surface/interface. While the direct interpretation of RA spectra is difficult, pronounced minima or maxima can often be correlated to specific features of the band structure—such as surface states—and transitions between the corresponding states.[3] Making use of the relation $\Re(\frac{\Delta r}{r}) \approx \frac{1}{2}\frac{\Delta R}{R}$, valid for $\Delta r << r$, allows to express the RA signal with respect to the reflectance R. The latter one can then directly be related to the anisotropy of the surface dielectric function via the following equation:[29,30]

$$\frac{\Delta R}{R} = \frac{4\pi d}{\lambda}[A\Delta\epsilon_s'' - B\Delta\epsilon_s'], \quad (2)$$

with $\Delta\epsilon_s''$ and $\Delta\epsilon_s'$ corresponding to the difference in real and imaginary parts of the surface dielectric function with respect to the two orthogonal directions, d the layer thickness, and λ the photon wavelength. Finally, A and B are related to the complex bulk dielectric function, ϵ_b, with $A = \Re\left[\frac{1}{\epsilon_b - 1}\right]$ and $B = -\Im\left[\frac{1}{\epsilon_b - 1}\right]$. The quantities in this expression can now be obtained via electronic structure calculations as outlined in the following paragraph.

2.1. Computational Spectroscopy

Different clean and oxygenated InP(001) surface reconstructions and their interaction with H_2O were modeled using periodic DFT as implemented in the CP2K code package.[31] For all calculations, the Gaussian-and-plane-waves (GPW) approach was employed, using a computational setup that has successfully been applied in the past.[22,26] A TZV2P basis-set was used in combination with nonlocal norm conserving GTH-PBE pseudopotentials for describing the electron-core interaction. Furthermore, a carefully converged plane-wave cutoff of 400 Ry and a relative cutoff of 60 Ry were selected. Exchange and correlation were described by the generalized gradient approximation in the formulation of Perdew, Burke, and Ernzerhof (PBE).[32,33] Additionally, van-der-Waals interactions were accounted for by the Grimme-D3 correction.[34] For efficient optimization of the electronic structure, the orbital transformation (OT) method[35] was applied.

The oxidized surfaces, based on (2×2) and (2×4) reconstructions, were modeled via asymmetric slabs, comprising 6 In and 6 P layers. To mitigate interactions between periodic images, a vacuum region of approximately 20 Å was included along the surface normal. During geometry optimization, the bottom 3 In- and 2 P-layers of the slab were fixed. To account for the polarity of the InP surface, the bottom In-layer was passivated with pseudo-hydrogen atoms ($Z = 1.25$). In addition to the solid–vacuum interface, the impact of H_2O and the resulting solid–liquid interface was also studied. For this purpose, 7 layers of H_2O were included, corresponding to 58 and 116 H_2O molecules for the (2×2) and $(2, \times 4)$ surface supercells, respectively. The dimensions of the investigated slab model ensure converged surface energies and are in agreement with earlier studies on similar systems.[22,25,26,36] In principle, the simulation of more realistic electrochemical scenarios—including solvated ions—is highly desirable. This does, however, also call for larger system sizes. Therefore, the current study is restricted to the presence of water, thus describing the dilute electrolyte limit.

To investigate the impact of surface dynamics, AIMD simulations were performed in a canonical ensemble at 300 K, controlled by an Adaptive-Langevin thermostat. The corresponding trajectories were run for at least 15 ps with a time-step of 0.5 fs. After an equilibration time of no less than 5 ps, snapshots were extracted every 500 fs, allowing for the subsequent determination of the optical anisotropy. The corresponding RA spectra were then determined via the Yambo code.[37,38] Yambo requires ground-state wave functions from a plane wave DFT code, which were provided via Quantum espresso(QE).[39] As in previous DFT calculations, the PBE exchange-correlation functional was employed alongside optimized norm-conserving Vanderbilt (ONCV) pseudopotentials. A plane-wave cutoff of 60 Ry, combined with a $4 \times 4 \times 1$ and $4 \times 2 \times 1$ k-point mesh, chosen according to the surface unit cell size, was applied.

All RA spectra were obtained in the independent particle random phase approximation without local field effects (IP-RPA), using the optimized RAS module, as implemented in the public development branch of Yambo (version 5.0.1).[12] A real-space cutoff was applied such that only the topmost four layers of the InP slab contributed to the RA spectra, while the bulk dielectric function of InP was extracted from experimental data.[40] To account for the underestimation of the band gap in the underlying DFT calculations, we applied an empirical scissors operator correction to the PBE-derived band structures. A suitable scissor operator was determined for each of the considered systems, relying on hybrid DFT, PBE0-based reference calculations[41,42] and a targeted bulk band gap of 1.34 eV. For this purpose, mid-trajectory snapshots of the AIMD simulations were chosen to determine the respective scissors operator (see Figure S1). While a fully hybrid DFT-MD trajectory with PBE0 would omit the necessity of the scissors operator, it would also significantly increase the computational costs, reducing the achievable trajectory length, and snapshotting density. The approach chosen here is therefore a balance between single-point accuracy and sampling over time.

3. Results and Discussion

The starting point of our work is the previously determined phase diagram of InP(001) surfaces as a function of the In and O chemical potentials. This shows a predominant occurrence of P-rich $\beta 2(2 \times 4)$- and (2×2)-based surface terminations, in particular for intermediate values of μ_{In}, whereas the fre-

quently investigated In-rich, mixed-dimer surface was found to be rather unlikely under such conditions.[22] Based on the respective regions of stability, we selected representative surface reconstructions to investigate their dynamics and the resulting changes in the optical response. For this purpose, the following phases were investigated: The $\beta2(2\times4)$ structure, a stepped P-rich surface with three P-dimers per surface unit cell; the $\beta2(2\times4)(P_2O_7)_3$ structure, in which each of the three P-dimers of the clean surface is saturated with oxygen, resulting in P_2O_7 polyphosphate-type motifs; the $(2\times2)(P_2O_7)_2$ reconstruction, a P-terminated, (2×2)-based structure in which each of the two P-dimers transforms to a fully saturated P_2O_7-type polyphosphate; and finally the $(2\times2)(P_2O_6)_2$ phase, which resembles the previous structure, however, with the P-dimers transformed to P_2O_6 type units, hence corresponding to a slightly reduced oxygen coverage.

In general, the oxygen-rich structures feature polyphosphate motifs that saturate the surface P-dimers and are often accompanied by additional In-O-In bridges in the subsurface. In addition to the systems in vacuum, the contact with H_2O was studied, also evaluating if the presence of water molecules has a stabilizing impact or not. In the following, the different surface reconstructions and their temporal evolution throughout AIMD simulations are discussed with emphasis on modifications in structure and optical response. Individual RA spectra, obtained from AIMD snapshots are combined to color plots, which display the spectral evolution over time. These plots are compared to the time-averaged RA spectra and the corresponding reference state—a geometry-optimized structure—for each surface reconstruction. This analysis aims to uncover how dynamic surface fluctuations and structural motifs influence the optical anisotropy.

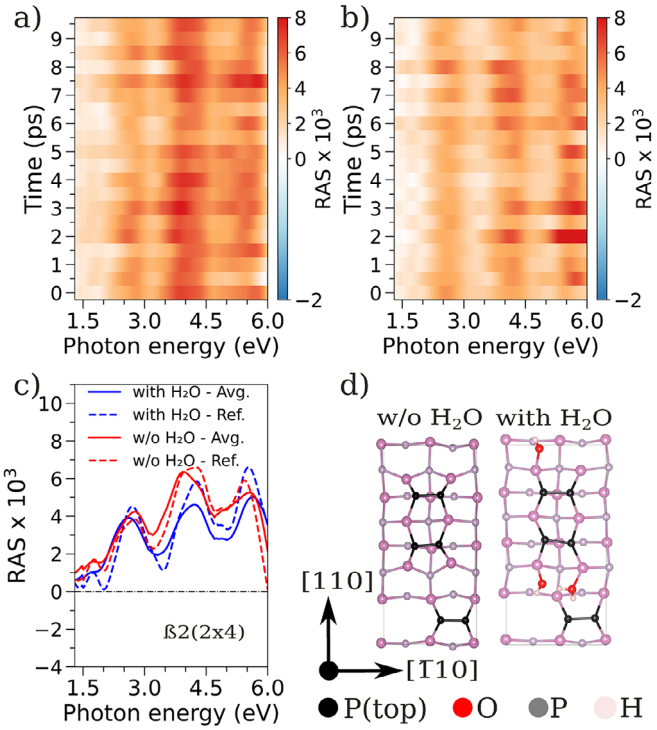

Figure 1. Evolution of RAS during the MD trajectory of the $\beta2(2\times4)$ surface. (a) and (b) show the time-resolved RAS color plots for the $\beta2(2\times4)$ surface without and with H_2O, respectively. (c) presents the time-averaged and reference (ground state) RA spectra for both the with H_2O (blue lines) and without H_2O (red lines) cases. (d) shows the representative AIMD snapshots of the corresponding configurations with the top and underlying P-atoms indicated in black and grey. In, O, and H atoms are indicated by pink, red, and cream, respectively. The color scheme provided here is also applied in subsequent figures.

3.1. $\beta2(2\times4)$

Under oxygen-poor conditions and for intermediate indium chemical potentials, the plain $\beta2(2\times4)$ reconstruction is found to be stable. This well-known phase corresponds to a stepped surface and is characterized by the presence of three P-dimers. Two of these dimers are located on the upper terrace, whereas the third one lies on the lower terrace. In contact with H_2O, the structural relaxation results in the adsorption of two hydroxyl groups that bind to In atoms at the edges of the upper terrace (see Figure 1d).

In the absence of H_2O, three pronounced peaks at 2.8, 3.9, and 5.5 eV as well as a small feature at 1.7 eV are observed in the time-averaged RA spectrum, obtained from the spectra corresponding to the different AIMD snapshots (see Figure 1c). The main features of the average RAS are also present during the time evolution of the system, in particular, the most intense peak at 3.9 eV is clearly visible throughout the whole color plot (see Figure 1a). An in-depth analysis of the individual spectra shows that their overall appearance does not change significantly. However, fluctuations in intensity as well as changes in the peak shape, including the evolution of shoulders and peak splitting are observed for the four main features (see Figure S2). The spectrum of the reference structure shows the same features with slightly different peak shape and intensity, but does not differ significantly from the average RAS, as can be seen in Figure 1c. In agreement with the small observed RAS fluctuations, limited structural distortions are observed along the AIMD trajectory, as can, for instance, be seen from the rather narrow radial distribution function (RDF) of the In-P bond length in the top layer (see Figure S10). Moreover, the RDF of the reference structure, convoluted with a gaussian, and that one of the AIMD trajectory are very similar. Consequently, the fluctuations along the AIMD trajectory can be interpreted as vibrational motion around the equilibrium structure.

For the system in contact with H_2O, the resulting average RA spectrum remains similar to the water-free case, with the three main peaks slightly shifted to 2.7, 4.2, and 5.7 eV, respectively. Additionally, the color plot illustrates rather small spectral deviations over time, with the three maxima clearly visible at each time step (see Figure 1b). A notable spectral characteristic that is observed in several snapshots is an additional shoulder at around 5 eV (see Figure S3). Furthermore, the RA spectrum of the reference structure is again not largely deviating from the time-averaged spectrum. Only the main features are slightly more pronounced for the high-energy peaks, as can be inferred from Figure 1c. For the case of the water-free surface, this agrees well with the fact that no significant atomic displacement of the

surface atoms are observed, which is again visible from a similar In—P bond length distribution in the top layer along the AIMD trajectory and for the reference structure (see Figure S10). Moreover, the differences in RDF between the cases with and without water are rather small and only start in beyond the second nearest neighbor shell.

Finally, an interesting effect is observed in course of the AIMD simulation. The OH groups that are bound to the In atoms at the terraces are found to dynamically switch positions. This happens through the interaction with a H_2O molecule in the vicinity of the neighboring In atom. A proton from the H_2O molecule migrates to the adsorbed OH group, leaving an OH behind which then adsorbs on the neighboring In. While these configurations are changing back and forth, the dynamic equilibrium persists along the whole trajectory (see for instance, Figure 1d), not leaving a clear spectral signature in the RA signal. This observation is similar to the Grotthus- and Zundel-type mechanisms observed by Wood et al.,[28,43] but for different pre-oxygenated and pre-hydroxylated structures. This means that the rapid and long-range hydrogen transport enabled hereby[28,43] appears to be a rather generic feature of InP(001) surfaces in contact with water and not unique for very specific surface structures.

In comparison, the spectra with and without H_2O show the same main features, indicating that OH adsorption and the resulting dynamic equilibrium have a minor impact on the electronic structure of the surface and hence the RA signal.

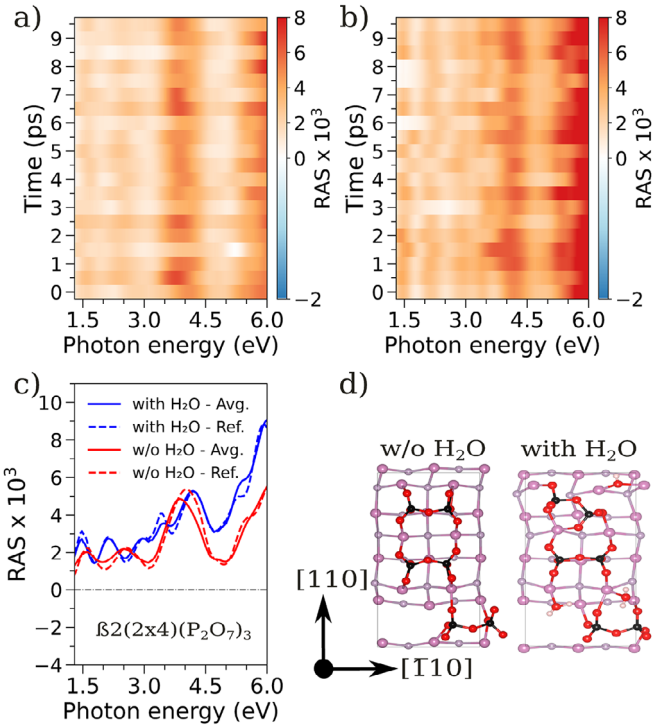

Figure 2. Evolution of RAS during the MD trajectory of the $\beta2(2 \times 4)(P_2O_7)_3$ surface. (a) and (b) show the time-resolved RAS color plot for the $\beta2(P_2O_7)_3$ surface without and with H_2O. (c) presents the time-averaged and reference structure RA spectra for the cases with H_2O (blue lines) and without H_2O (red lines). (d) shows representative MD snapshots of the corresponding configurations.

3.2. $\beta2(2 \times 4)(P_2O_7)_3$

The $\beta2(P_2O_7)_3$ reconstruction is observed under more oxygen-rich conditions and is characterized through the formation of three particularly stable P_2O_7 polyphosphate motifs. In the case of the solid–vacuum interface, the time-averaged RA spectrum shows two pronounced peaks at 3.8 eV and toward 6 eV. In addition, two small peaks at 1.6 and 2.5 eV are observed. In comparison to the RA spectrum of the relaxed reference structure, even less significant differences as in the previous cases are observed. The spectra match almost perfectly, with only the peak at 3.8 eV showing a tiny shift and a slightly increased intensity. When the time evolution of the RA signal is considered, the main features remain unchanged and the two main peaks with their adjacent minima are clearly visible for the different time steps depicted in the color plot (see Figure 2a). Even the two low-intensity peaks persist for the whole time series (see also Figure S4). The individual RA spectra along the AIMD trajectory undergo small fluctuations, which again can be understood as signature of thermal vibrations. Here, it has to be pointed out that the P_2O_7 motifs are found to be extremely stable, which is also evident from the small P—O bond length variation that is observed in the RDF (see Figure S11). This structural stability is also reflected in a low temporal variability of the RA spectra.

For the system in contact with H_2O, up to three H_2O molecules adsorb on the edge of the upper In terrace, whereas a hydroxyl group is adsorbed between two In edge sites on the other side of the terrace (see Figure 2d). The resulting In–OH–In configuration results in a tilting of the adjacent P_2O_7 unit. Surprisingly, this configuration is observed throughout the whole AIMD trajectory with only small displacements of the surface atoms. The corresponding time-averaged RA spectrum is depicted in Figure 2c and shows, for higher energies, a similar spectrum as the water-free case with peaks at 4.2 and toward 6 eV. In addition, a peak at 3.4 eV and three low-energy peaks of small intensity are visible at 1.5, 2.1, and 3.0 eV, respectively. Interestingly, the intensity of the averaged RA spectrum is slightly increased as compared to the water-free case, which may indicate an H_2O-stabilized, less dynamic surface. While the four maxima and the intermediate minima can be observed for the color plot along the AIMD trajectory in Figure 2b, a more detailed investigation of the individual snapshots reveals small fluctuation of the low-energy features and the shoulder at 5.2 eV for several points in time (see Figure S5). Also for this scenario, comparing the average RA spectrum to the spectrum of the reference structure shows only small deviations. The spectra almost perfectly match, apart from a tiny intensity variations of the peaks and the more pronounced shoulder at 5.2 eV. These small spectral changes are in line with the observed stable P_2O_7 units (see Figure S11) and hence thermal fluctuations around the lowest-energy structure.

Again, the spectra in presence and absence of H_2O are qualitatively similar with quite small fluctuations during the investigated time period, emphasizing the stability of the P_2O_7 units for both scenarios, which is also confirmed by the RDF of the P—O bonds in the top layer (see Figure S11). The In—P and

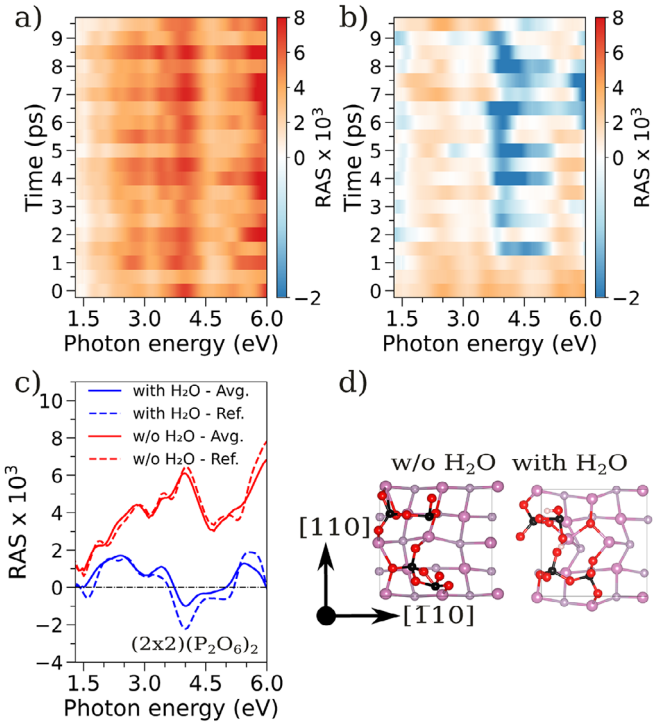

Figure 3. Evolution of RAS during the MD trajectory of the $(2 \times 2)(P_2O_6)_2$ surface. (a) and (b) show the time-resolved RAS color plots for the $(2 \times 2)(P_2O_6)_2$ surface without and with H_2O. (c) presents the time-averaged and reference structure RA spectra for the cases with H_2O (blue lines) and without H_2O (red lines). (d) shows representative MD snapshots of the corresponding configurations.

In—O bonds show slightly differing distributions in the presence of water, which, however, results from the additional In–OH–In configurations, thus not pointing to a significantly enhanced surface dynamics.

3.3. (2 × 2)$(P_2O_6)_2$

For further increasing oxygen chemical potential, the 2 × 2-based surfaces become stable, which is due to their ability of accepting more oxygen. The $(2 \times 2)(P_2O_6)_2$ surface is characterized by the formation of two different P_2O_6 polyphosphate motifs, which in the presence of H_2O adsorb additional H/OH.

In the absence of H_2O, the time-averaged RA spectrum of the $(2 \times 2)(P_2O_6)_2$ phase remains positive over the whole energy range and displays rather distinct (double-)peaks at about 2.8, 4.0, and toward 6.0 eV, as can be inferred from Figure 3c. The RA spectrum corresponding to the reference structure does not deviate significantly from the average RAS. In fact, the observable differences are particular small for this case. Consequently, when the time evolution of the spectra is considered, rather small fluctuations are observed. In particular, the maxima at around 4.0 and 6.0 eV, as well as the minimum between them persist throughout time (see Figure 3a). These findings align well with the small fluctuations of the In—O bonds with respect to the reference structure as well as with the narrow bond length distribution for the P—O bonds (see Figure S12), which again indicates the rigidity of the P_xO_y motifs. A more detailed investigation of the individual spectra reveals changes in intensity and shape of the main peaks, including the occurrence of additional features such as shoulders or peak splitting (see Figure S6).

Unlike for the first two surfaces, the presence of H_2O significantly alters spectra and structure. The initially present P_2O_6 units transform to P_2O_7H- and $P_2O_6H_2$-like motifs. This happens via the migration of H^+ and OH^- ions from the bulk H_2O to the respective polyphosphates, causing a significant structural rearrangement. Moreover, an additional oxygen is directly adsorbed on the surface, forming an In–O–In bridge configuration. As a consequence of these structural changes, the time-averaged RA spectrum differs significantly from the water-free case. While the average spectrum shows positive peaks a around 2.4, 3.4, and 5.4 eV, a negative feature with its largest intensity at about 4.0 eV is observed as well (see Figure 3c). Furthermore, the overall intensity of the spectrum is largely reduced. This may indicate a more isotropic surface, potentially due to H_2O-induced distortions.

Surprisingly, also for this case, the reference state spectrum is still quite close to the average RAS. This is due to the negative anisotropy around 4 eV persisting over most of the considered trajectory time, i.e., between 1.5 and 9.0 ps. The two spectrally different domains can be distinguished in the color plot depicted in Figure 3b. The spectra observed in the first ps are clearly different in comparison to the rest of the time series. In particular, the negative anisotropy near 4 eV is clearly absent for these points in time and also weaker toward the end of trajectory, as can also be seen in the individual spectra (Figure S7). Interestingly, these spectral differences can be tied to structural changes captured during the AIMD trajectory. Notably, around the 1 ps mark, the adsorbed O atom (Figure 3d), moves from an In_2O configuration to an In_3O environment, which remains stable afterwards. This interfacial rearrangement induces substantial in-plane motion, which, together with the change in bonding, seems to be at the origin of the altered RA fingerprint. Hence, the above-discussed results reveal that in the absence of H_2O the $(2 \times 2)(P_2O_6)_2$ surface maintains a stable optical response characterized by positive anisotropies that are only slightly fluctuating over time. In contrast, the presence of interfacial H_2O induces significant structural and chemical transformations, such as oxygen adsorption and hydroxylation. This leads to stronger fluctuations of the RA spectra over time and consequently a damping of the averaged RAS features. Such a behavior would be clearly observable by experimental RAS with picosecond time-resolution. Moreover, these structural changes are also visible in the RDF for the In—O and In—P bonds. In particular, the In—P bonds are shifted towards larger bond length in the presence of water and significantly differ from the water-free case (see Figure S12).

3.4. (2 × 2)$(P_2O_7)_2$

Finally, the oxygen-rich $(2\times2)(P_2O_7)_2$ surface has been investigated. This surface is characterized by the formation of two distinct P_2O_7 motifs on top of a flat In-layer. These polyphos-

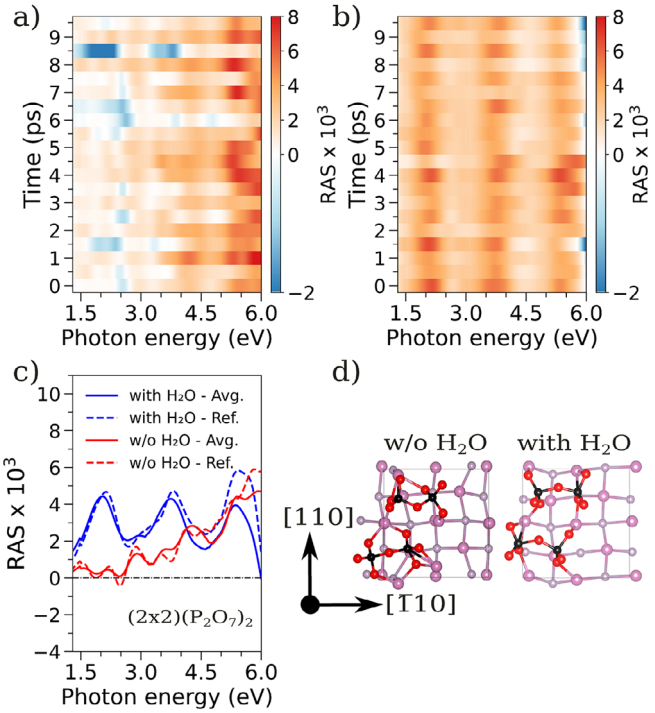

Figure 4. Evolution of RAS during the MD trajectory of the $(2\times2)(P_2O_7)_2$ surface. (a) and (b) show the time-resolved RAS color plots for the $(2\times2)(P_2O_7)_2$ surface without and with H_2O. (c) presents the time-averaged and reference structure RA spectra for the cases with H_2O (blue lines) and without H_2O (red lines). (d) shows representative MD snapshots of the corresponding configurations.

phate units are also observed in the presence of H_2O (see Figure 4d).

For the system in vacuum, the time-averaged RA spectrum shows a strong feature at ~ 5.3 eV (see Figure 4c). An additional, slightly pronounced peak is observed at about 4.2 eV, while several weak features are visible at lower energies. Over time, the spectral response evolves significantly, as can be inferred from the color plots in Figure 4a. The most prominent peak at ~ 5.3 eV is visible for most parts of the color plot and the corresponding individual spectra (see Figure S8). Yet, there are several snapshots, where this peak is largely reduced, going along with a strongly damped RA signal (e.g., at 6.0 and 8.5 ps). Moreover, the rather weak signal below about 3.5 eV is fluctuating between negative and positive intensities throughout time as can also be inferred from the individual spectra. These fluctuations occur on rather short timescales, thus suggesting the presence of transient surface configurations. This correlates with the fact that pronounced structural distortions are observed in the AIMD trajectory, including significant displacements of In atoms in the top most In layer, which can also be inferred from the slightly broadened RDF of the In—O bonds along the trajectory (see Figure S13). Interestingly, the P_2O_7 motifs persist throughout the AIMD trajectory, again resulting in a narrow P—O bond length distribution (see Figure S13); however, they get shifted with respect to each other, which seems to cause the discussed In displacements. Nevertheless, the time-averaged RA spectrum departs only slightly from the reference state spectrum. In general, the induced structural distortions seem to render the structure more isotropic, thus reducing the overall RA signal.

Finally, in aqueous environment, we observe the opposite behavior compared to the $(2\times2)(P_2O_6)_2$ structure. The P_2O_7 motifs and the underlying In layer remain largely unaltered along the AIMD trajectory. This results in three pronounced peaks of roughly equal intensity in the average RA spectrum, located at 2.1, 3.7, and 5.3 eV, respectively, as depicted in Figure 4c. The reference-state spectrum again matches closely the average RAS and contains the same features, only showing increased intensity for the high-energy peak. The time-resolved RA spectra and the corresponding color plots show the presence of the three characteristic peaks in each of the individual snapshots, however, with changing intensity (see Figure 4b). A detailed analysis of the individual spectra reveals the appearance of small shoulders at roughly 3 eV for most snapshots, which is also slightly visible for the average spectrum (see also Figure S9). In contrast to the water-free case, the P_2O_7 motifs show no significant motion with respect to each other, which also results in smaller displacements of the In atoms in the layer below and hence a slightly narrowed In—O bond length distribution as compared to the water-free case (see Figure S13). These small displacements can, as for some of the earlier discussed cases, be understood as thermal vibrations and do not correspond to structural distortions, in contrast to the water-free scenario.

The aforementioned results indicate a stabilizing impact of H_2O on the surface, thus preserving the optical anisotropy over time. In contrast, under vacuum conditions, enhanced surface dynamics leads to a broader distribution of transient states, which directly affect the RAS signal and result in larger fluctuations of the optical anisotropy.

4. Conclusion

In this work, we explored the impact of structural dynamics along AIMD trajectories on the optical anisotropy of different InP(001)-based surface reconstructions. We find Zundel, shared-proton structures which enable Grotthus-type, long-range hydrogen transport[43] for additional structures than previously reported. This suggests that such an on-surface hydrogen transport is a comparatively generic feature of InP(001) surfaces and as a consequence potentially plays an important role in their function in applications of (photo)electrocatalysis. If this is a feature of In, independent of the vicinity to phosphorous, such mechanisms might also play a role in GaIn-based, liquid-metal electrocatalysis.[44]

Due to the dynamical structural changes of the surface over the course of the MD trajectory, the corresponding RA spectra fluctuate around the average RA spectrum. For most cases, these fluctuations and the differences to the RA spectrum of the respective reference structure are much smaller than for the recently investigated case of Au(110), where a significant reduction of the average RAS was observed.[12] This indeed means that for (electro)chemically stable surfaces of InP(001), RAS derived from geometry-optimized surfaces represent as a reasonable

starting point for comparison to experimental spectra, which can be explained by the underlying electronic structure of the semiconductor. While for metals such as gold, where slight structural changes result in the population of different electronic states, the presence of a band gap makes it difficult for electrons to populate previously unoccupied states. For semiconductors (and insulators) this means that structural changes may result in a modification of the electronic states, however, the character of the occupied states will still remain similar, whereas for metals, states with completely different characteristics may become populated. This in turn will result in stronger changes of the RA signal for the case of metals. In principle, this also means that the observation of strong changes in the RA spectrum of a semiconductor can be an indicator of unoccupied surface states close to the valence band maximum.

This does, however, not apply for the structurally less rigid surface phases, here the $(2 \times 2)(P_2O_6)_2$ and $(2 \times 2)(P_2O_7)_2$ phases of InP(001). In these cases, structural motifs and species change over the course of the MD trajectory for the case of water or vacuum. While H_2O exhibits a de-stabilizing effect on the $(2 \times 2)(P_2O_6)_2$ surface, the opposite is true for the $(2 \times 2)(P_2O_7)_2$ surface. As a consequence, the meaningfulness of computational RA spectra of geometry-optimized structures is of limited validity for such more dynamic surfaces. This demonstrates that the use of molecular dynamic trajectories is also indispensable for computational RA spectroscopy at semiconductor–electrolyte interfaces. While the general approach for computational RA spectroscopy allows quantitative comparison between experiment and DFT-based model in vacuum or gas-phase environment,[7] this is only emerging for the case of solid–liquid interfaces. Due to the complexity of electrochemical systems—applied potentials, structural complexity, structural dynamics over time—the direct comparison of experimental and computational spectra remains challenging at present. By addressing the structural dynamics of the semiconductor–electrolyte interface as in principle observable by ultrafast RA spectroscopy on short time domains, this work is a first step to enable this in the future.

Acknowledgments

This work was funded by the German Research Foundation (DFG) under project number 434023472 and the German Bundesministerium für Bildung and Forschung (BMBF), project number 01LS2103A. The authors acknowledge support by the state of Baden-Württemberg through bwHPC and the German Research Foundation (DFG) through grant no INST 40/575-1 FUGG (JUSTUS 2 cluster). Part of this work was performed on the HoreKa supercomputer funded by the Ministry of Science, Research and the Arts Baden-Württemberg and by the Federal Ministry of Education and Research. The authors acknowledge support by the Open Access Publishing Fund of the University of Tübingen.

Open access funding enabled and organized by Projekt DEAL.

Conflict of Interests

There are no conflicts of interest to declare.

Data Availability Statement

The molecular dynamics trajectories that support the findings of this study are openly available on Zenodo at https://doi.org/10.5281/zenodo.17816635.[45]

Keywords: Density functional theory · Electrochemical interfaces · Molecular dynamics · Semiconductors · Spectroelectrochemistry

References

[1] M. M. May, W. Jaegermann, *Curr. Opin. Electrochem.* **2022**, *34*, 100968.
[2] D. V. Esposito, J. B. Baxter, J. John, N. S. Lewis, T. P. Moffat, T. Ogitsu, G. D. O'Neil, T. A. Pham, A. A. Talin, J. M. Velazquez, B. C. Wood, *Energy Environ. Sci.* **2015**, *8*, 2863.
[3] P. Weightman, D. S. Martin, R. J. Cole, T. Farrell, *Rep. Prog. Phys.* **2005**, *68*, 1251.
[4] M. Guidat, M. Löw, M. Kölbach, J. Kim, M. M. May, *ChemElectroChem* **2023**, *10*, 8.
[5] M. M. May, H.-J. Lewerenz, T. Hannappel, *J. Phys. Chem. C* **2014**, *118*, 19032.
[6] J. Ortega-Gallegos, L. Guevara-Macías, A. Ariza-Flores, R. Castro-García, L. Lastras-Martínez, R. Balderas-Navarro, R. López-Estopier, A. Lastras-Martínez, *Appl. Surf. Sci.* **2018**, *439*, 963.
[7] M. M. May, M. Sprik, *New J. Phys.* **2018**, *20*, 033031.
[8] M. Löw, M. Guidat, J. Kim, M. M. May, *RSC Adv.* **2022**, *12*, 32756.
[9] S. Vazquez-Miranda, V. Solokha, R. E. Balderas-Navarro, K. Hingerl, C. Cobet, *J. Phys. Chem. C* **2020**, *124*, 5204.
[10] M. Flieg, M. Guidat, M. M. May, *Phys. Rev. Lett*, **2025**, *135*, *in print*. https://doi.org/10.1103/7vfj-hl9f.
[11] W. G. Schmidt, *Phys. Status Solidi B Basic Res.* **2005**, *242*, 2751.
[12] J. Leist, J. Kim, H. Euchner, M. M. May, *J. Phys.: Condens. Matter* **2024**, *36*, 185002.
[13] A. Heller, B. Miller, H. J. Lewerenz, K. J. Bachmann, *JACS* **1980**, *102*, 6555.
[14] M. Feifel, D. Lackner, J. Ohlmann, J. Benick, M. Hermle, F. Dimroth, *Solar RRL* **2019**, *3*, 1900313.
[15] E. A. Schmitt, M. Guidat, M. Nusshör, A.-L. Renz, K. Möller, M. Flieg, D. Lörch, M. Kölbach, M. M. May, *Cell Rep. Phys. Sci.* **2023**, *4*, 101606.
[16] J. L. Young, H. Döscher, J. A. Turner, T. G. Deutsch, *J. Phys. Chem. C* **2016**, *120*, 4418.
[17] S. Kaneco, H. Katsumata, T. Suzuki, K. Ohta, *Chem. Eng. J.* **2006**, *116*, 227.
[18] H.-J. Lewerenz, K. Schulte, *Electrochim. Acta* **2002**, *47*, 2639.
[19] B. C. Wood, T. Ogitsu, E. Schwegler, *J. Chem. Phys.* **2012**, *136*.
[20] X. Zhang, T. Ogitsu, B. C. Wood, T. A. Pham, S. Ptasinska, *J. Phys. Chem. C* **2019**, *123*, 30893.
[21] X. Zhang, T. A. Pham, T. Ogitsu, B. C. Wood, S. Ptasinska, *J. Phys. Chem. C* **2020**, *124*, 3196.
[22] V. Yadav, H. Euchner, M. M. May, *RSC Adv.* **2025**, *15*, 8464.
[23] M. M. May, H.-J. Lewerenz, D. Lackner, F. Dimroth, T. Hannappel, *Nat. Commun.* **2015**, *6*, 8286.
[24] I. A. Ruiz Alvarado, M. Karmo, E. Runge, W. G. Schmidt, *ACS Omega* **2021**, *6*, 6297.
[25] R. Alvarado, I. Azahel, W. G. Schmidt, *ACS Omega* **2022**, *7*, 19355.
[26] H. Euchner, V. Yadav, M. M. May, *ACS Appl. Mater. Interfaces* **2025**, *17*, 8601.
[27] O. Henrion, A. Klein, W. Jaegermann, *Surf. Sci.* **2000**, *457*, L337.
[28] B. C. Wood, E. Schwegler, W. I. Choi, T. Ogitsu, *J. Phys. Chem. C* **2014**, *118*, 1062.
[29] C. Hogan, O. Pulci, P. Gori, F. Bechstedt, D. S. Martin, E. E. Barritt, A. Curcella, G. Prevot, Y. Borensztein, *Phys. Rev. B* **2018**, *97*, 195407.
[30] J. McIntyre, D. Aspnes, *Surf. Sci.* **1971**, *24*, 417.

[31] T. D. Kühne, M. Iannuzzi, M. Del Ben, V. V. Rybkin, P. Seewald, F. Stein, T. Laino, R. Z. Khaliullin, O. Schütt, F. Schiffmann, D. Golze, J. Wilhelm, S. Chulkov, M. H. Bani-Hashemian, V. Weber, U. Borštnik, M. Taillefumier, A. S. Jakobovits, A. Lazzaro, H. Pabst, T. Müller, R. Schade, M. Guidon, S. Andermatt, N. Holmberg, G. K. Schenter, A. Hehn, A. Bussy, F. Belleflamme, G. Tabacchi, et al., *J. Chem. Phys.* **2020**, *152*.
[32] J. P. Perdew, K. Burke, M. Ernzerhof, *Phys. Rev. Lett.* **1996**, *77*, 3865.
[33] J. P. Perdew, K. Burke, M. Ernzerhof, *Phys. Rev. Lett.* **1997**, *78*, 1396.
[34] S. Grimme, J. Antony, S. Ehrlich, H. Krieg, *J. Chem. Phys.* **2010**, *132*.
[35] J. VandeVondele, J. Hutter, *J. Chem. Phys.* **2003**, *118*, 4365.
[36] W. G. Schmidt, *Appl. Phys. A* **2002**, *75*, 89.
[37] A. Marini, C. Hogan, M. Grüning, D. Varsano, *Comput. Phys. Commun.* **2009**, *180*, 1392.
[38] D. Sangalli, A. Ferretti, H. Miranda, C. Attaccalite, I. Marri, E. Cannuccia, P. Melo, M. Marsili, F. Paleari, A. Marrazzo, G. Prandini, P. Bonfà, M. O. Atambo, F. Affinito, M. Palummo, A. Molina-Sánchez, C. Hogan, M. Grüning, D. Varsano, A. Marini, *J. Phys.: Condens. Matter* **2019**, *31*, 325902.
[39] P. Giannozzi, S. Baroni, N. Bonini, M. Calandra, R. Car, C. Cavazzoni, D. Ceresoli, G. L. Chiarotti, M. Cococcioni, I. Dabo, A. Dal Corso, S. de Gironcoli, S. Fabris, G. Fratesi, R. Gebauer, U. Gerstmann, C. Gougoussis, A. Kokalj, M. Lazzeri, L. Martin-Samos, N. Marzari, F. Mauri, R. Mazzarello, S. Paolini, A. Pasquarello, L. Paulatto, C. Sbraccia, S. Scandolo, G. Sclauzero, A. P. Seitsonen, et al., *J. Phys.: Condens. Matter* **2009**, *21*, 395502.
[40] D. E. Aspnes, A. A. Studna, *Phys. Rev. B* **1983**, *27*, 985.
[41] C. Adamo, V. Barone, *J. Chem. Phys.* **1999**, *110*, 6158.
[42] P. Borlido, T. Aull, A. W. Huran, F. Tran, M. A. L. Marques, S. Botti, *J. Chem. Theory Comput.* **2019**, *15*, 5069.
[43] B. C. Wood, E. Schwegler, W. I. Choi, T. Ogitsu, *J. Am. Chem. Soc.* **2013**, *135*, 15774.
[44] A. G. Mohamed, D. Lörch, H. Euchner, M. M. May, P. Bogdanoff, *ChemCatChem* **2025**, *17*, e202401740.
[45] V. Yadav, H. Euchner, M. M. May, Dataset for "Surface Dynamics of Clean and Oxygenated InP(001) Surfaces in Contact with Water - Insights from Computational Spectroscopy", *Zenodo* **2025**, https://doi.org/10.5281/zenodo.17816635

Manuscript received: September 1, 2025
Revised manuscript received: November 26, 2025
Accepted manuscript online: December 2, 2025
Version of record online: ■■, ■■

Supporting Information for: Surface Dynamics of Clean and Oxygenated InP(001) Surfaces in Contact with Water - Insights from Computational Spectroscopy

Vibhav Yadav, Holger Euchner, and Matthias M. May

Universität Tübingen, Institute of Physical and Theoretical Chemistry, Tübingen, Germany

Table S1: Scissor-operator parameters obtained for different surface structures, used to determine the RA spectra. Shift, cslope, and vslope correspond to the shift in band gap and scaling of conduction and valence bands, respectively.

Surface	**Shift(eV)**	**cslope**	**vslope**
$\beta 2(2\times4)$ without H_2O	0.403	1.098	1.138
$\beta 2(2\times4)$ with H_2O	0.35	1.117	1.164
$\beta 2(2\times4)(P_2O_7)_3$ without H_2O	0.246	1.085	1.178
$\beta 2(2\times4)(P_2O_7)_3$ with H_2O	0.7097	1.1	1.198
$(2\times2)(P_2O_6)_2$ without H_2O	0.487	1.086	1.147
$(2\times2)(P_2O_6)_2$ with H_2O	-0.143	1.207	1.206
$(2\times2)(P_2O_7)_2$ without H_2O	0.775	1.037	1.183
$(2\times2)(P_2O_7)_2$ with H_2O	-0.469	1.08	1.207

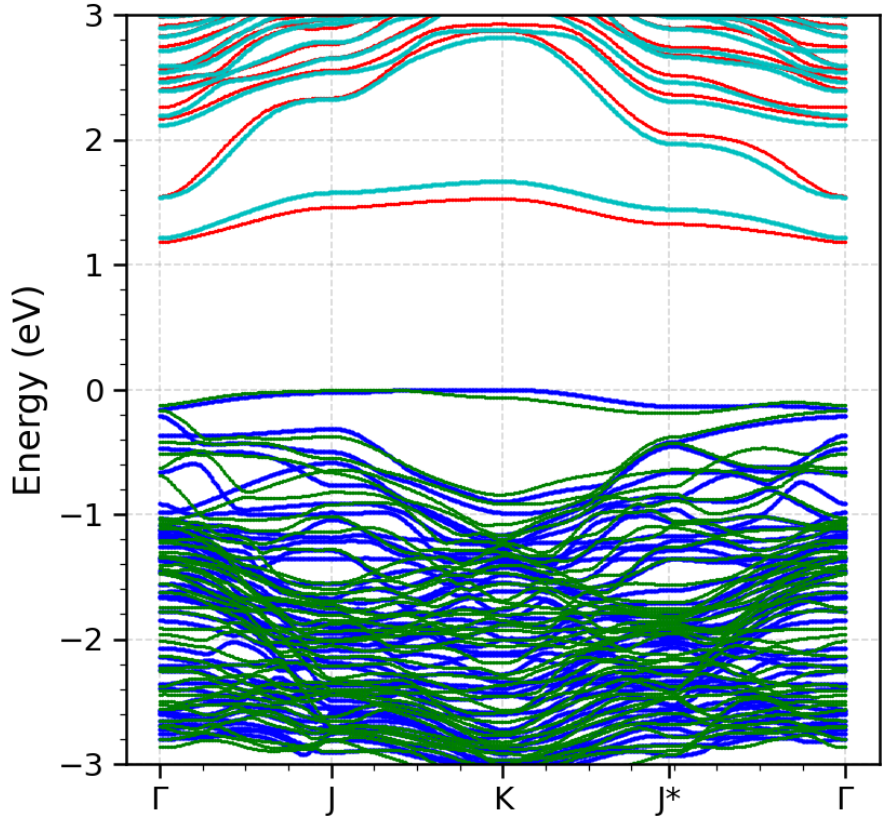

Figure S1: PBE0 (red/green) and fitted PBE (blue/cyan) band structure for the case of the $(2\times2)(P_2O_7)_2$ phase.

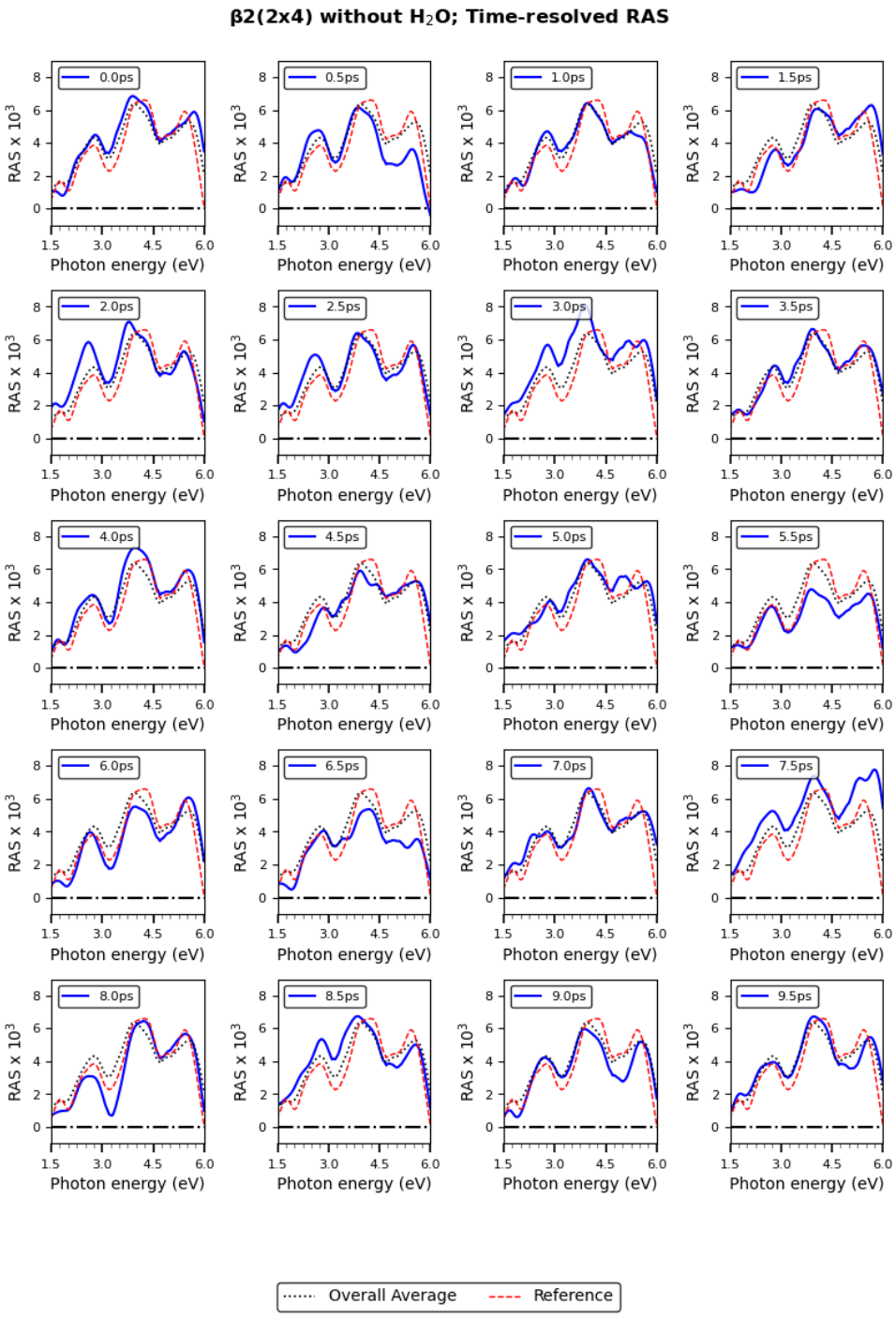

Figure S2: RA spectra of $\beta 2(2\times4)$ without H_2O along the AIMD trajectory. Subplots present the RA spectra corresponding to time average, reference structure, and respective time step.

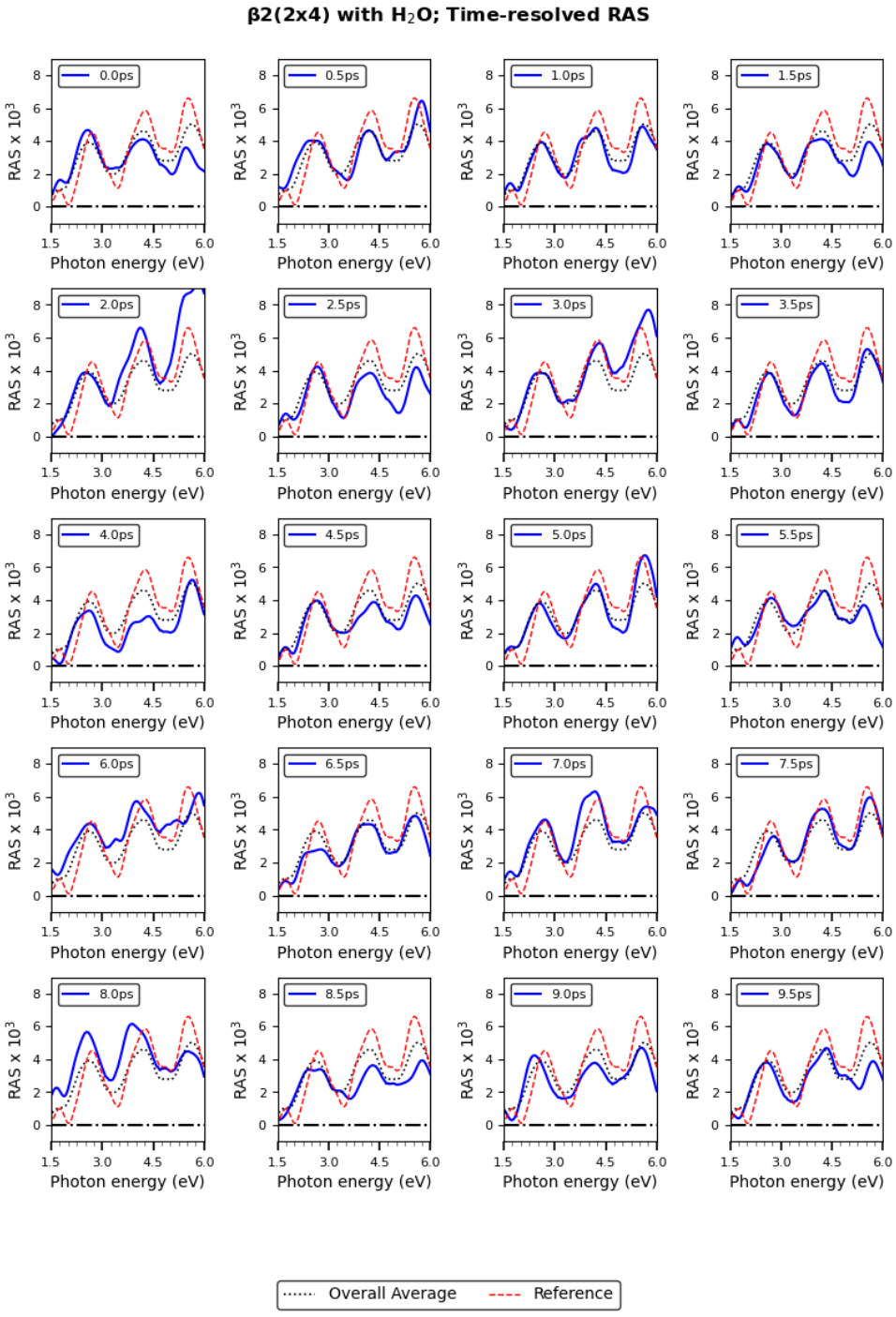

Figure S3: RA spectra of $\beta 2(2\times4)$ with H_2O along the AIMD trajectory. Subplots present the RA spectra corresponding to time average, reference structure, and respective time step.

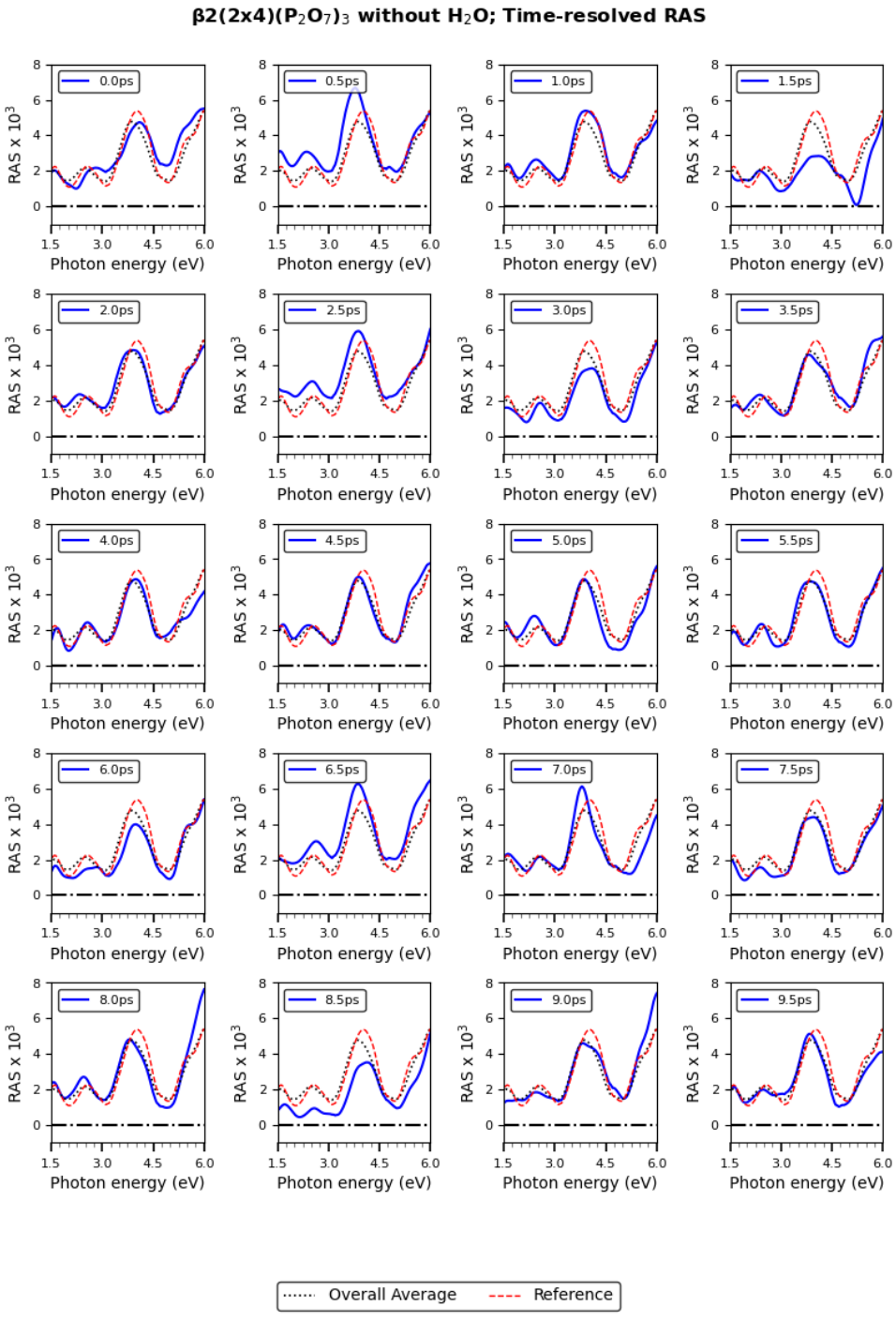

Figure S4: RA spectra of $\beta 2(2\times4)(P_2O_7)_3$ without H_2O along the AIMD trajectory. Subplots present the RA spectra corresponding to time average, reference structure, and respective time step.

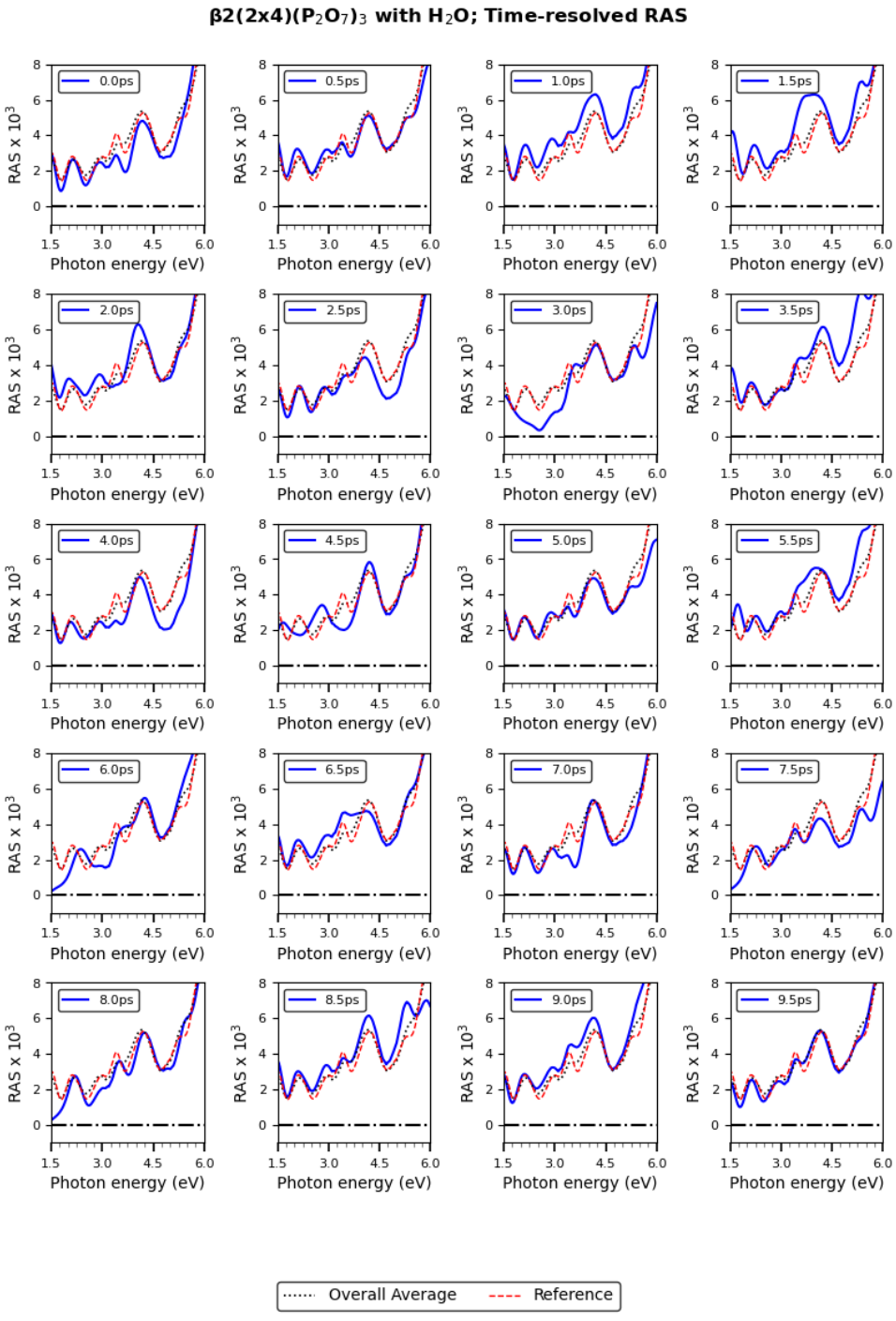

Figure S5: RA spectra of $\beta 2(2\times4)(P_2O_7)_3$ with H_2O along the AIMD trajectory. Subplots present the RA spectra corresponding to time average, reference structure, and respective time step.

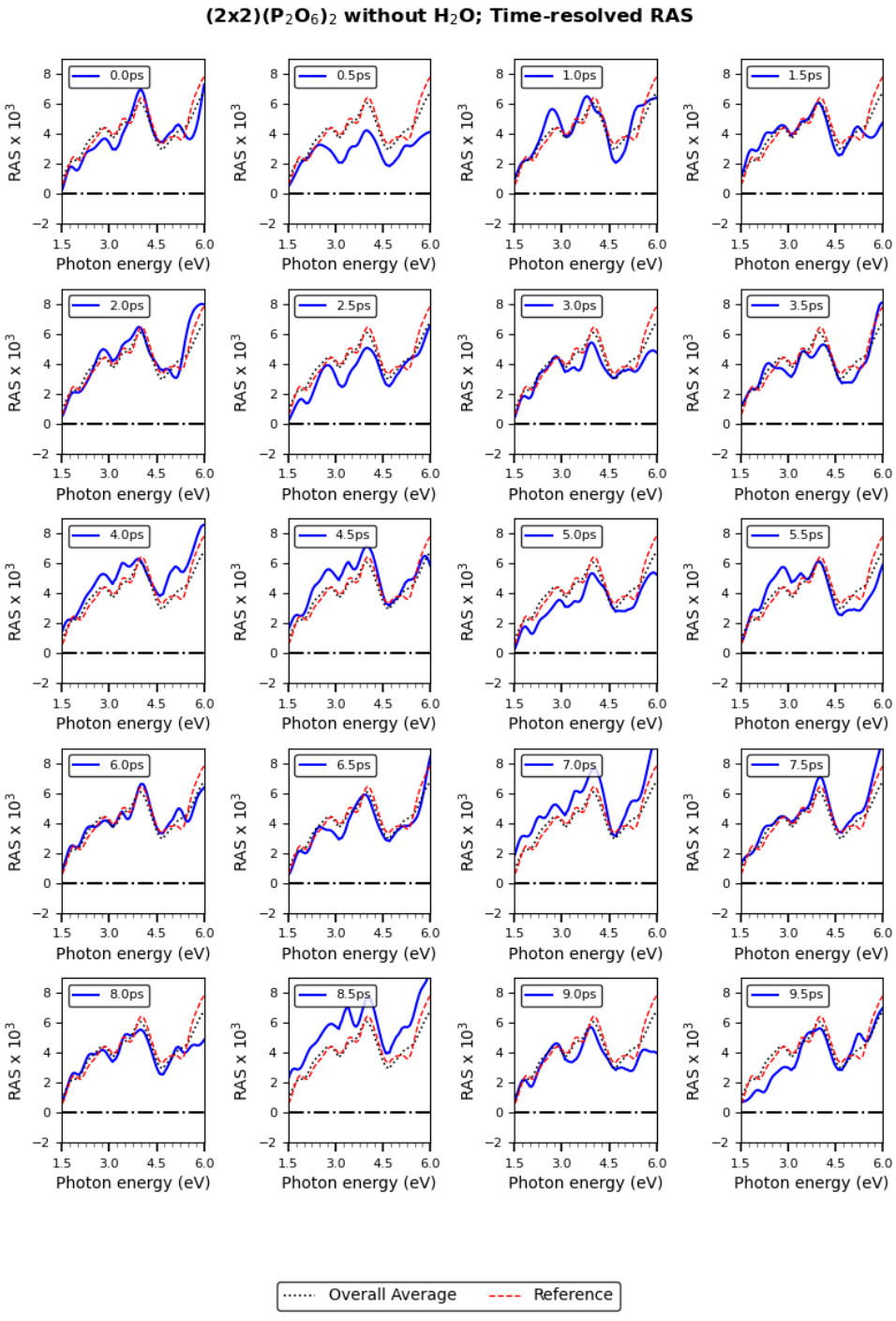

Figure S6: RA spectra of $(2\times2)(P_2O_6)_2$ without H_2O along the AIMD trajectory. Subplots present the RA spectra corresponding to time average, reference structure, and respective time step.

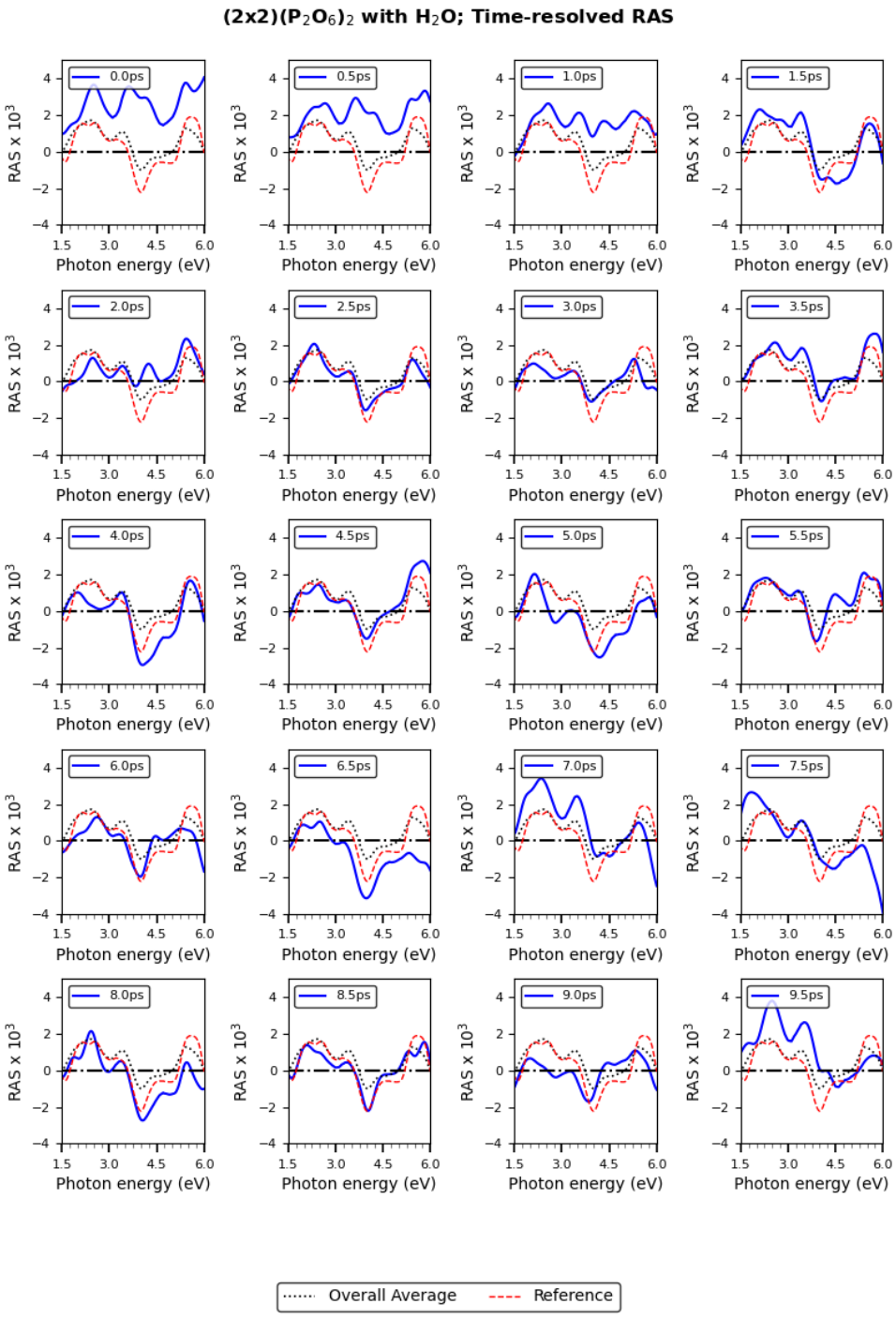

Figure S7: RA spectra of $(2\times2)(P_2O_6)_2$ with H_2O along the AIMD trajectory. Subplots presents the RAS of time-averaged, reference, and respective trajectory.

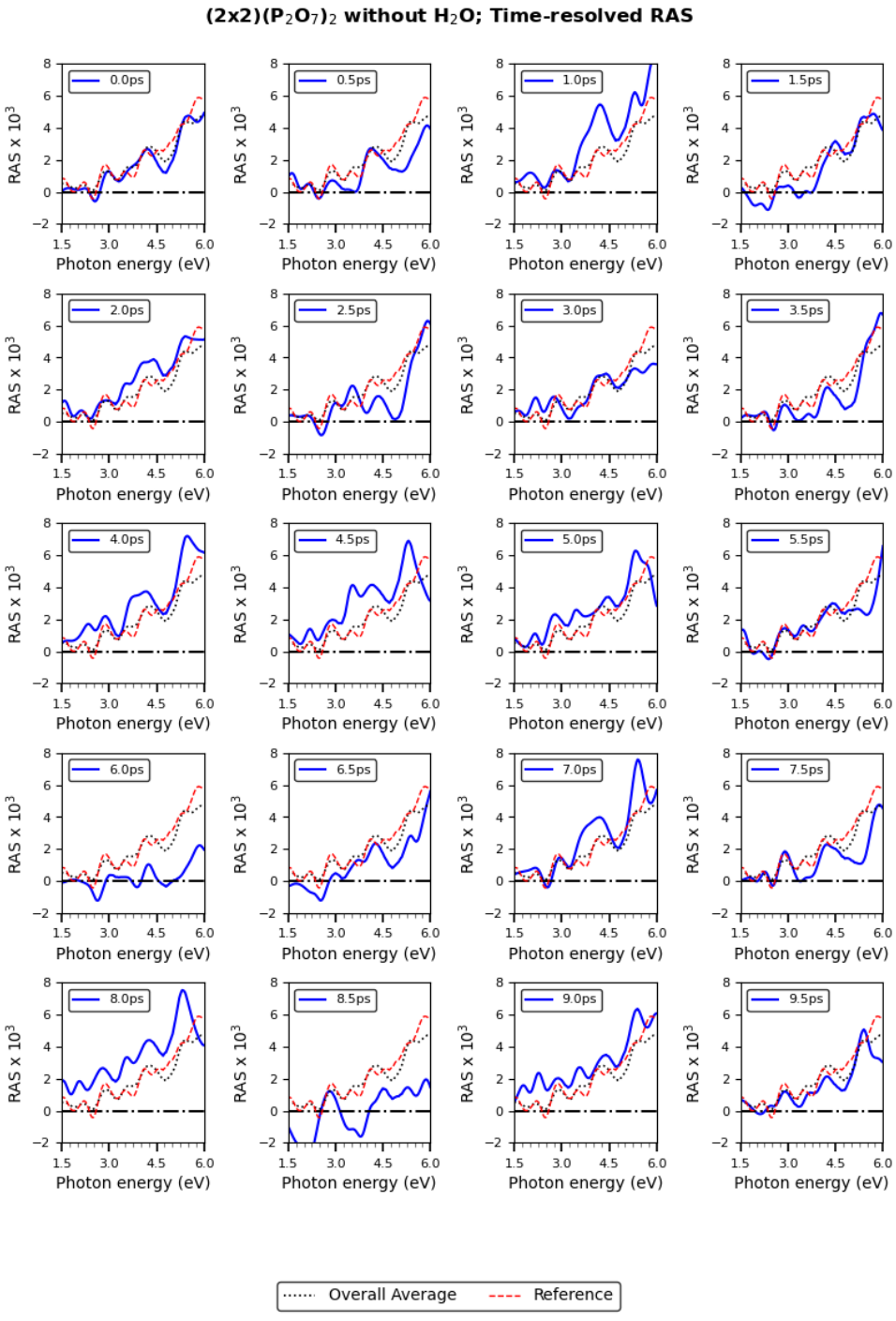

Figure S8: RA spectra of $(2\times2)(P_2O_7)_2$ without H_2O along AIMD trajectories. Subplots present the RA spectra corresponding to time average, reference structure, and respective time step.

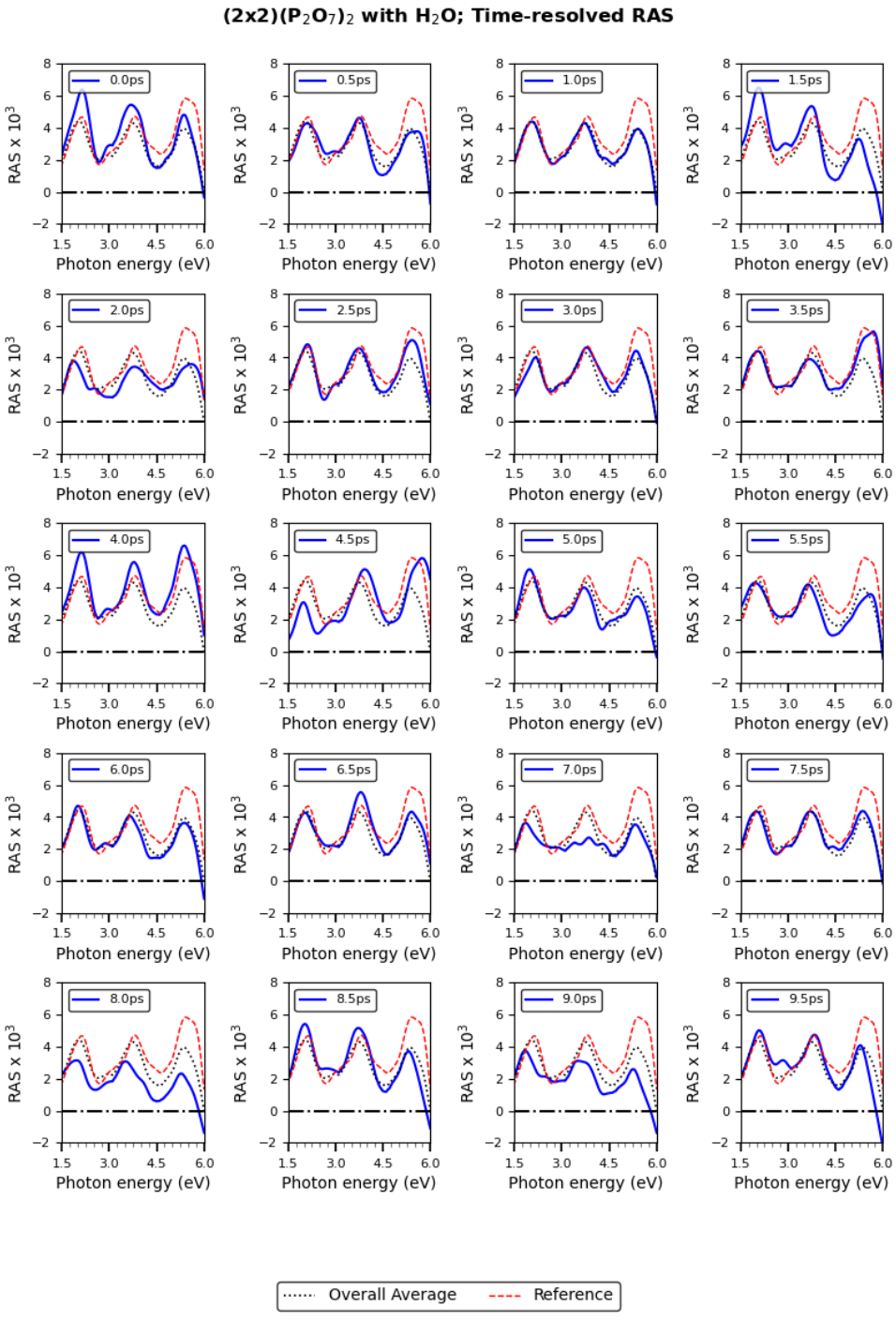

Figure S9: RA spectra of $(2\times2)(P_2O_7)_2$ with H_2O along the AIMD trajectory. Subplots present the RA spectra corresponding to time average, reference structure, and respective time step.

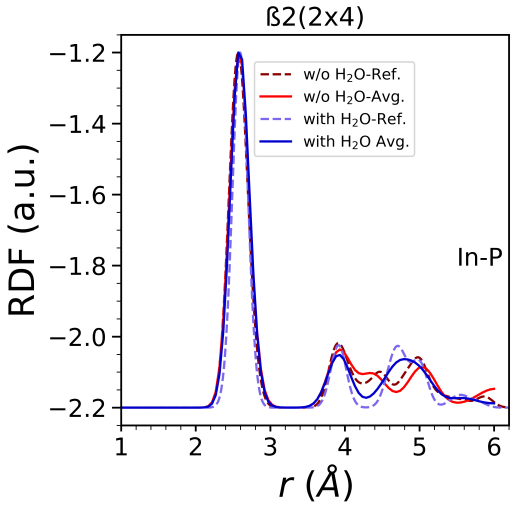

Figure S10: Radial distribution function (RDF) of the In and P atoms in the topmost layers of the $\beta 2(2 \times 4)$ structure with (blue lines) and without water (red lines). The solid lines denote the average RDF obtained along the AIMD trajectory, whereas the dashed lines correspond to the reference structure (see main text) and have been obtained by convolution with a Gaussian to allow for better comparability. The data are scaled with respect to the respective maximum.

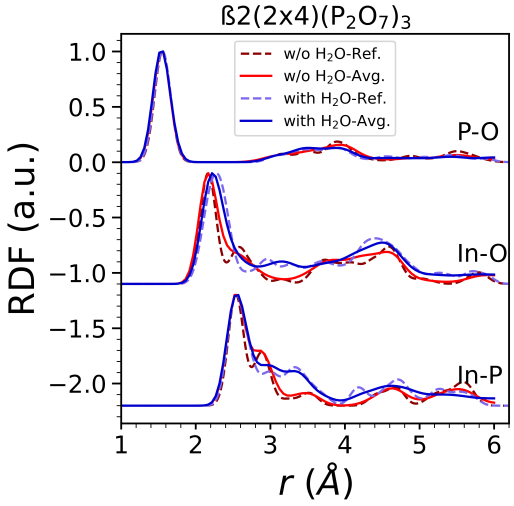

Figure S11: Radial distribution function (RDF) of the In, P and O atoms in the topmost layers of $\beta 2(2\times4)(P_2O_7)_3$ structure with (blue lines) and without water (red lines). The solid lines denote the average RDF obtained along the AIMD trajectory, whereas the dashed lines correspond to the reference structure (see main text) and have been obtained by convolution with a Gaussian to allow for better comparability. The data are scaled with respect to the respective maximum.

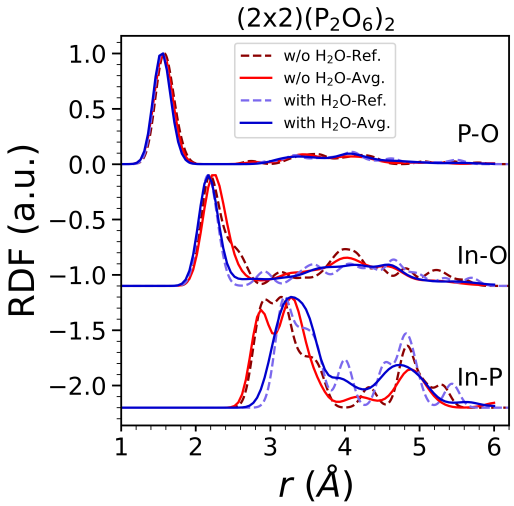

Figure S12: Radial distribution function (RDF) of the In, P and O atoms in the top most layers of the $(2\times2)(P_2O_6)_2$ structure with (blue lines) and without water (red lines). The solid lines denote the average RDF obtained along the AIMD trajectory, whereas the dashed lines correspond to the reference structure (see main text) and have been obtained by convolution with a Gaussian to allow for better comparability. The data are scaled with respect to the respective maximum.

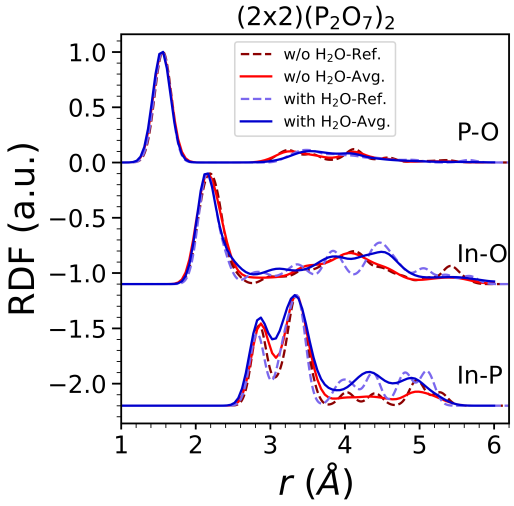

Figure S13: Radial distribution function (RDF) of the In, P and O atoms in the topmost layers of the $(2\times2)(P_2O_7)_2$ structure with (blue lines) and without water (red lines). The solid lines denote the average RDF obtained along the AIMD trajectory, whereas the dashed lines correspond to the reference structure (see main text) and have been obtained by convolution with a Gaussian to allow for better comparability. The data are scaled with respect to the respective maximum.

ACS APPLIED MATERIALS & INTERFACES

www.acsami.org

Research Article

The InP(100) Surface Phase Diagram: From the Gas Phase to the Electrochemical Environment

Holger Euchner,* Vibhav Yadav, and Matthias M. May

Cite This: *ACS Appl. Mater. Interfaces* 2025, 17, 8601−8609

Read Online

ACCESS | Metrics & More | Article Recommendations | Supporting Information

ABSTRACT: The versatile optoelectronic properties of the material class of III−V semiconductors enable the highest performance in photovoltaic and photoelectrochemical solar cells. While a high level of control and understanding with respect to different surface reconstructions of these compounds in gas-phase ambient has been reached, the situation in an electrochemical environment still poses challenges. Here, we therefore have undertaken a computational study of the InP(100) surface in the presence of hydrogen and chlorine, mimicking the contact with a hydrochloric acid-containing electrolyte, aiming at an understanding of ion adsorption and dominant surface reconstructions with respect to applied potential and electrolyte concentration. For this purpose, the most stable surface terminations for hydrogen and chlorine (co)adsorption from the gas phase as well as the corresponding phase diagrams have been determined with respect to the hydrogen and chlorine chemical potential. In this context, we also introduce a quantitative type of phase diagram to highlight the stability of surface phases with respect to competing structures. Finally, by making use of the computational hydrogen electrode approach, these results were then transferred to the potential domain. We find that hydrogen (chlorine) adsorption is dominating at more (less) cathodic potentials, while coadsorption is limited to small fractions of the phase space. This allows us to determine experimentally accessible phases for which no detrimental effects, such as the creation of in-gap surface states, are to be expected.

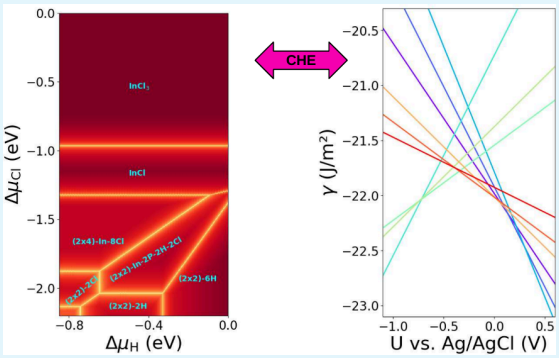

KEYWORDS: *InP(100), Surface Reconstruction, Phase Diagram, Computational Hydrogen Electrode, Density Functional Theory*

INTRODUCTION

The transformation toward a defossilized energy supply of our society has to be realized in the near future to mitigate global warming, meaning that not only electricity but also fuels have to be replaced with renewable alternatives. Here, the production of hydrogen will be part of the solution, with photoelectrochemical (PEC) water splitting having the potential to become an important building block for the future distributed production of carbon-neutral fuels.[1−3] The PEC method is based on an integrated approach, where the photoelectrode is directly immersed in the electrolyte such that photon harvesting and water splitting happen in a single device.[4,5] This comes along with advantages such as compact device design, independence from the electricity grid, and co-benefits from heat exchange between a solar absorber and catalyst.[6] However, the direct contact of the solar absorber and electrolyte results in numerous challenges, in particular with respect to the electrochemical interface. Similar to the case of batteries, the electrochemical interface of the electrode and electrolyte is crucial for the understanding and improvement of the underlying processes, especially with respect to device stability.

Photoelectrodes applied for direct solar water splitting typically show severe stability issues in the electrochemical environment, which directly leads either to dissolution of the electrode or to the degradation-induced formation of surface states in the band gap of the photoabsorber, causing charge-carrier recombination and performance loss. While the successful passivation/functionalization of InP-based photocathodes recently allowed for largely improved performance, the exact structure of the stable interfaces and its functioning are still an open question.[7] In a first approach, we therefore study the simple binary InP(100) surface—*the drosophila* of III−V photoelectrochemistry—to gain insight into the complex structure and processes occurring at the electrode/electrolyte interface.

For this purpose, we have studied the surface phase diagram of InP in an electrochemical environment, consisting of

Received: November 20, 2024
Revised: January 9, 2025
Accepted: January 13, 2025
Published: January 21, 2025

https://doi.org/10.1021/acsami.4c20370
ACS Appl. Mater. Interfaces 2025, 17, 8601−8609

aqueous solutions of hydrochloric acid (HCl), via density functional theory (DFT). Here, it has to be noted that studies considering the phase stability beyond the clean InP(100) surface are rather limited,[8−14] while electrochemical environments, including the impact of electrolyte constituents and applied potential on the surface structure, so far have not been addressed at all. Hence, starting from different surface reconstructions of InP(100), we have investigated the adsorption of hydrogen and chlorine upon the latter ones, motivated by the finding that highly ordered interfaces/phases exist under these conditions, whose exact structures are, however, not yet fully identified.[15] The resulting surface phase diagrams, obtained for hydrogen and chlorine adsorption in a vacuum (from the gas phase) and depicted as a function of the respective chemical potentials (μ_H and μ_{Cl}), contain a variety of stable phases that show hydrogen and chlorine adsorption. However, only for a small part of the phase space, i.e., for very specific conditions, is the coadsorption of hydrogen and chlorine observed. Furthermore, to translate these findings to an electrochemical environment, the concept of the computational hydrogen electrode has been applied.[16] This consequently allows the determination of the surface phase diagram in an aqueous electrolyte, by evaluating the surface free energy as a function of the electrochemical potentials of hydrogen ($\tilde{\mu}_H$) and chlorine ($\tilde{\mu}_{Cl}$). Finally, by selecting a certain electrolyte composition, the phase diagram can be transformed in the potential domain, such that the phase stability with respect to an applied potential can be extracted, in principle allowing for comparison to the corresponding experimental data.[15,17]

METHODS

Density functional theory-based calculations have been performed to determine the surface phase diagram of InP in the presence of hydrogen and chlorine. For this purpose, different, well-known reconstructions of the pristine InP(100) surface, as can be prepared in ambient gas-phase conditions,[18] have been optimized and used as starting configurations for hydrogen and chlorine adsorption. To allow for an efficient modeling of the respective surfaces, asymmetric slabs with pseudohydrogen termination at the bottom were constructed, thus preventing the occurrence of dangling bonds and spurious states in the band structure. All DFT calculations were conducted with the CP2K code using the Gaussian and plane wave (GPW) method, using the DZVP-MOLOPT-SR-GTH basis set in combination with the Godecker−Teter−Hutter pseudopotentials, applying a cutoff of 800 Ry together with a relative cutoff of 60 Ry.[19,20] Exchange and correlation were described via the PBE functional, while in addition, a dispersion correction was applied as introduced by Grimme et al. (vdW-D3).[21,22] First, the bulk structure of InP was optimized with the above-described settings, yielding a lattice parameter of 5.935 Å for the cubic unit cell. Starting from this structure, different surface unit cells for the InP(100) surface were constructed. All investigated surfaces were based on a 12-layer structure (six In and six P layers) with fixed cell dimensions along the *c*-axis, such that each structure was terminated by a vacuum layer of at least 15 Å thickness (see Figure S1 in the Supporting Information (SI)).

COMPUTATIONAL HYDROGEN ELECTRODE

To access surface phase diagrams in the gas-phase ambient, a grand canonical approach has to be applied,[23,24] relating the calculated surface energies to different experimental conditions, corresponding to the availability of the respective atoms. This can be achieved by expressing the Gibbs free surface energy $\gamma(T, p)$ as a function of the chemical potential, μ_i, of the corresponding gas-phase molecules, normalized to the surface area A. This results in the following equation:

$$\gamma(T, p) = \frac{1}{A}\left(G(T, p, N_i) - \sum_i N_i\mu_i(T, p)\right) \quad (1)$$

Here, N_i is the number of atoms of type i, whereas G is the Gibb's free energy of the slab, which in ab initio-based approaches is frequently approximated by the corresponding total energy E_{slab}, meaning that entropy and volume change are neglected. By introducing $\Delta\mu_i(T, p) = \mu_i(T, p) - E_i$, the chemical potential is typically renormalized with respect to the ground state energy of the respective elements E_i, thus yielding

$$\gamma(T, p) = \frac{1}{A}\left(E_{surf} - \sum_i N_i\Delta\mu_i(T, p)\right) \quad (2)$$

with $E_{surf} = E_{slab} - \sum_i N_i E_i$. Starting from this equation, the most stable surface structures, those with the lowest surface free energy, can be determined.

When systems in the electrochemical environment are considered, the presence of charged species has to be accounted for, which means that, in the above formalism, the chemical potential has to be replaced by the electrochemical potential ($\tilde{\mu} = \mu + ze\phi$). Accessing the surface free energies in the electrochemical environment, on the other hand, would in principle mean calculating solvation free energies for the respective ions in solution. This is, however, a computationally extremely demanding task. Fortunately, there exists an elegant and well-established approach to connect the electrochemical potentials of molecules in the gas phase and their corresponding ions in solution: the computational hydrogen electrode (CHE).[16] The underlying idea of the CHE is the fact that the standard hydrogen electrode (SHE) at standard conditions yields a reference point at which hydrogen gas and protons in solution are in equilibrium, i.e., $\tilde{\mu}_{H^+_{(aq)}} + \tilde{\mu}_{e^-} = \frac{1}{2}\mu_{H_2}$. Consequently, by exploiting this relation, one only has to compute the energy of a hydrogen molecule in the gas phase, instead of directly computing the corresponding solvation energies.[16,24,25] Since the potential dependence of an electron at the Fermi level and the pH dependence of an ion in solution are well-known, the electrochemical potential of a proton and electron in solution can be expressed by the following equation:

$$\tilde{\mu}_{H^+_{(aq)}} + \tilde{\mu}_{e^-} = \frac{1}{2}\mu_{H_2} - eU_{SHE} - k_BT\ln(10)pH \quad (3)$$

with U_{SHE} the potential with respect to the standard hydrogen electrode scale. It is now easy to extend this concept to any other species in solution.[26,27] For the case of chlorine the corresponding equation reads as

$$\tilde{\mu}_{Cl^-_{(aq)}} - \tilde{\mu}_{e^-} = \frac{1}{2}\mu_{Cl_2} + e(U_{SHE} - U_0) + k_BT\ln(c_{Cl^-}) \quad (4)$$

with U_0 the standard potential of the Cl/Cl^- redox couple (i.e., 1.36 V) versus SHE.[28] Note that in eq 4 the concentration is used instead of the formally correct activity, an approximation valid for low concentrations.[29]

In the here-described grand canonical approach, the temperature-, concentration-, and potential-dependence of the electrochemical potential can also be renormalized and

https://doi.org/10.1021/acsami.4c20370
ACS Appl. Mater. Interfaces 2025, 17, 8601−8609

combined in a single term, $\Delta\tilde{\mu}$, yielding the following equation for the case of protons:

$$\Delta\tilde{\mu}_{H^+}(T, p, U) = \tilde{\mu}_{H^+_{(aq)}}(T, p, U) + \tilde{\mu}_{e^-} - \frac{1}{2}E_{H_2}$$
$$= -eU_{SHE} - k_B T \ln(10)\text{pH} \quad (5)$$

For the chlorine ion, one obtains

$$\Delta\tilde{\mu}_{Cl^-}(T, p, U) = \tilde{\mu}_{Cl^-_{(aq)}}(T, p, U) - \tilde{\mu}_{e^-} - \frac{1}{2}E_{Cl_2}$$
$$= e(U_{SHE} - 1.36) + k_B T \ln(c_{Cl^-}) \quad (6)$$

In this formulation, the total energy of the gas-phase molecules is subtracted from the electrochemical potential of the solvated ion and corresponding electrons. This renormalization is, as in the above-discussed vacuum case, based on the assumption that the free energies of the molecules can be approximated by the total energy that is directly accessible by DFT. Making use of the above derived expressions, the change in Gibbs free surface energy can finally be expressed as

$$\gamma(T, p, U) = \frac{1}{A}\left(E_{surf} - \sum_i N_i \Delta\tilde{\mu}_i(T, c, U)\right) \quad (7)$$

This now enables us to also compute phase diagrams as a function of the electrochemical variables. However, it must be pointed out that the typical application of the CHE, as outlined above, comes with certain limitations. The fact that in eq 7 total energies are used means that the electrochemical environment is not directly accounted for as the free energy is assumed to be independent of the electrochemical variables such as the applied potential.[30] Furthermore, in the methodology applied here, where DFT calculations in a vacuum are considered, effects such as the charging of the electrode and the electrochemical double layer and their effect on energetics and electronic structure (band bending) are not accounted for. Consequently, results for semiconducting systems in contact with an electrolyte obtained by the CHE approach are strictly speaking valid for only uncharged interfaces. Unlike for metals, a surface charge on a semiconductor will not be fully screened, leading to a finite electric field within the semiconducting slab.[31,32] This will effectively introduce a certain level of uncertainty with respect to the potential domain when comparing these results directly with experiment.

RESULTS AND DISCUSSION

In the following, the InP(100) surface and its reconstructions are addressed in a stepwise approach. Starting from the clean surface in the presence of only In and P, the adsorption of hydrogen and chlorine is considered separately before a combined adsorption is investigated. These scenarios are first considered for gas-phase ambient conditions before the results are exploited for a given electrochemical environment.

Clean Surface. First, the phase diagram of the pristine InP(100) surface (in vacuum) has been reinvestigated with respect to the chemical potential of In and P, which in experiment are determined by the exact growth/surface preparation conditions. Since the chemical potentials of In and P are interrelated via the stability of the InP bulk phase under equilibrium conditions ($\mu_{InP} = \mu_{In} + \mu_P$), the surface energy can be expressed as a function of only the In chemical potential:

$$\Delta G \approx E_{slab} - (\mu_{InP} - \mu_{In})N_P - \mu_{In}N_{In} \quad (8)$$

The resulting phase diagram shows the so-called (2×2)-2D, $c(4 \times 4)$, $\alpha 2(2 \times 4)$, $\beta 2(2 \times 4)$, and mixed-dimer phases as stable clean surfaces. Since all further calculations are based on the surface reconstructions introduced here, these will be described in some detail in the following. The (2×2)-2D surface corresponds to a P-terminated surface with two additional P-dimers on top. The $c(4 \times 4)$ phase is closely related to the (2×2)-2D reconstruction, being constructed from a larger supercell that is also terminated by phosphorus with three additional P-dimers on top. Finally, there are three different structures that are based on 2×4 supercells. The $\alpha 2(2 \times 4)$ and $\beta 2(2 \times 4)$ phases can be understood as stepped surfaces, which differ in the number of terminating P atoms. The mixed dimer structure, on the other hand, corresponds to an In-terminated surface with a single, "mixed" In−P dimer on top.

The phase diagram shows that with increasing In chemical potential, the more In-rich surface terminations become dominant, culminating in the mixed dimer surface. For intermediate $\Delta\mu_{In}$ values, the $\alpha 2(2 \times 4)$ and $\beta 2(2 \times 4)$ phases are the most stable ones. When $\Delta\mu_{In}$ decreases further, the $c(4 \times 4)$ is observed for a small potential range. Finally, for P-rich conditions, the (2×2)-2D surface is stabilized. Apart from the fact that the (2×2)-1D structure is found to be slightly unstable, this is in agreement with literature.[33] These differences are likely due to the different exchange−correlation functionals and the negligence of van der Waals interactions in earlier calculations.

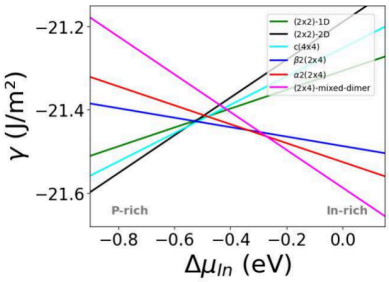

Figure 1. Phase diagram of the clean InP(100) surface as a function of the In chemical potential. The corresponding structures are depicted in Figure 2.

Hydrogen and Chlorine Adsorption. As the next step, the impact of hydrogen was investigated by computing the corresponding phase diagram in the presence of hydrogen. For this purpose, the different stable plain surfaces and derivatives

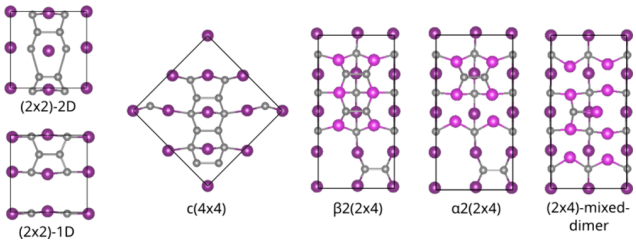

Figure 2. Different surface reconstructions of the InP(100) surface. In atoms are depicted in purple (and pink if two In layers are shown), while P atoms are shown in gray.

https://doi.org/10.1021/acsami.4c20370
ACS Appl. Mater. Interfaces 2025, 17, 8601−8609

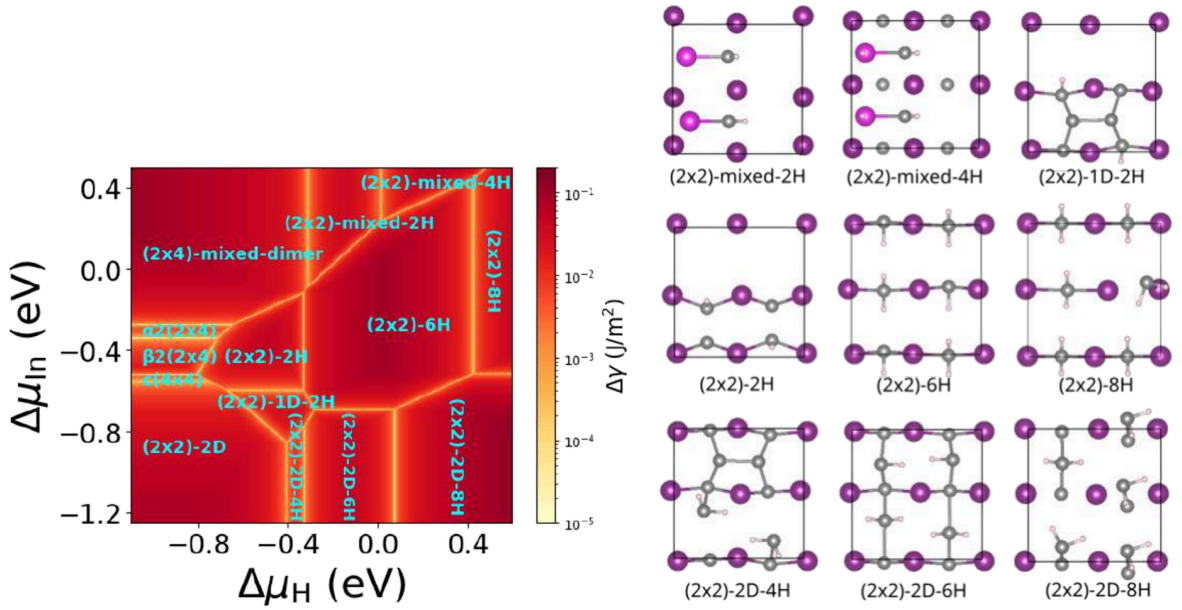

Figure 3. Phase diagram of the InP(100) surface with respect to the In and H chemical potential and corresponding structures (top view). In and P atoms of the topmost layers are depicted in purple (and pink if two In layers are shown) and gray, whereas H is shown in light pink.

thereof were decorated with different numbers and arrangements of hydrogen atoms. In total more than 300 different configurations were structurally optimized, finally yielding the corresponding surface energies as a function of the renormalized In and hydrogen chemical potentials $\Delta\mu_{In}$ and $\Delta\mu_H$ as depicted in Figure 3. Before the discussion of the resulting phase diagram, a consistent nomenclature for hydrogen-terminated surfaces will be introduced. In the following, structures with hydrogen on P-terminated (2 × 2) surfaces will be termed (2 × 2)-*n*H phases, whereas phases based on the P-dimer terminated (2 × 2)-2D phase will be termed (2 × 2)-2D-*n*H phases. Here, a note of caution is necessary, as in earlier works a (2 × 2)-2D-2H structure is reported that refers to the P-terminated surface without additional phosphorus,[18] which in the here introduced convention corresponds to the (2 × 2)-2H phase.

Regarding the phase diagram, as expected, the pristine surface reconstructions are observed at low $\Delta\mu_H$ values (low $\Delta\mu_H$ corresponds to a low hydrogen partial pressure). For increasing $\Delta\mu_H$, hydrogen-terminated surfaces become stabilized. Interestingly, under P-rich conditions as well as In-rich conditions, the pristine clean phases remain stable over a wider range of $\Delta\mu_H$. Here, it has to be noted that the phase diagram differs somewhat from literature,[18] which again may be attributed to the use of different exchange−correlation functionals and/or the larger number of competing structures that were considered in our study. Furthermore, it must be pointed out that the energy differences between certain configurations are often rather small.

To take these uncertainties into account, the phase diagram is represented such that the stability of the thermodynamically stable phases with respect to competing phases of different stoichiometry is color-coded. This is achieved by computing the energy difference between the most stable and second most stable phases at a particular value of $\Delta\mu_H$ and $\Delta\mu_{In}$. This value is then used as a descriptor for phase stability and represented by the color code in Figure 3. Hence, the darker a particular area is depicted in the phase diagram, the likelier the occurrence of the corresponding phase. A large part of the phase diagram comprises the (2 × 2)-*n*H phases (with n = 2, 6, 8), which correspond to phosphorus-terminated surfaces with hydrogen atoms replacing the top P-dimer. Here, the (2 × 2)-6H phase covers a rather large area and is, as can be inferred from the darker color, also expected to be quite stable. The maximum coverage is reached when each top layer phosphorus atom is terminated by two hydrogen atoms. The resulting (2 × 2)-8H phase already shows distortions of the PH_2 units at the surface and is only stable for $\Delta\mu_H > 0.4$. For P-rich conditions, (2 × 2)-2D-based structures with hydrogen atoms filling the available sites on the P-dimers become stable for increasing $\Delta\mu_H$. Here, again, the maximum hydrogen content on the surface seems to be reached with a total of 8 hydrogen atoms, meaning a P-terminated surface with 4 PH_2-units on top. Finally, for In-rich conditions and increasing $\Delta\mu_H$, mixed-dimer-like surface terminations are found to be the most stable. The (2 × 2)-mixed phases correspond to an In-rich surface that is terminated by two mixed dimers, where first both P-sites ((2 × 2)-mixed-2H) and then both In-sites ((2 × 2)-mixed-4H) of the In−P dimers are occupied by hydrogen. Interestingly, the $\alpha2(2 \times 4)$- and $\beta2(2 \times 4)$-based phases are not observed any more when hydrogen is present. This is because for intermediate $\Delta\mu_{In}$ values the fully P-terminated (2 × 2)-based phases are stabilized. This stabilization is a consequence of the higher availability of P-sites for the formation of P−H bonds. Here, it has to be noted that not all of the structures that are found to be stable—in particular those based on the P-rich (2 × 2)-2D surface—comply with the electron counting rules introduced by Pashley.[34] Finally, it has to be pointed out that, while a large number of different configurations have been investigated, it cannot be excluded that larger supercells may yield additional stable reconstructions with intermediate hydrogen content.

Similarly, the adsorption of chlorine on the different InP(100) surface reconstructions was considered, now allowing us to compute the phase diagram as a function of the indium and chlorine chemical potentials $\Delta\mu_{In}$ and $\Delta\mu_{Cl}$, as

https://doi.org/10.1021/acsami.4c20370
ACS Appl. Mater. Interfaces 2025, 17, 8601−8609

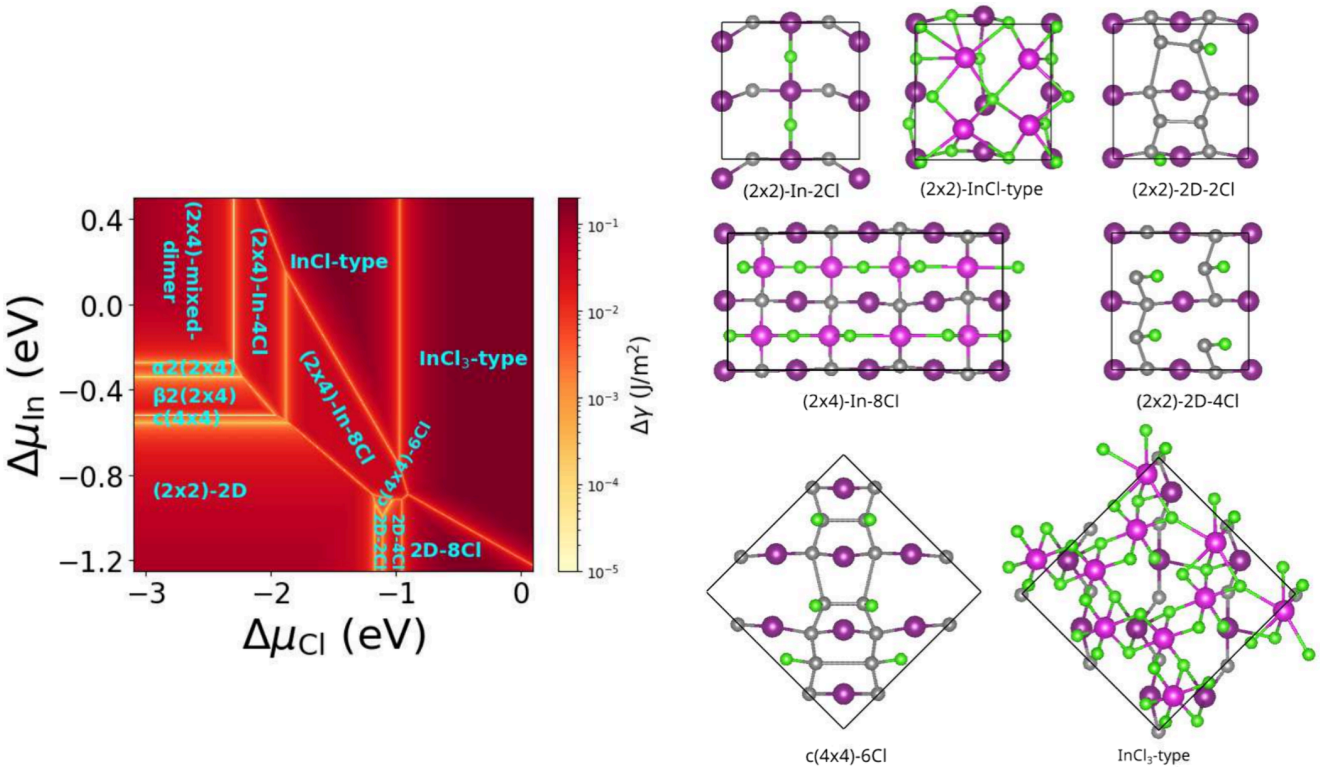

Figure 4. Phase diagram of the InP(100) surface with respect to the In and Cl chemical potential and corresponding structures (top view). In and P atoms of the topmost layers are depicted in purple (and pink if two In layers are shown) and gray, whereas chlorine is shown in light green.

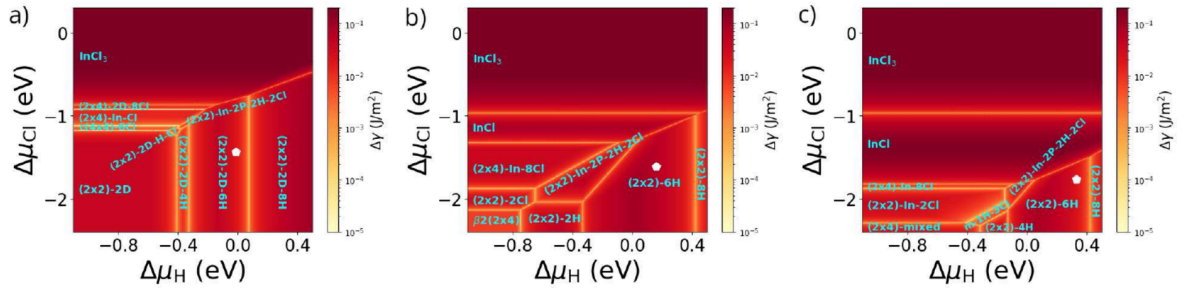

Figure 5. Phase diagram of the InP(100) surface with respect to the chemical potentials of H and Cl for a fixed In chemical potential. (a) In-rich ($\Delta\mu_{In}$ = −0.9 eV), (b) intermediate ($\Delta\mu_{In}$ = −0.4 eV), and (c) P-rich ($\Delta\mu_{In}$ = 0.1 eV) conditions. The white pentagons represent particular combinations of $\Delta\mu_{In}$, $\Delta\mu_{H}$, and $\Delta\mu_{Cl}$, corresponding to applied potentials of approximately −0.25, −0.42, and −0.58 V, respectively.

shown in Figure 4. Again, the pristine surface reconstructions are observed at low $\Delta\mu_{Cl}$ values. Here, it has to be noted that they are observable for significantly lower chemical potentials, as in the case of hydrogen, which is a consequence of the higher reactivity of chlorine. For increasing $\Delta\mu_{Cl}$, chlorine-terminated surfaces become quickly stabilized. For increasing $\Delta\mu_{Cl}$ and under P-rich conditions, the pristine (2 × 2)-2D phase shows an extended stability range and is followed by surfaces for which an increasing number of Cl atoms are located on top of the P-dimer sites, with the (2 × 2)-2D-8Cl phase already being largely disordered. For In-rich conditions, the In-terminated (2 × 2)-In-2Cl and (2 × 4)-In-8Cl phases become stable for increasing $\Delta\mu_{Cl}$ values, before an InCl-like layer becomes stabilized. Interestingly, at a large $\Delta\mu_{Cl}$, the formation of an $InCl_3$-like layer becomes stable over the whole $\Delta\mu_{In}$ range. Both InCl-type phases cover a rather large range of the phase space and are, as can be seen from the dark color in the phase diagram, expected to be comparably stable. As can be inferred from the large part of the phase space that is covered by In-rich surface terminations, chlorine has a strong preference to form In−Cl bonds, whereas P−Cl bonds only form under P-rich conditions. As in the case of hydrogen, there may exist larger supercells that stabilize additional intermediate Cl concentrations.

Following the same approach as in the previous paragraphs, the co-adsorption of hydrogen and chlorine was considered. Now, the different plain surfaces and their derivatives were decorated by different numbers and arrangements of hydrogen and chlorine atoms. In principle, the phase diagram can now be obtained as a function of the renormalized chemical potentials of In, Cl, and H. However, to allow for a better graphical representation, phase diagrams for three selected values of the In chemical potential have been chosen. The resulting graphs correspond to two-dimensional cuts through the three-dimensional phase space, spanned by the chemical potentials of In, Cl, and H. Choosing a fixed value for $\Delta\mu_{In}$ can also be

https://doi.org/10.1021/acsami.4c20370
ACS Appl. Mater. Interfaces 2025, 17, 8601−8609

understood as chlorination/hydrogenation of a particular surface reconstruction. The resulting phase diagrams for In-rich ($\Delta\mu_{In}$ = −0.9 eV), intermediate ($\Delta\mu_{In}$ = −0.4 eV), and P-rich ($\Delta\mu_{In}$ = 0.1 eV) conditions correspond to selecting the (2 × 2)-2D, β2(2 × 4), and the mixed-dimer reconstructions as clean surfaces, respectively.

These combined phase diagrams, depicted in Figure 5a−c, clearly show the dominant nature of chlorine adsorption. For increased chlorine chemical potentials, the $InCl_3$-like overlayer is observed for the different $\Delta\mu_{In}$ values and, moreover, is essentially independent from the hydrogen chemical potential. The dark color of the corresponding phase space area indicates that $InCl_3$-type phases are significantly more stable than the competing structures that have been investigated. Only at low chlorine chemical potential are hydrogen-containing phases observed. For more In-rich conditions (Figure 5b and c), the phase space that is dominated by chlorine-rich phases is further increasing, while hydrogen-containing surfaces are only observed for further decreased $\Delta\mu_{Cl}$ values. This essentially confirms our previous findings for the separate hydrogen and chlorine absorption and can be understood from the fact that hydrogen prefers to bind to phosphorus, whereas Cl prefers to form bonds with In. Consequently, the more indium-rich the conditions are, the more dominant the Cl adsorption and hence the Cl-rich phases. However, even under P-rich conditions, chlorine adsorption takes place for a large part of the phase diagram.

Interestingly, for the three selected In chemical potentials, the co-adsorption of hydrogen and chlorine is only observed for a very narrow range in chemical potential. This corresponds well with adsorption studies on metal electrodes,[26] where similar behavior was observed. In the case of P-rich conditions ($\Delta\mu_{In}$ = −0.9 eV), two tiny areas with hydrogen/chlorine co-adsorption are observed (see Figure 5a). For rather low values of $\Delta\mu_{Cl}$ and $\Delta\mu_{H}$, a (2 × 2)-2D-based structure with a hydrogen and a chlorine atom sitting on the same dimer, the (2 × 2)-2D-H-Cl phase, is observed (see Figure 6). Increasing $\Delta\mu_{Cl}$ and $\Delta\mu_{H}$ values foster an In-terminated surface with partial P-coverage, the (2 × 2)-In-2P-2H-2Cl structure, with the P atoms being saturated by hydrogen and Cl atoms occupying the free P-sites. At larger In chemical potential ($\Delta\mu_{In}$ = −0.4 eV), only the latter co-adsorption phase prevails,

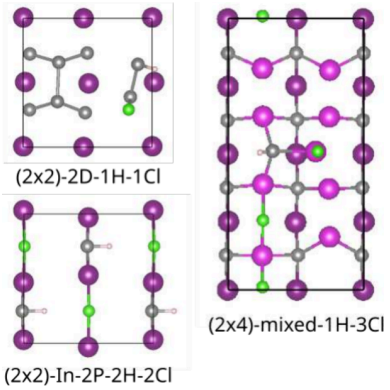

Figure 6. Surface reconstructions with hydrogen and chlorine co-adsorption (top view). In and P atoms of the topmost layers are depicted in purple (and pink if two In layers are shown) and gray, whereas chlorine and hydrogen are shown in light green and light pink.

which is a consequence of its increased In content as compared to the (2 × 2)-2D-H-Cl phase. In fact, the (2 × 2)-In-2P-2H-2Cl phase even occupies an increased area in the phase diagram, as can be seen in Figure 5b. Finally for $\Delta\mu_{In}$ = 0.1 eV, again the (2 × 2)-In-2P-2H-2Cl phase is observed, as well as a mixed dimer based surface (mixed-1H-3Cl) with the P and In atoms of the dimer being saturated by H and Cl and two additional Cl atoms forming In−Cl−In bonds (see Figure 6).

From Gas-Phase to Electrochemical Environment. While the phase diagrams discussed in the previous paragraphs are relevant for the adsorption of hydrogen and chlorine in a gas-phase environment, which is of great importance for epitaxial growth, the question of the predominant phases for systems in contact with an electrochemical environment remains open. However, making use of the above-introduced CHE concept and also applying it for the case of indium allow the transfer of the obtained phase diagrams to the potential domain. This means the phase diagram can be expressed with respect to the applied potential for given concentrations of hydrogen, chlorine, and indium in the electrolyte solution. For this purpose, the standard potentials of the corresponding redox couples have to be used to relate them to the SHE scale (see Table 1).

Table 1. Redox Potentials of H/H^+, In/In^{3+}, Cl/Cl^-, and Ag/AgCl vs SHE

redox couple	potential (vs SHE)
H/H^+	0 V
In/In^{3+}	−0.338 V[28]
Cl/Cl^-	+1.360 V[28]
Ag/AgCl	−0.197 V[35]

Consequently, for fixed In, Cl, and H concentrations, as in an electrochemical experiment, the phase diagram can be depicted as a function of the applied potential. In the following, the concentrations of In, Cl, and H are assumed to stem from the dissolution of 0.01 molar $InCl_3$ in 0.1 molar hydrochloric acid (pH 1), thus corresponding to realistic experimental conditions.[15,17] Note that the potential is depicted with respect to the Ag/AgCl scale (−0.197 V vs SHE) to facilitate comparison to experimental data. To get a first idea on the impact of an applied potential, the phase diagram of the pristine InP(100) surface reconstructions is considered; that is, chlorine and hydrogen adsorption are neglected. Still, this simplified model contains some important insights, showing that transitions between the different clean phases all would lie in a very narrow potential window (see Figure 7a). The transitions between the stable surface reconstructions all lie within about 0.1 V, with the In-rich mixed-dimer structure dominating for more cathodic potentials (below ∼−0.5 V) and the P-rich (2 × 2)-2D being dominant for more anodic potentials (above ∼−0.4 V).

These findings already indicate that α2(2 × 4), β2(2 × 4), and c(4 × 4) reconstructions are rather unlikely to be observed in an electrochemical environment, even under the assumption of negligible hydrogen and chlorine adsorption. On the other hand, when the full phase space is taken into account, the phase diagram in Figure 7b is obtained. At more cathodic potentials, hydrogen-terminated surfaces are observed, however, with different In/P content. In fact, with increasing (less cathodic) potential, the surfaces get more P-rich, resulting in transitions between surfaces with mixed In−P termination

https://doi.org/10.1021/acsami.4c20370
ACS Appl. Mater. Interfaces 2025, 17, 8601−8609

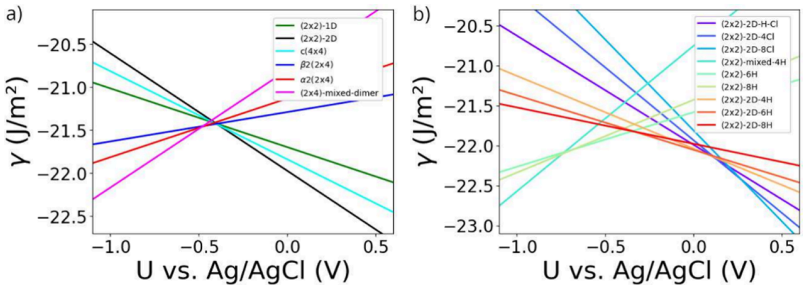

Figure 7. Phase diagram of the InP(100) surface as a function of the applied potential for a 0.01 molar $InCl_3$ solution at pH 1. In (a) only the stability of the plain surface reconstructions is considered, while (b) considers H and Cl adsorption.

(based on (2 × 2)-mixed structures) to P-terminated (2 × 2)-based surfaces and (2 × 2)-2D-based phases. Interestingly, the hydrogen content on each of these surfaces decreases with increasing potential such that the hydrogen concentration on the surface does not uniformly decrease when the applied potential is increased. For instance, a transition from (2 × 2)-6H to (2 × 2)-2D-8H is predicted for increasing potential (at ∼−0.3 V), thus meaning an increase in hydrogen content, while with further increasing potential, hydrogen then desorbs again from the (2 × 2)-2D-type structure. At an applied potential of about 0.1 V, the (2 × 2)-2D-H-Cl phase with hydrogen and chlorine co-adsorption is stabilized, however, only in a tiny potential window. Hence, this means a rather sharp transition from hydrogen to chlorine adsorption.

For more anodic potentials, chlorine adsorption is dominant, quickly reaching the already rather distorted (2 × 2)-2D-8Cl surface. From the large phase space occupied by the In- and Cl-rich phases observed in Figure 5, it seems surprising that these structures are not present under electrochemical conditions. However, by connecting the applied voltage to the selected plots at fixed In chemical potentials, which are depicted in Figures 5a−c, this becomes more evident. The white pentagons in Figure 5a−c mark the phases that correspond to a particular applied voltage under the given electrochemical conditions for the depicted values of $\Delta\mu_{In}$. This means, for instance, that a potential of −0.25 V corresponds to a $\Delta\mu_{In}$ of −0.9 eV, with $\Delta\mu_{Cl}$ = −1.44 eV and $\Delta\mu_{H}$ = −0.01 eV (see Figure 5a), describing a point in the phase diagram where the (2 × 2)-2D-6H phase is found to be stable. By further examining the situations depicted in Figures 5a−c, it becomes clear that for increasing voltage, the electrochemical potential of In (and hydrogen) decreases, such that In-poorer (and H-poorer) surfaces become more favorable. Thus, when the potentials at which Cl adsorption becomes favorable are reached, there is at the same time a preference for P-terminated surfaces, such that In- and Cl-rich phases cannot be reached. As already mentioned in the general discussion on the CHE, this approach may introduce an uncertainty in the potential domain when comparing these results to experiment, meaning that the onset potential of transitions between different surface reconstructions may be shifted. Finally, it has to be noted that recent studies on hydrogen-terminated (2 × 2)-based phases demonstrated that doping can result in the stabilization of charged surfaces, depending on the Fermi level position.[36] This indicates that applied potentials may also favor charged surfaces and/or affect the electronic structure.

While the above results give valuable insights with respect to the different phases that are, or could in principle be, observed under experimental conditions, an open question is the impact of the adsorbates on the electronic properties. Surface reconstructions that create electronic states within the band gap of InP are detrimental for the use as a photoelectrode and should therefore be avoided. To investigate how the electronic structure is affected by the respective adsorbates, we determined the band structure for the different structures that are predicted to be stable under electrochemical conditions. Before discussing the results, it has to be noted that the applied PBE+D3 approach largely underestimates the band gap, a well-known issue for generalized gradient-based functionals, hence yielding a bulk band gap of ∼0.48 eV for InP. Furthermore, it has to be pointed out that due to the finite system size, band gaps larger than the bulk value can be observed.[37] This finite size effect is, however, decreasing with an increasing slab size. Yet, for some of the surface reconstructions shown here (indicated by arrows in Figure 7), even a slab thickness of beyond 40 layers does not lead to full convergence. This is probably the reason why, for surface slabs of InP, band gaps closer to the experimental value (1.3 eV) than to the PBE-underestimated bulk band gap are frequently reported. The resulting band gaps are depicted in Figure 8 and compared to the bulk value, showing that for some phases the width of the band gap is largely affected. Band structure plots of the corresponding phases, showing midgap states or changes at the band edges, causing the observed changes in the band gap are depicted in Figure S2 in the SI. In

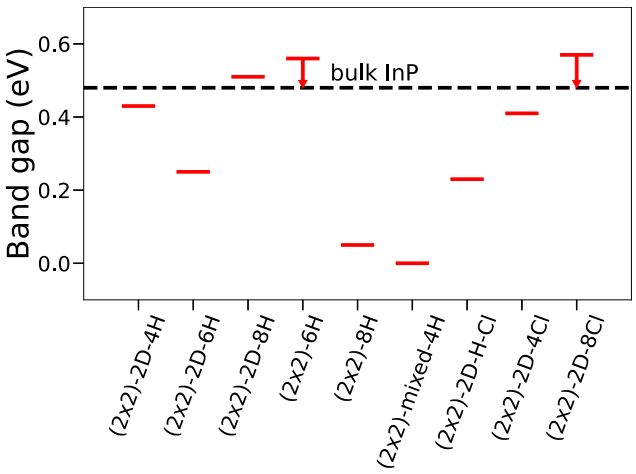

Figure 8. Calculated band gaps for the different surface reconstructions that are observed in Figure 7. The bulk band gap is depicted as a dashed line. The corresponding band structure plots are shown in Figure S2.

https://doi.org/10.1021/acsami.4c20370
ACS Appl. Mater. Interfaces 2025, 17, 8601−8609

fact, qualitatively the (2 × 2)-2D-based phases show band gaps close to the bulk value for (2 × 2)-2D-4H and the H-rich (2 × 2)-2D-8H phase, whereas (2 × 2)-2D-6H is affected by the presence of midgap states. A similar behavior is observed for the (2 × 2)-based phases where (2 × 2)-6H is observed to have a bulk-like gap, while the (2 × 2)-2D-8H becomes almost metallic. The (2 × 2)-2D-H-Cl phase also shows a decreased band gap, whereas for the Cl-rich phases, the band gap is again close to the bulk value, and no midgap states are observed. Hence, especially for the (2 × 2)-2D-8H, (2 × 2)-6H, and the Cl-rich (2 × 2)-2D-8Cl phases, no detrimental effects, such as charge-trapping in gap states, are expected. Consequently, these structures could be good starting points for (photo)-electrochemical surface processing.

CONCLUSION

By using DFT we were able to investigate the gas-phase adsorption of hydrogen and chlorine on InP(100), showing that coadsorption can only be observed for very small ranges of the chemical potential phase space. The novel type of phase diagram, which we introduce here, allows a quantification of phase stabilities with respect to competing phases, thus emphasizing that certain phases may be difficult to observe experimentally. The resulting phase diagrams clearly point to a dominant occurrence of phases featuring In−Cl bonds such as the $InCl_3$-type surface. Surprisingly, these findings do not hold in an electrochemical environment. There, the differences in respective standard potentials and oxidation states of In, Cl, and H restrict the accessible part of the phase space such that In- and, at the same time, Cl-rich phases are not observed. The hydrogen coverage, on the other hand, does not simply decrease with more anodic potential but instead fluctuates with changing potential. This is because the more P-rich-based surface reconstructions are stabilized with increasing potential. Furthermore, a sharp transition from hydrogen to chlorine adsorption is observed, such that the hypothesis derived from experiment of H−Cl coadsorption seems rather unlikely. Finally, an investigation of the electronic band structure shows that the adsorption does not generally introduce midgap surface states in InP, which is a prerequisite for materials to be used as high-performance photoelectrode or processing of optoelectronic devices in electrochemical environments.

ASSOCIATED CONTENT

Data Availability Statement

The data underlying this study will be made openly available upon reasonable request to the authors.

Supporting Information

The Supporting Information is available free of charge at https://pubs.acs.org/doi/10.1021/acsami.4c20370.

Additional computational details and band structure plots (PDF)

AUTHOR INFORMATION

Corresponding Author

Holger Euchner − *Universität Tübingen, Institute of Physical and Theoretical Chemistry, 72076 Tübingen, Germany;* orcid.org/0000-0003-2287-6970; Email: holger.euchner@uni-tuebingen.de

Authors

Vibhav Yadav − *Universität Tübingen, Institute of Physical and Theoretical Chemistry, 72076 Tübingen, Germany*

Matthias M. May − *Universität Tübingen, Institute of Physical and Theoretical Chemistry, 72076 Tübingen, Germany;* orcid.org/0000-0002-1252-806X

Complete contact information is available at: https://pubs.acs.org/10.1021/acsami.4c20370

Notes

The authors declare no competing financial interest.

ACKNOWLEDGMENTS

The authors gratefully acknowledge funding from the German Bundesministerium für Bildung and Forschung (BMBF), project "NETPEC" (No. 01LS2103A), and from the German Research Foundation (DFG), project number 434023472. The authors acknowledge support by the state of Baden-Württemberg through bwHPC and the German Research Foundation (DFG) through grant no. INST 40/575-1 FUGG (JUSTUS 2 cluster) and by the HoreKa supercomputer funded by the Ministry of Science, Research and the Arts Baden-Württemberg and by the Federal Ministry of Education and Research.

REFERENCES

(1) Jacobsson, T. J.; Fjällström, V.; Edoff, M.; Edvinsson, T. Sustainable solar hydrogen production: from photoelectrochemical cells to PV-electrolyzers and back again. *Energy Environ. Sci.* **2014**, *7*, 2056−2070.

(2) Turner, J. A. Sustainable Hydrogen Production. *Science* **2004**, *305*, 972−974.

(3) Khaselev, O.; Turner, J. A. A Monolithic Photovoltaic-Photoelectrochemical Device for Hydrogen Production via Water Splitting. *Science* **1998**, *280*, 425−427.

(4) May, M. M.; Lewerenz, H.-J.; Lackner, D.; Dimroth, F.; Hannappel, T. Efficient direct solar-to-hydrogen conversion by in situ interface transformation of a tandem structure. *Nat. Commun.* **2015**, *6*, 8286.

(5) Schleuning, M.; Ahmet, I. Y.; van de Krol, R.; May, M. M. The role of selective contacts and built-in field for charge separation and transport in photoelectrochemical devices. *Sustain. Energy Fuels* **2022**, *6*, 3701−3716.

(6) Kölbach, M.; Rehfeld, K.; May, M. M. Efficiency gains for thermally coupled solar hydrogen production in extreme cold. *Energy Environ. Sci.* **2021**, *14*, 4410−4417.

(7) Schmitt, E. A.; Guidat, M.; Nusshör, M.; Renz, A.-L.; Möller, K.; Flieg, M.; Lörch, D.; Kölbach, M.; May, M. M. Photoelectrochemical Schlenk cell functionalization of multi-junction water-splitting photoelectrodes. *Cell Reports Phys. Sci.* **2023**, *4*, 101606.

(8) Wood, B. C.; Ogitsu, T.; Schwegler, E. Local structural models of complex oxygen- and hydroxyl-rich GaP/InP(001) surfaces. *J. Chem. Phys.* **2012**, *136*, 064705.

(9) Wood, B. C.; Schwegler, E.; Choi, W. I.; Ogitsu, T. Hydrogen-Bond Dynamics of Water at the Interface with InP/GaP(001) and the Implications for Photoelectrochemistry. *J. Am. Chem. Soc.* **2013**, *135*, 15774−15783.

(10) Wood, B. C.; Schwegler, E.; Choi, W. I.; Ogitsu, T. Surface Chemistry of GaP(001) and InP(001) in Contact with Water. *J. Phys. Chem. C* **2014**, *118*, 1062−1070.

(11) Pham, T. A.; Zhang, X.; Wood, B. C.; Prendergast, D.; Ptasinska, S.; Ogitsu, T. Integrating Ab Initio Simulations and X-ray Photoelectron Spectroscopy: Toward A Realistic Description of Oxidized Solid/Liquid Interfaces. *J. Phys. Chem. Lett.* **2018**, *9*, 194−203.

(12) Zhang, X.; Ogitsu, T.; Wood, B. C.; Pham, T. A.; Ptasinska, S. Oxidation-Induced Polymerization of InP Surface and Implications for Optoelectronic Applications. *J. Phys. Chem. C* **2019**, *123*, 30893−30902.
(13) Ruiz Alvarado, I. A.; Karmo, M.; Runge, E.; Schmidt, W. G. InP and AlInP(001)(2 × 4) Surface Oxidation from Density Functional Theory. *ACS Omega* **2021**, *6*, 6297−6304.
(14) Ruiz Alvarado, I. A.; Schmidt, W. G. Water/InP(001) from Density Functional Theory. *ACS Omega* **2022**, *7*, 19355−19364.
(15) Löw, M.; Guidat, M.; Kim, J.; May, M. M. The interfacial structure of InP(100) in contact with HCl and H_2SO_4 studied by reflection anisotropy spectroscopy. *RSC Adv.* **2022**, *12*, 32756−32764.
(16) Nørskov, J. K.; Rossmeisl, J.; Logadottir, A.; Lindqvist, L.; Kitchin, J. R.; Bligaard, T.; Jónsson, H. Origin of the Overpotential for Oxygen Reduction at a Fuel-Cell Cathode. *J. Phys. Chem. B* **2004**, *108*, 17886−17892.
(17) Guidat, M.; Löw, M.; Kölbach, M.; Kim, J.; May, M. M. Experimental and Computational Aspects of Electrochemical Reflection Anisotropy Spectroscopy: A Review. *ChemElectroChem.* **2023**, *10*, No. e202300027.
(18) Schmidt, W. G.; Hahn, P. H.; Bechstedt, F.; Esser, N.; Vogt, P.; Wange, A.; Richter, W. InP(001)-(2 × 1) Surface: A Hydrogen Stabilized Structure. *Phys. Rev. Lett.* **2003**, *90*, 126101.
(19) Kühne, T. D.; et al. CP2K: An electronic structure and molecular dynamics software package - Quickstep: Efficient and accurate electronic structure calculations. *J. Chem. Phys.* **2020**, *152*, 194103.
(20) Krack, M. Pseudopotentials for H to Kr optimized for gradient-corrected exchange-correlation functionals. *Theor. Chem. Acc.* **2005**, *114*, 145−152.
(21) Perdew, J. P.; Burke, K.; Ernzerhof, M. Generalized Gradient Approximation Made Simple. *Phys. Rev. Lett.* **1996**, *77*, 3865−3868.
(22) Grimme, S.; Antony, J.; Ehrlich, S.; Krieg, H. A consistent and accurate ab initio parametrization of density functional dispersion correction (DFT-D) for the 94 elements H-Pu. *J. Chem. Phys.* **2010**, *132*, 154104.
(23) Reuter, K.; Scheffler, M. Composition, structure, and stability of RuO_2 (110) as a function of oxygen pressure. *Phys. Rev. B* **2001**, *65*, 035406.
(24) Groß, A. Grand-canonical approaches to understand structures and processes at electrochemical interfaces from an atomistic perspective. *Curr. Opin. Electrochem.* **2021**, *27*, 100684.
(25) Peterson, A. A.; Abild-Pedersen, F.; Studt, F.; Rossmeisl, J.; Nørskov, J. K. How copper catalyzes the electroreduction of carbon dioxide into hydrocarbon fuels. *Energy Environ. Sci.* **2010**, *3*, 1311.
(26) Gossenberger, F.; Roman, T.; Groß, A. Hydrogen and halide co-adsorption on Pt(111) in an electrochemical environment: a computational perspective. *Electrochim. Acta* **2016**, *216*, 152−159.
(27) Euchner, H.; Groß, A. Atomistic modeling of Li- and post-Li-ion batteries. *Phys. Rev. Mater.* **2022**, *6*, 040302.
(28) Bratsch, S. G. Standard Electrode Potentials and Temperature Coefficients in Water at 298.15 K. *J. Phys. Chem. Ref. Data* **1989**, *18*, 1−21.
(29) Wittstock, G. *Gunther Wittstock Lehrbuch der Elektrochemie*; Wiley, 2023.
(30) Groß, A. Reversible vs Standard Hydrogen Electrode Scale in Interfacial Electrochemistry from a Theoretician's Atomistic Point of View. *J. Phys. Chem. C* **2022**, *126*, 11439−11446.
(31) Zhang, C.; Sprik, M. Finite Field Methods for the Supercell Modelling of Charged Insulator-Electrolyte Interfaces. *Phys. Rev. B* **2016**, *94*, 245309.
(32) Zhang, C.; Hutter, J.; Sprik, M. Coupling of Surface Chemistry and Electric Double Layer at TiO2 Electrochemical Interfaces. *J. Phys. Chem. Lett.* **2019**, *10*, 3871−3876.
(33) Schmidt, W. G. III-V compound semiconductor (001) surfaces. *Appl. Phys. A: Mater. Sci. Process.* **2002**, *75*, 89−99.
(34) Pashley, M. D. Electron counting model and its application to island structures on molecular-beam epitaxy grown GaAs(001) and ZnSe(001). *Phys. Rev. B* **1989**, *40*, 10481−10487.
(35) Roscher, J.; Holze, R. Reference Electrodes. *Encyclopedia* **2023**, *3*, 478−489.
(36) Sciotto, R.; Ruiz Alvarado, I. A.; Schmidt, W. G. Substrate Doping and Defect Influence on P-Rich InP(001):H Surface Properties. *Surfaces* **2024**, *7*, 79−87.
(37) Cupo, A.; Meunier, V. Quantum confinement in black phosphorus-based nanostructures. *J. Phys.: Condens. Matter* **2017**, *29*, 283001.

https://doi.org/10.1021/acsami.4c20370
ACS Appl. Mater. Interfaces 2025, 17, 8601−8609

Supporting Information

The InP(100) Surface Phase Diagram: From the Gas-Phase to the Electrochemical Environment

Holger Euchner,* Vibhav Yadav, and Matthias M. May

Universität Tübingen, Institute of Physical and Theoretical Chemistry, Auf der Morgenstelle 15, 72076 Tübingen, Germany

E-mail: holger.euchner@uni-tuebingen.de

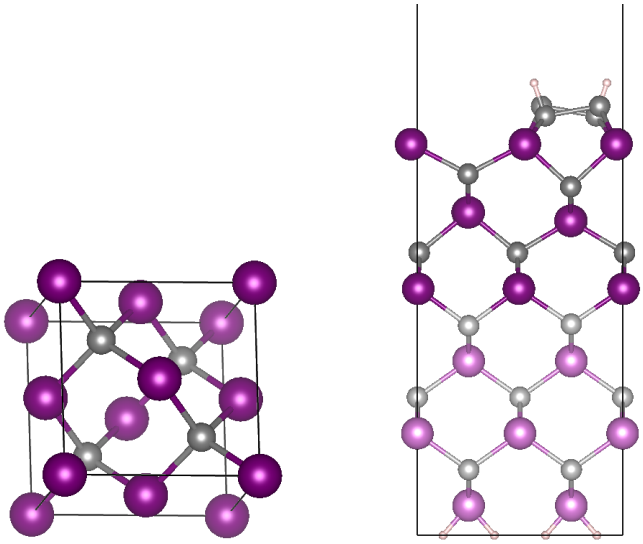

Figure S1: Bulk InP structure with In and P atoms in purple and grey (left). Schematic depiction of the computational setup for the InP(100) surface. The light grey (P) and light purple (In) atoms are kept fix during the calculations, while the positions of the In and P atoms in the top most layers (dark purple and dark grey) are optimized (right).

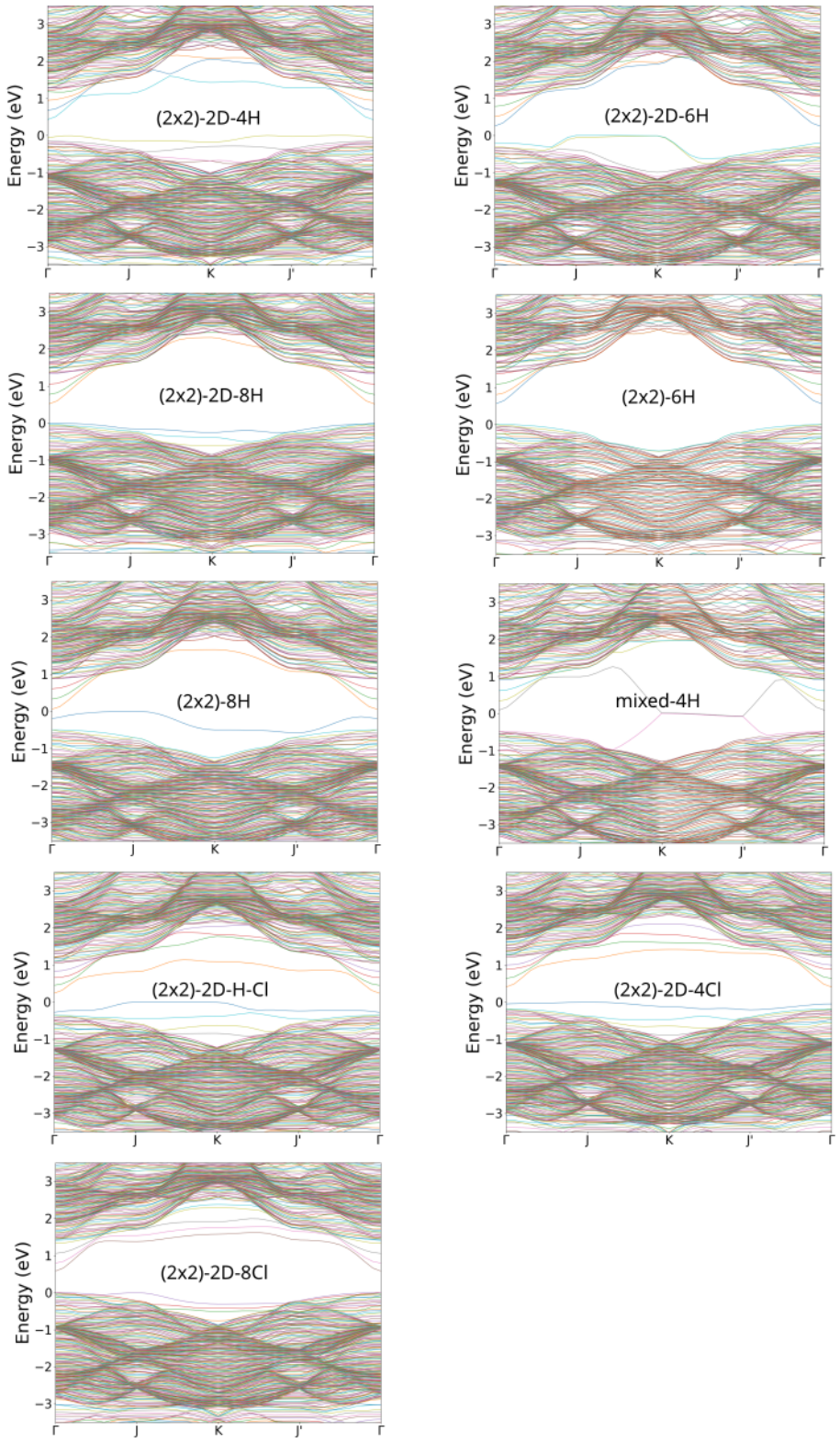

Figure S2: Band structure of the different stable phases that are observed under the given electrochemical conditions (see main text). The resulting band gaps for the different structures are given in Fig. 8 in the main manuscript.

Declaration of originality

Name: MSc. Vibhav Yadav

Hereby, I confirm that the submitted doctoral thesis:

1. is written by me,
2. the source of information of the text is solely based on the aforementioned references, the published papers, and discussions,
3. I confirm that the electronic and printed version of this cumulative dissertation are identical in content and format.

Place, Date Tübingen 12.06.2026 Signature [redacted]